HU ISSN 1586–2070

JOURNAL OF COMPUTATIONAL AND APPLIED MECHANICS

A Publication of the University of Miskolc

VOLUME 7, NUMBER 1 (2006)

MISKOLC UNIVERSITY PRESS

HU ISSN 1586–2070

JOURNAL OF COMPUTATIONAL AND APPLIED MECHANICS

A Publication of the University of Miskolc

VOLUME 7, NUMBER 1 (2006)

MISKOLC UNIVERSITY PRESS

EDITORIAL BOARD

István PÁCZELT, Editor in Chief, Department of Mechanics, University of Miskolc, 3515 MISKOLC, Hungary, mechpacz@uni-miskolc.hu

László BARANYI, Department of Fluid and Heat Engineering, University of Miskolc, 3515 MISKOLC, Hungary, arambl@uni-miskolc.hu

Edgár BERTÓTI, Department of Mechanics, University of Miskolc, 3515 MISKOLC, Hungary, mechber@uni-miskolc.hu

Tibor CZIBERE, Department of Fluid and Heat Engineering, University of Miskolc, 3515 MISKOLC, Hungary, aramct@uni-miskolc.hu

István ECSEDI, Department of Mechanics, University of Miskolc, 3515 MISKOLC, Hungary, mechecs@uni-miskolc.hu

Wolfram FRANK, Institut für Fluid- und Thermodynamik, Universität Siegen, Paul-Bonatz-Strasse 9-11, 57076 SIEGEN, Germany, frank@ift.mb.uni-siegen.de

Ulrich GABBERT, Institut für Mechanik, Otto-von-Guericke-Universität Magdeburg, Universitätsplatz 2, 39106 MAGDEBURG, Germany, ulrich.gabbert@mb.uni-magdeburg.de

Zsolt GÁSPÁR, Department of Structural Mechanics, Budapest University of Technology and Economics, Műegyetem rkp. 3, 1111 BUDAPEST, Hungary, gaspar@ep-mech.me.bme.hu

Robert HABER, Department of Theoretical and Applied Mechanics, University of Illinois at Urbana-Champaign, 216 Talbot Lab., 104 S. Wright Str., URBANA, IL 61801, USA, r-haber@uiuc.edu

Gábor HALÁSZ, Department of Hydraulic Machines, Budapest University of Technology and Economics, Műegyetem rkp. 3, 1111 BUDAPEST, Hungary, HALASZ@vizgep.bme.hu

Ji Huan HE, Department of Mathematics, College of Basic Science, Shanghai Donghua University, No. 1882 Yan'anxilu Road, 200051 SHANGHAI, China, jhhe@dhu.edu.cn

Károly JÁRMAI, Department of Materials Handling and Logistics, University of Miskolc, 3515 MISKOLC, Hungary, altjar@uni-miskolc.hu

László KOLLÁR, Department of Strength of Materials and Structures, Budapest University of Technology and Economics, Műegyetem rkp. 3. K.II.42., 1521 BUDAPEST, Hungary, lkollar@eik.bme.hu

Vladimir KOMPIŠ, Department of Mechanics, Faculty of Mechanical Engineering, University of Žilina, ŽILINA, Slovakia, kompisv@fstroj.utc.sk

Imre KOZÁK, Department of Mechanics, University of Miskolc, 3515 MISKOLC, Hungary, mechkoz@uni-miskolc.hu

József KÖVECSES, Mechanical Engineering Department 817 Sherbrooke Street West, MD163 Montreal, Quebec H3A 2K6 jozsef.kovecses@mcgill.ca

Márta KURUTZ, Department of Structural Mechanics, Budapest University of Technology and Economics, Műegyetem rkp. 3, 1111 BUDAPEST, Hungary, kurutzm@eik.bme.hu

R. Ivan LEWIS, Room 2-16 Bruce Building, Newcastle University, NEWCASTLE UPON TYNE, NE1 7RU, UK, R.I.Lewis@NCL.AC.UK

Gennadij LVOV, Department of Mechanics, Kharkov Polytechnical Institute, 2 Frunze Str., 310002 KHARKOV, Ukraine, lvovgi@kpi.kharkov.ua

Herbert MANG, Institute for Strength of Materials, University of Technology, Karlsplatz 13, 1040 VIENNA, Austria, Herbert.Mang@tuwien.ac.at

Zenon MROZ, Polish Academy of Sciences, Institute of Fundamental Technological Research, Swietokrzyska 21, WARSAW, Poland zmroz@ippt.gov.pl

Gyula PATKÓ, Department of Machine Tools, University of Miskolc, 3515 MISKOLC, Hungary, mechpgy@uni-miskolc.hu

Jan SLADEK, Ústav stavbeníctva a architektúry, Slovenskej akadémie vied, Dubróvska cesta 9, 842 20 BRATISLAVA, Slovakia, usarslad@savba.sk

Gábor STÉPÁN, Department of Mechanics, Budapest University of Technology and Economics, Műegyetem rkp. 3, 1111 BUDAPEST, Hungary, stepan@mm.bme.hu

Barna SZABÓ, Center for Computational Mechanics, Washington University, Campus Box 1129, St. LOUIS, MO63130, USA, szabo@me.wustl.edu

Szilárd SZABÓ, Department of Fluid and Heat Engineering, University of Miskolc, 3515 MISKOLC, Hungary, aram2xsz@uni-miskolc.hu

György SZEIDL, Department of Mechanics, University of Miskolc, 3515 MISKOLC, Hungary, Gyorgy.SZEIDL@uni-miskolc.hu

LOCAL EDITORIAL COUNCIL

T. CZIBERE, I. KOZÁK, I. PÁCZELT, G. PATKÓ, G. SZEIDL

Journal of Computational and Applied Mechanics, Vol. 7., No. 1., (2006), pp. 3–12

COMPARISON OF STRAIN GAUGE TECHNIQUE AND PHOTOELASTIC COATING METHOD IN THE INVESTIGATION PROCEDURE OF FEMUR PROSTHESES

Lajos Borbás
Department of Vehicle Parts and Drives
Budapest University of Technology and Economics
Műegyetem rkp. 3-5., H-1521 Budapest, Hungary
`borbas@kge.bme.hu`

Frigyes Thamm
Department of Applied Mechanics
Budapest University of Technology and Economics
Műegytem rkp. 3-5., H-1521 Budapest, Hungary

László Oláh
Department of Polymer Engineering
Budapest University of Technology and Economics
Műegytem rkp. 3-5., H-1521 Budapest, Hungary
`olah@pt.bme.hu`

[Received: August 31, 2004]

Abstract. Photoelastic coating was applied to investigate the contact stress distribution between the femur shaft and the indrawn prosthesis. To obtain an overall pattern of the stress distribution the investigated femur was placed on a turntable with its axis parallel to the femur shaft. Fringe patterns obtained at different angular positions of the turntable were combined producing a flattened overall image of the whole surface of the femur shaft. The patterns proved to be much more instructive than measurements applying strain gauges

Keywords: strain gauge technique, photoelastic coating method

1. **Introduction**

There are a great number of *femur head prostheses* of different shapes used in *traumatological* surgery. The comparison of their efficiency is highly difficult due to the irregularities of the individual femur shape and the procedure of "driving" them into the femur channel. Different positions during the movement of the person (walking, running, stepping on stairs, etc.) cause more or less different stress distributions in the femur and especially along the contact surface between the femur channel and the stem of the prosthesis.

Thus it became difficult to obtain the suitable shape of the prosthesis became difficult and this resulted in different designs dependent on the opinion of the surgeon about the relative danger caused by one or another load position on the femur.

The main differences between the particular parts of the prosthesis included the shape of the central line of the stem (straight or curved) and its cross-section along its length (nearly circular or more or less lengthy). Additional problems arose from the scatter of the elastic and strength properties of the cortical and *trabecular* bones [1,2].

A number of theoretical investigations were carried out [3]-[8] which yielded some insight into the mechanism of force transfer between the prosthesis and the femur shaft, but due to the necessary simplifications made during the calculations they could yield only guidelines for the recommended shape of the prosthesis.

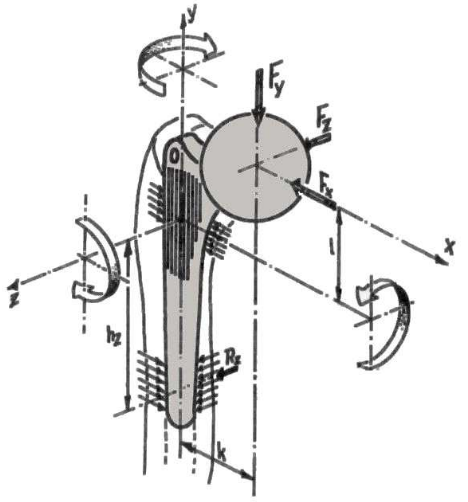

Figure 1. The external forces and moments acting on a femur prosthesis

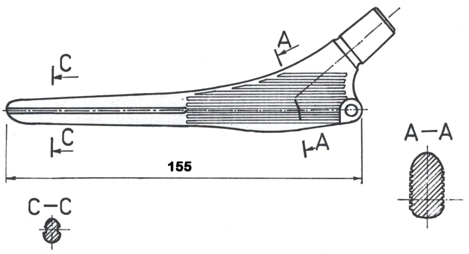

Figure 2. Prosthesis type *MY*. The vertical grooves on the upper half of the stem were intended to withstand the torsion moment M_y as shown in Figure 1

In Figure 1 all possible components of the external forces and moments acting upon the prosthesis are collected. According to the conditions of equilibrium the following equations can be written: $M_x = F_z l$, $M_y = F_z k$, $M_z = F_z k$.

Most of them create normal contact stresses between the prosthesis stem and the femur shaft provided good ingrown bond between both. Force F_y and moment M_y have to be transmitted to the bone by interface shear. Particularly the latter may cause failure especially for prostheses whose stems have approximately circular cross-section. Thorough optical mapping of a femur shaft actually revealed a cross-section of such shape as well [13], the result will be discussed in Section 3. Axial ribbing of the prosthesis [9] or surface treatment of the prosthesis stem [10] may improve the contact but may also create failure of the stem.

Implant longevity depends on the stability of the prosthesis in the bone. Relative movement of the prosthesis against the bone must be of a very low value [11] and the contact stress between them should also be as smooth as possible. To obtain the necessary experience of prosthesis design, experiments on cadavers have to be carried out. The problem is, however, that measurements can be carried out mostly only at the outer surface of the femur, letting possible contact stress concentrations remain hidden. Interpretation must depend therefore on the thorough evaluation of the stress patterns obtained in experiments.

2. **Preliminary experiments**

The cooperation between the Department of Traumatologic Surgery of Szent János Hospital in Budapest under the leadership of G. Krakovits, the PROTETIM Kft. (Medical Devices; director I. Juhász), the KALIBER Műszer és Méréstechnika Kft. (Enterprise for Mechanical Measurement; technical director I. Ballon), the Department of Applied Mechanics, and the Department of Vehicle Parts and Drives of the BUTE resulted in some preliminary work in the field of biomechanics applying different kinds of strain measurement technologies [14].

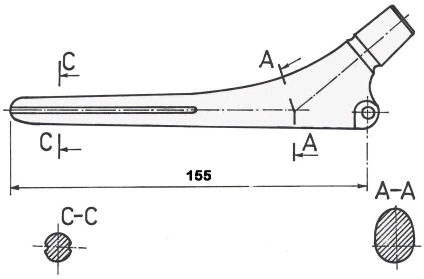

Figure 3. Prosthesis type KR

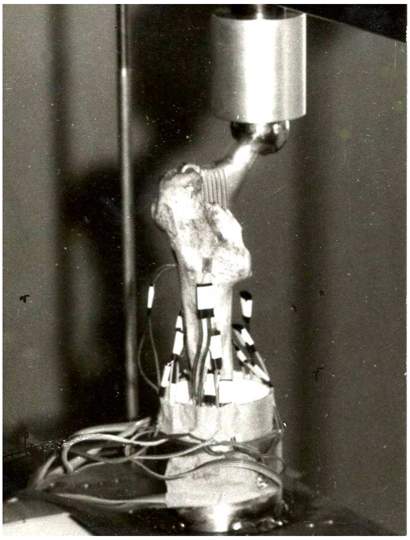

Figure 4. A femur with the indrawn prosthesis with bonded strain gauges

To obtain some insight into the influence of the shape of the prosthesis stem on the contact stress distribution, two series of strain gauge measurements were carried out using different prostheses made by the PROTETIM Kft. and widely used in Hungary.

In the first series an intact bone (No.1) was compared with three femurs with prostheses as follows: No.2: un-cemented prosthesis with a narrow cross-section (Type “MY”), No.3: un-cemented prosthesis with nearly circular cross-section of the stem

(Type “KR”), No.4: Cemented prosthesis (Type “KR”). The notations follow those used by PROTETIM. The shapes of the prostheses are shown in Figures 2 and 3.

A vertical load of $F_y = 425N$ was applied. One of the specimens with the strain gages bonded on it and placed into the loading rig is shown in Figure 4. The measured strains plotted over the femur length are collected in Figure 5. As the gauges No. 56, 70 and 58 were in vertical position, they indicated strain in this direction. Only gauge No. 55 indicated the presence of hoop or shear stress but no clear conclusions could be drawn about the question of which of the prostheses would be favorable.

In a second attempt *uniaxial* loading by the force $F_y$was compared with a combined load consisting of F_y and a torsional moment $M_t = aF_{xt}$ as seen in Figure 6. From the strains measured approximate stress values were calculated by multiplying them simply with estimated Young's moduli based on data from [1]. As seen from the plot of the stresses, the applied positions of the strain gauges proved to be insensitive to possible shear stresses caused by the torque. Application of strain rosettes on more points of the bone surface would have been more effective, but the evaluation of multiaxial stress states would have been difficult because of the anisotropic elasticity of the bone material.

3. Application of photoelasic coating

As shown above, pointwise measurement is not sufficient to obtain a sound impression about possible stress peaks whose location is not known. Therefore the photoelastic coating technique was applied. The coating was about 2 mm thick and consisted of a flexibilized epoxy resin in order to minimize its stiffening effect upon the femur as

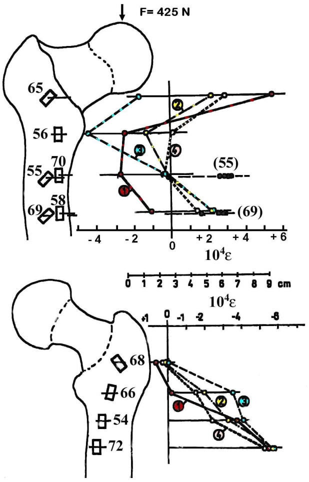

Figure 5. Strain distribution on four different species evaluated from the strain gage data: 1. Intact bone, 2. Prosthesis with a narrow stem, 3. Prosthesis with a thick stem, 4. Cemented prosthesis

investigated by Cristofolini [12]. The strain-optical constant S_ε of the coating was determined in the usual way on a strip of it bonded on a cantilever beam loaded to known deflection.

The actual value of the strain-optical constant was: S_ε= 1,04.10^{-3} strain/fringe order.

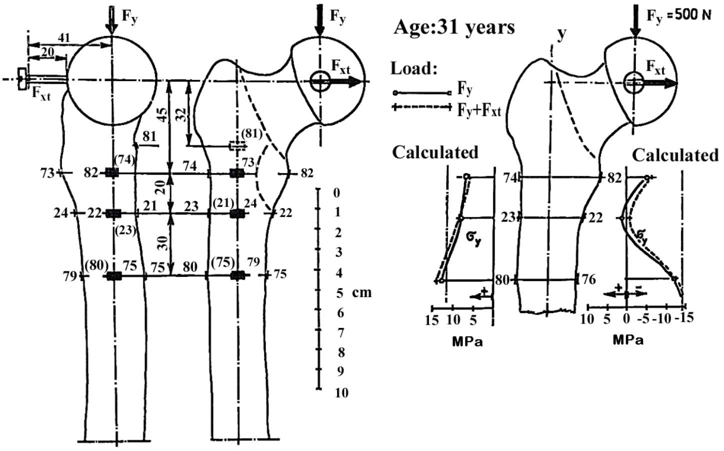

Figure 6. Position of the strain gauges and evaluated stress distribution from an experiment with two different loading modes (bending, bending + torsion)

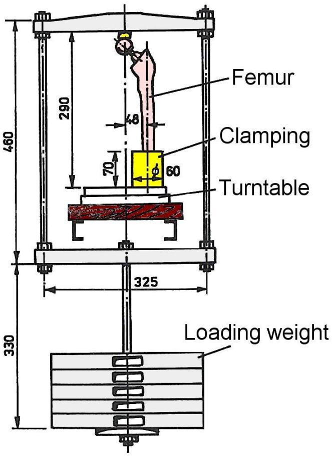

Figure 7. Femur investigated in the loading rig

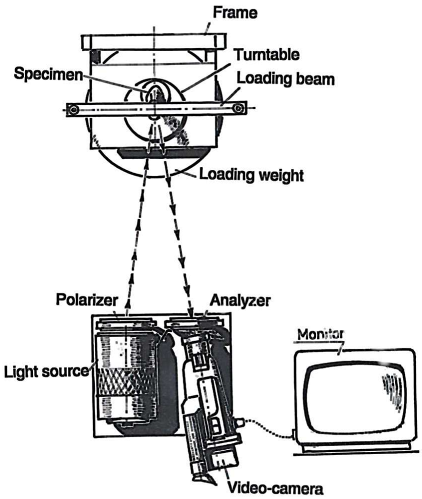

Figure 8. Measurement set-up for the *photoeleastic* investigation

To obtain a pattern of the complete surface of the femur, the investigated specimen together with the loading rig was mounted on a turntable. The full *isochromatic* fringe pattern was then combined from pictures taken by turning the loading rig in steps of 30^0.

The side view of the assembly is shown in Figure 7, and the complete instrumentation including the reflection polariscope provided with a video-camera and the attached monitor in Figure 8.

Patterns of six specimens were obtained, the data of which are given in Table 1.

Table 1: Data of the specimens undergoing photoelastic investigation.

Number	Type of prosthesis*	Stem shape	Fixation method	Load F [N]	Load-free test	Compressive Young modulus E[MPa]
1	KR	Straight	Driving-in	735.5	Yes	$2.799.10^4$
2	KR	Straight	Driving-in		Yes	$1.306.10^4$
3	Mm	Curved	Bonding		No	$1.306.10^4$
4	Mm	Curved	Driving-in		Yes	$1.399.10^4$
5	MY	Straight	Bonding		No	$1.311.10^4$
6	- **	Intact Femur		612.9	No	$1.248.10^4$

To obtain patterns adjusted well to each other, we had to depart from the standard ISO 7206 and positioned the axis of the femur shaft parallel to the rotational axis of the loading frame. To identify the position of the fringes, a network of generators and contours of the cross-sections were drawn on the specimens.

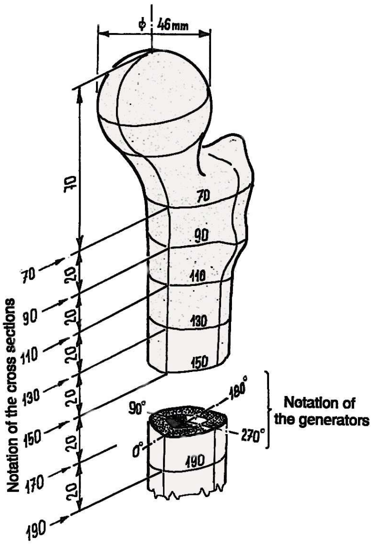

Figure 9. System of coordinate lines drawn upon the surface of the femur for the identification of the measurement results. 0^o: anterior, 180^o: posterior

Their notations are collected in Figure 9. As the *photoelastic* coating was bonded on the surface of the femurs with already mounted prostheses the fringe pattern observed did not show the stress distribution caused by the driving-in process.

To obtain data about the latter, the prosthesis was – where it was possible - extracted from the femur and underwent a second *photoelastic* investigation without the external load (see Table 1).

The *isochromatic* fringe patterns were determined at crossed and parallel *polarizers* showing the integer and half orders, respectively. In one case *polarizers* inclined at 45^o to each other were also applied producing fringes of 1/4 and 1/3 order. Figure 10 shows one characteristic flattened fringe pattern with the fringe orders noted along the fringes.

From the fringe patterns the difference of the principal strains can be obtained by the equation

$$\varepsilon_1 - \varepsilon_2 = S_\varepsilon m \tag{1}$$

with ε_1 and ε_2 the two principal strains, S_ε the strain fringe constant and m the fringe order.

It should be noted that the principal strain and principal stress difference is always positive. Regions of tension and compression can only be distinguished in a case of pure uniaxial loading and compression which is assumed in the intact part of the femur shaft in case of loading as shown in Figure 7.

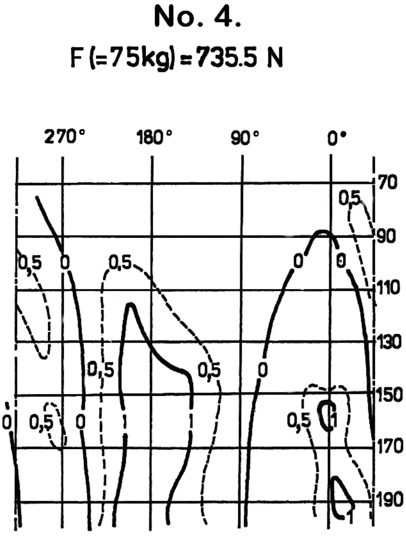

Figure 7. Example of a flattened fringe pattern (specimen No.4 of Table 1). The notation of the cross sections and the generators corresponds to that shown in Figure 9.

The sign of stress can be obtained from the equilibrium conditions. Tension and compression are divided on the fringe patterns by a distinct line of zero fringe order.

To obtain stress values, the Young modulus and the Poisson ratio of the cortical bone is to be known. To avoid the necessity of using foreign data, the fringe pattern of the lower part of the femur below the prosthesis stem was used as calibration specimen.

In an earlier work [13] the cross-sectional data of femur shafts were calculated based on measurements of slices cut out of the shaft of the investigated femurs. A nearly circular shape with the principal axis of inertia lying approximately in the x and z directions as seen in Figure 1 was observed with the principal moduli of inertia being about $J_1 \approx J_z \approx 4.2 \times 10^4$ mm^4, resp. $J_2 \approx J_x \approx 3.10 \times 10^4$ mm^4 and the cross section area of about $A \approx 300$ mm^2. In a proper distance from the prosthesis stem tip only uniaxial stress state in the y-direction can be assumed resulting from the force F and the bending moment Fk (Figure 11). The stress σ at a distance ξ from the center of gravity of the cross-section can be calculated according to elementary mechanics:

$$\sigma = -F\left[\frac{k\xi}{J_z} + \frac{1}{A}\right] \tag{2a}$$

the negative sign meaning compression. Its highest value appears at point P of Figure 9. Considering the cross-section of the femur shaft to be cylindrical the negative stress peak will be

$$\sigma_0 = -F\left[\frac{kD}{2J_z} + \frac{1}{A}\right] . \tag{2b}$$

According to Hooke's law the relation between the difference of the principal strains and stresses is, taking into account equation (1),

$$\sigma_1 - \sigma_2 = \frac{E}{1+\upsilon}\left(\varepsilon_1 - \varepsilon_2\right) = \frac{E}{1+\upsilon}S_\varepsilon m = S_\sigma m \tag{3}$$

with S_σ the stress-fringe constant. Because of the uniaxial stress state σ_1 has to be zero, combining the fringe order $m = m_P$ at point P with equation (2a)

$$S_\sigma = \sigma_0/m_P \tag{4}$$

is obtained, which allows the transition from fringe values to stresses. Assuming a Poisson ratio of $\nu = 0.4$, formulas (3) and (4) also allow an estimation of the Young modulus. Its values for the femurs investigated are therefore also collected in Table 1. Fair agreement with data found in [1] can be stated.

4. **Discussion of the results**

According to equation (1), the external values of axial stress in the femur shaft have to appear at generators 0^0 (negative) and 180^0 (positive) of Figure 9 remaining approximately constant along the shaft length as long as its cross-section does not change nearing the femur head. This can be seen clearly in Figure 12 obtained from an intact femur (listed No.6 in Table 1) The figure also shows the stress distribution along the surface of the femur shaft at the cross-sections 130 mm and 190 mm.

Figure 13 (No.5 in Table 1) shows a fringe pattern of a femur with bonded-in prosthesis. The similarity at the cross-section l90 mm with that of Figure 12 indicates a perfect fit of the prosthesis in the femur channel.

The drop in stress at higher cross-sections (above 130 mm) is caused by the transition of the load from the femur shaft to the prosthesis stem as investigated in [7].

Figures 14 and 15 are flattened fringe patterns of the femur listed as No.2 in Table 1. Figure 14 was obtained with the prosthesis driven in. Deviation of the loci of external stress values from the generator 0^0(anterior) and that of 180^o (posterior) especially at the plane 130 mm for tension and in the domain 200-250^0 for compression to 20^o can be observed. From this it may be concluded that the position of the prosthesis in the medullar channel is eccentric against the axis of symmetry of the femur shaft. The pattern taken after the extraction of the prosthesis (Figure 15) shows traces

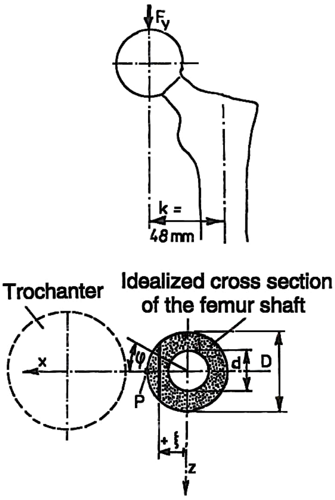

Figure 11. Idealized cross-section of the femur shaft on which equations (1) and (2a) are based

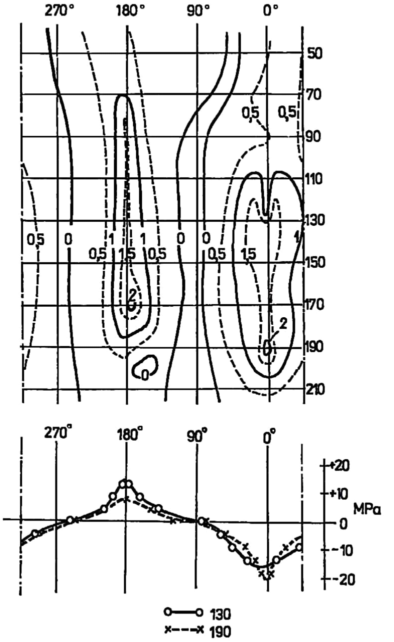

Figure 12. Flattened fringe pattern of the intact femur (No.6 of Table 1). The lower part of the Figure shows the (axial) stress distribution along two cross-sections

of residual stress along the generators 90^o and 270^o, which are remnants of plastic deformation having occurred during the driving-in procedure. Surely a less successful procedure than that of No.5 of Table 1.

Acknowledgement. The authors are indebted to the *PROTETIM Kft. (Orvostechnikai Üzem, Hódmezővásárhely)* for their support and to the *Kaliber Műszer és Méréstechnika Kft. (Budapest)* for putting auxiliary equipment at their disposal to carry out different biomechanical measurements.

References

1. Reilly, D.T. and Burstein, A.H.: The mechanical properties of cortical bone. *Jr. of Bone and Joint Surgery*, **56**(5), (1974), 1001-1022.
2. Lénárt, G., Tóth, I. and Pintér, J.: Experiments on the Hardness of Bone by Vickers Microhardness Measurements. *Acta Biochimica et Biophysica Academiae Scientiarum Hungariae*, **3**, (1968) 205-215.
3. Huiskes, R.: Various Stress Patterns of Press-Fit, Ingrown and Cemented Femoral Stems. Clinical Orthopaedics and Related Research Nr. 261, (1990) pp. 27-58.
4. Fethke, K., Schmitz, K.P. and Plath, J.: Experimentelle und numerische Untersuchungen zur Verankerung von zementfreien Hüftenendprothesenmodellen. VDI-GMA-Bericht 29, (1996) pp.: 75-78.

5. Zacharias, Th., Holzmüller, G., Laue, S., Martin, H., Schmitz, K.P., Fethke, K., Gerhardt, H., Sungu, M. and Both, A.: Automatic Individual Finite-Element Analysis of Cement-less Hip-Implantations. Publication of the University of Rostock 1997.
6. Kirchner, I.: Stress Analysis of Human Femur and Prosthesis, Ph.D. - Thesis. Budapest University for Technology and Economics, 1992. (in Hungarian)
7. Thamm, F.: Investigation of the Contact Stress Distribution Between the Femur Shaft and the Intermedullar Prosthesis. Proc. II. Congress of Mechanical Engineers, (2000) Vol. I. pp.: 319-324. Budapest University for Technology and Economics.
8. Pálfi, P.: The Last Results of Biomechanics of the Bone and their Application in the Numerical Investigation of the Human Femur. Lecture held at the IX^{th} Hungarian Conference on Mechanics. Miskolc. 2003.
9. Beer, R.J., Kodvanj, J., Eberhardsteiner, J., Grienauer, W., Skrbensky, G.and Gottsauner, F.: Mechanical and Optical Aspects of an Implant-Bone Connection in the Femur, Comparison of Two Solutions of Femur-Prostheses. Proc. of 16^{th} Danubia-Adria-Symposium 1999, Cluj-Napoca, pp. 9-10.
10. Baleani, M., Cristofolini, L. and Viceconti, M.: Investigation on Fatigue Limit of Hip Prostheses with Different Surface Treatment. Proc. of 13^{th}. Danubia-Adria Symposium l996. Rajecke Teplice. pp.: 83-84.
11. Callaghan, J.J., Fulghum, C.S., Glisson, R.R. and Stranne, S.K.: The effect of femoral stem geometry on interface motion in un-cemented porous-coated total hip-prostheses. *Int. J. of Bone and Joint Surgery*, **74-A**(6), (1992), 839-848.
12. Cristofolini, L.: Studio Fotoelastico su Femuri Umani con Protezi. Errori Sperimentali devuti al Rivestimento.
13. Thamm, F.: Determination of the Cross-Sectional Data of a Cross-Section of Irregular Shape. Proc. of 17^{th}. Danubia-Adria Symposium, Prague. September, 2000. pp. 321-323.
14. Borbás, L., Thamm, F., Hagymási, M. and Krakovits, G.: Investigation of different designs of femur head prosthesis with respect to the force transition to the femur shaft. XXV AIAS International conference on material engineering. Gallipoli-Lecce, 4–7. September, 1996. pp. 245–248.

Journal of Computational and Applied Mechanics, Vol. 7., No. 1., (2006), pp. 13–22

FINITE ELEMENT ANALYSIS OF SLIPPED CAPITAL FEMORAL EPIPHYSIS AND ITS FIXATION BY A SINGLE SCREW

Ádám Czeglédi and Imre Bojtár
Department of Structural Mechanics
Budapest University of Technology and Economics
Műegyetem rkp. 3-5., H-1521 Budapest, Hungary
`czadam@wiw.hu, ibojtar@mail.bme.hu`

György Szőke
Orthopaedic Department of Semmelweis University
H-1113 Budapest, Karolina út 27., Hungary
`sceleto@freemail.hu`

[Received: October 16, 2004]

Abstract. Slipped capital femoral epiphysis (SCFE) is a relatively common orthopaedic disorder that occurs in early adolescent age. SCFE means the slip of the epiphysis of the upper part of the femoral head along the growth plate (physis). The most important step in the treatment process of femoral disorders that develop due to birth defects or disturbance of growth is early intervention. The most effective treatment procedure of SCFE is the in situ fixation of the slipped epiphysis by a single screw. There is a common solution for the positioning of the pin to achieve the less harmful construction, but it is not confirmed, and was not investigated up to the present. The aim of our work was complex. First, we wished to build up a numerical model of the proximal epiphysis of the femur with the phenomenon of SCFE itself, according to the finite element (FE) method, and then to build up various FE models with differently positioned pins. The aim was to find the optimal position of the screw that generates less stress inside the bone and helps recovering in the most effective way by reducing the possibility of postoperative failures or any impairment.

Keywords: slipped capital femoral epiphysis, finite element method, single screw fixation, biomechanics, 3D modeling, numerical model

1. Introduction

1.1. **Generic review.** Slipped Capital Femoral Epiphysis (SCFE) is one of the most common femoral orthopaedic disorders of pediatrics, affecting mainly adolescents undergoing a growth spurt [1]. The first known written record about SCFE was published by *Ambroise Paré* in 1572 [2], but the definition of treatment and complications started to be better known after Roentgen's development of x-ray in 1895 [2]. Though it usually involves the left hip, according to Klein et al. (1952) bilateral affection is 41%, and 80% by Severin and Billing (1975) [2]. The male-to-female ratio is about

2:1 or 3:1, and females are usually premenarchal [3]. Although the exact aetiology of SCFE is still unknown, the high occurrence in obese patients suggests that the primary evocative cause of development of the disease is the presence of mechanical factors. Pathophysiology of SCFE is the displacement (slip) of the upper part of the femoral head (*epiphysis*) along the growth plate *(physis)* due to shear forces (Figure 1), usually in the varus and anterior direction, but there are a few reported cases of valgus SCFE as well [4]. The *physis* is a cartilaginous plate between the epiphysis and the body of the femur *(metaphysis)*, where cellular activity takes place in the endochondral ossification of long bones, and its ability to resist shear force is the least at the time of puberty. Works studying the tensile and shear properties of the physis pointed out that the thicker it is, the smaller stress it is able to resist [5, 6].

Figure 1. An acute slipped capital femoral epiphysis. The upper part of the femoral head (epiphysis) has slipped along the growth plate, evocating an abnormal state [7]

1.2. **Diagnosis.** Growth plate injuries are usually classified by the *Salter-Harris classification system*, in which five different types of injury are determined. SCFE is a type I fracture, which means pure epiphyseal separation, with the fracture isolated to the growth plate itself [8]. Actually, this description matches only the case of *acute* SCFE (Figure 1). Besides this, the deformation can be *acute-on-chronic*, or *chronic*, depending on the root cause [2]. Acute slip is due to a trauma on the weakened physis, and is quite rare. An acute-on-chronic slip occurs also due to traumatic symptoms, but after an evolved former mild slip. Chronic slip is the most common, and forms gradually with increasing pain. The structure of the growth plate follows the changing position, always remodelling according to the actual phase. Its significance emerges when choosing the treatment method (see later).

Symptoms may include a dull, aching hip, thigh, or knee pain. A typical misleading complaint is knee pain due to the referred pain from the hip joint (Hilton's law). That is the reason why SCFE is missed in several cases, without obtaining hip radiographs [2, 3]. Bilateral anteroposterior (AP) and frog-leg lateral (Lauenstein) (FLL) view hip radiographs must be obtained (Figure 2) in the case of the symptoms mentioned above (obesity, adolescent age, hip pain, knee pain, limp).

1.3. **Treatment.** The first important part of the treatment is early diagnosis. After demonstration of SCFE the goal is a correct *in situ* stabilization of the hip. Since chronic cases are the most common type of SCFE, we will focus only on it.

Figure 2. An AP (left picture) and a FLL view (right picture) x-ray radiograph of a 14-year-old male adolescent. The slip of the epiphysis can be clearly seen on the FL view [9]

Treatment of chronic SCFE cannot happen by simply placing the epiphysis back to its original position, because the blood vessels supplying the growth plate have adapted continually to the slipped position, and the trauma to the vessels caused by a sudden replacement of the epiphysis may lead to avascular necrosis (AVN). To avoid AVN, an in situ fixation must be applied. Though former methods included applying of hip spica for fixing and immobilization, and fixing with multiple pins, the best-known method nowadays is fixation with a single pin (Figure 3) [2]. Besides AVN another common complication is chondrolysis, the atrophy of cartilage, which is usually caused by the penetration of the articular cartilage by a pin (mostly occuring in multiple screw fixation, evidently because of the higher risk of penetration). According to former studies, in order to increase the rate of complication-free operations, a single-screw fixation should be used instead of multiple spinning [1, 2, 3, 10, 11].

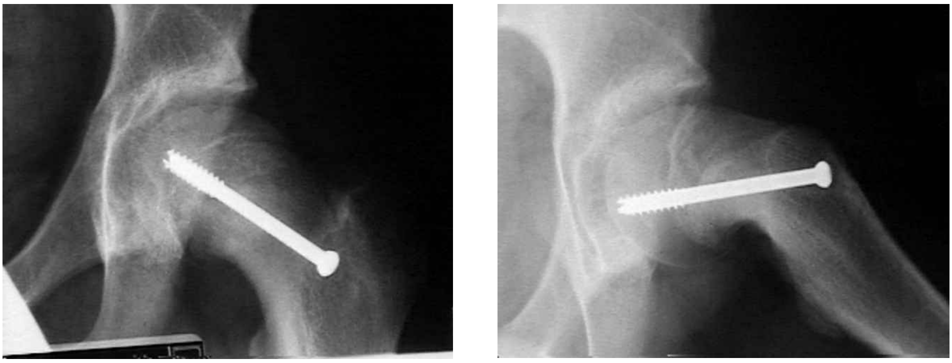

Figure 3. Fixing with a single screw: an AP (left) and a FLL (right) view

1.4. **Objectives.** The fact that the less abnormal stress evolves in the bone, the less the complication rate is, and the faster the recovery of the bone happens, inspired us to find the optimal place and position of the screw in the femur in order to achieve the least stress in both, using the finite element technique. Though it is very rare, there are case reports about single-screw-fixed femur fractures in the subtrochanteric area (following an accident or a trauma) due to stress accumulation in the weakened (the drilled) region (Figure 4.a) [12]. In other cases, after removal of the pin, a traumatic effect was also followed by a subtrochanteric fracture of the femur (Figure 4.a) [13].

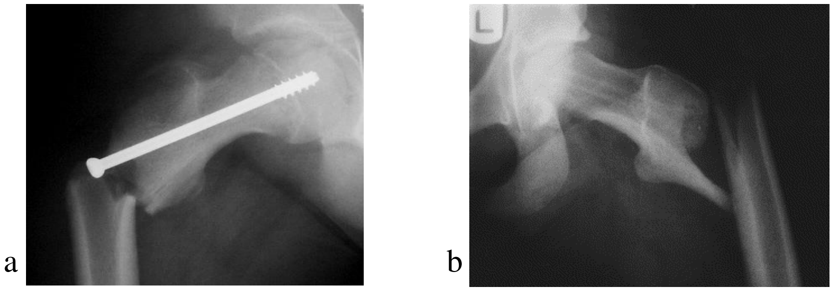

Figure 4. Two subtrochanteric fractures of the femoral shaft, both following an accidental fall: (a) is of a 10 year old girl after a single screw fixation of her SCFE, (b) is of a 14 year old girl 3 weeks after screw removal. Both show a weakening of the subtrochanteric region due to the drill [12, 13]

.

Our first goal was to create the finite element (FE) model of a screw and a femur with a slipped epiphysis. The next step was generating several types of this model, but with differently placed screw tracks in them. Then applying an approximate load condition of weight bearing on each model, by finite element analysis we can compare the obtained stress results, drawing conclusions for the optimal model, thus the optimal screw position.

2. Materials and methods

2.1. **Mesh generation.** The finite element method (FEM) is a numerical technique developed for the solution of complex problems of structural stress analysis, in which the geometrically complex structure is subdivided into a mesh of elements having simple geometry. By means of FEM, a complex problem can be solved approximately based on solving the equations of the simple sub-structures. For the analysis we used the MSC.Marc Mentat software.

The geometry of the healthy femur was provided by the Biomechanics European Laboratory (BEL) Repository with an outer surface of the femur of the visible human man, as derived from computer tomography (CT) data taken on a frozen cadaver (made available by the National Library of Medicine) [14]. Developing of the

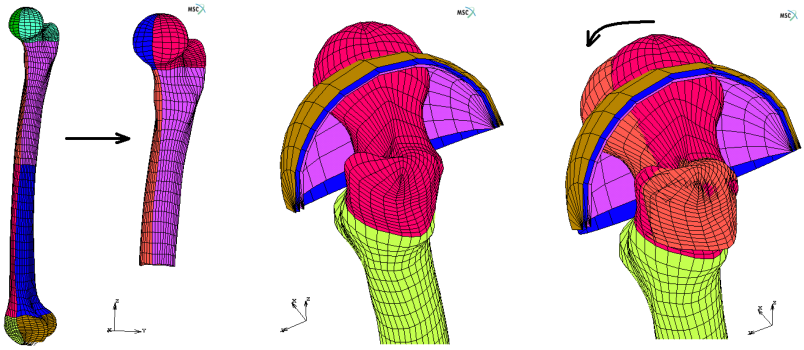

Figure 5. a) Geometric model of the healthy femur, originally determined by eight surfaces, b) proximal epiphysis of the same model, with the three spherical surfaces representing the boundaries of the growth plate, c) and moving the surfaces of the upper part around the center of the spheres

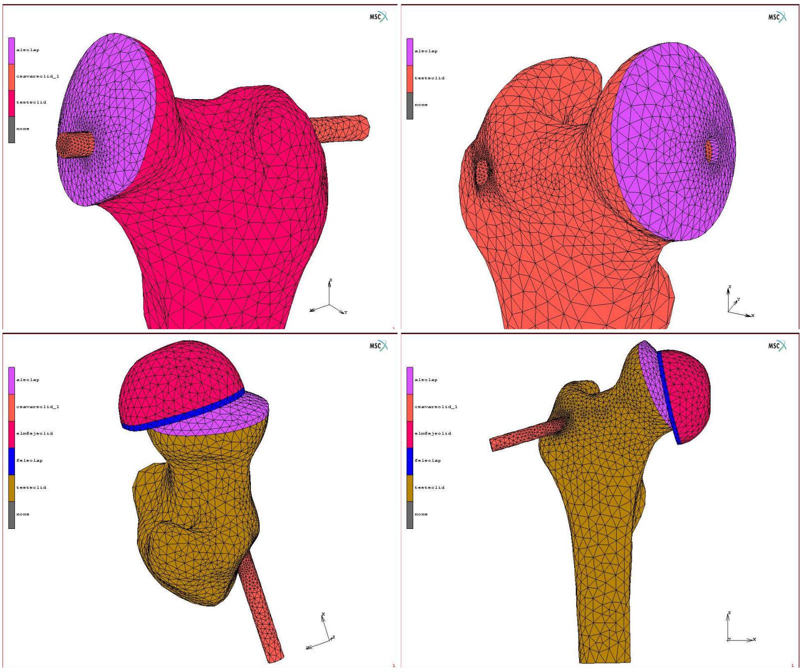

Figure 6. FE mesh of the femur with a slipped epiphysis and the screw, indicating the separately handled parts, and the complexity of the model. It is clearly seen that the epiphysis is displaced in inferior and anterior directions, around the centre of the slipping sphere surface (see Figure 5) by 20-20 degrees

surface of the femur with the slipped epiphysis meant multiple challenges. Besides constructing the phenomena of slipping, we had to built a mesh, which includes the existence of the growth plate itself, and the possibility of handling each body in the model (the slipped epiphysis, the growth plate, the body of the bone and the screw).

The surface of the original geometry was made up of eight different surfaces, but we needed only four of them: the ones constructing the geometry of the proximal epiphysis and the upper part of the body (Figure 6.a). Since with a good approximation the physis is a spherical plate, we applied a sphere surface for the construction of the growth plate. It meant three different surfaces with radii 96, 100, and 104 millimetres with a common center located in the neck. Thus two parts of the growth plate can be generated: one joining the epiphysis, and the other staying in its original position, making the effective slipping surface a part of the surface of a 100 mm radius sphere. In reality, the physis does not separate this way, but for an approximate model it may be accepted. The slipped epiphysis is displaced anteriorly and inferiorly by 20 degrees in both directions. The basic geometric model for further mesh generation is shown in Fig. 5.c. The only changing feature of the further models is the position of the screw. After the intersection of the different surfaces, the mesh of a model with a particular screw position can be created (Figure 6). (The disadvantage of the finite element meshing of these models is that at each model definition the meshing procedure must be repeated, which is time consuming. For future investigations a parametric modelling system is to be created.)

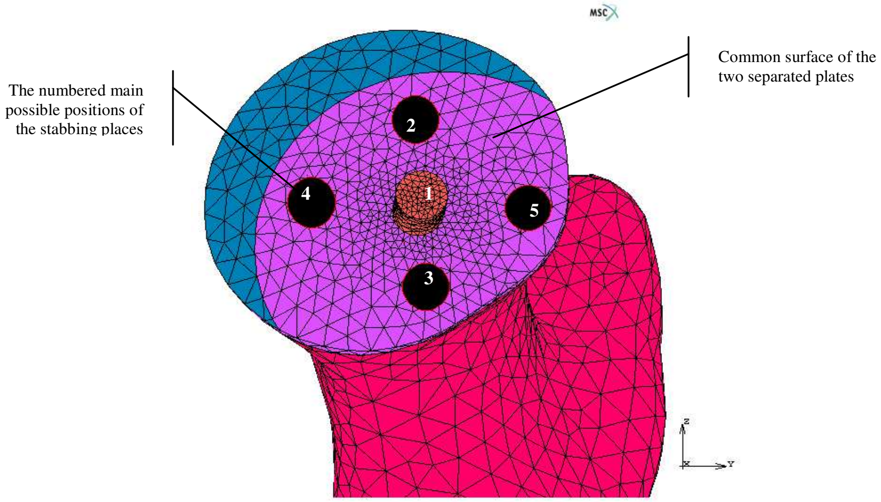

Figure 7. Upper part of the FE model with a specific screw position stabbing the common surface of the separated plates (here the one in the original position can be seen), and the other possible positions that must be investigated to map the complete surface

In Figure 7 a FE model is shown with a screw stabbing through the common surface of the slipped and originally positioned growth plates at about the centre. The other possible stabbing points are shown in Figure 7, which are to be investigated. It can be seen that the parts of the model can be handled separately, enabling them to be given different material properties. We used an isotropic model for all defined materials. Young's moduli for the bone, the growing plate, and the screw were 15, 0.01, and 200 MPa, respectively. Poisson's ratios were 0.3, 0.3, and 0.25. The data of the bone were derived from the average of the cortical and spongeus bone material properties, considering that in reality it is an orthotropic material, but in this work it is approximated with an isotropic one. For the properties of the physis, we did not find any appropriate data in literature, but investigating a femur with healthy geometry, we simulated SCFE by giving weaker mechanical properties to the elements symbolizing the growth plate when applying load on the femoral head representing a bilateral stance phase, and it provided the adequate amount of displacement at Young's modulus about 1/1500 of the bone. The material properties of the screw correspond to the steel's properties.

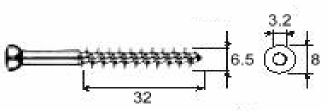

Figure 8. Cancellous bone screw [15]

The model of the screw was created on the analogue of a titanium cancellous bone screw used in surgical practise for fixing SCFE (Figure 8) [15]. The geometrical model of the screw in the FE mesh is approximated with a 6-millimetre diameter cylinder.

The FE models consists of about 78 000 four-noded tetrahedral elements, with the average element edge length varying among 4 (in the epiphysis), 2 (around the drill and the screw) and 6 millimetres (in the body).

2.2. **Boundary conditions.** For the numerical simulation of the bilateral stance phase we used data from a former study (Bergmann et al., 2001). The bottom part of the model was fixed, on the slipped head the following force components were applied relative to body weight: $F_x = -20\%$ (distal); $F_y = 5\ \%$ (dorsal); $F_z = -60\ \%$ (inferior). We took a 70 kg body weight (e.g. an obese child), thus the components were: $\mathrm{F}_x = -14$ kN; $\mathrm{F}_y = 3.5$ kN; $\mathrm{F}_z = -42$ kN. The position of axes is shown in Figure 9.

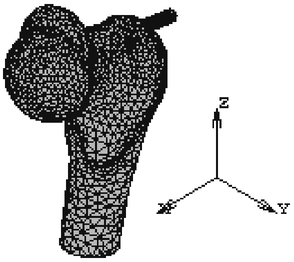

Figure 9. Position of the global coordinate system

3. Results

We could investigate two models so far, the construction of the other models is in process. The model of case 1 and 2 (see Figure 7) were examined for the effect of the boundary condition and load case mentioned above. The most important values are collected in Table 1. The smaller (more favourable) values are marked with grey background and bold. The consequences are clear: the better model related to the peak stress and strain quantities, is the model of case 1. On the other hand, the maximum of the total displacement is smaller in the model of case 2. It may be due to the fact that the centre of gravity of the epiphysis is under the tip of the screw in case 2, which gives higher stability to the epiphysis against load.

		CASE #			
		1		**2**	
		MIN	**MAX**	**MIN**	**MAX**
Displacement in epiphysis	*x [mm]*	0.008466	**0,058340**	-0.047000	0.065560
	y [mm]	0.025000	0.161400	0.026050	**0.138500**
	z [mm]	**-0.118600**	0.029310	-0.125300	0.014570
	total [mm]	0.048010	0.175800	0.041960	***0.169800***
Total shear strain in physis	[−]		**0.005132**		0.005959
Equivalent total strain in physis	[−]		**0.009642**		0.010570
Max principal stress (press) in epiphysis	$[kN/mm^2]$		**0.020540**		0.030830
Max principal stress (press) in metaphysis	$[kN/mm^2]$		**0.039940**		0.057080

Table 1. The values typeset by boldface letters are the favorable ones

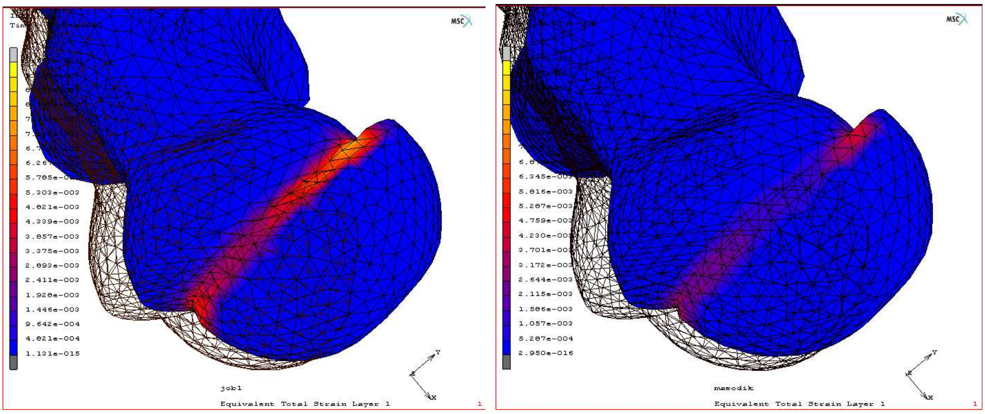

Figure 10. The deformed and undeformed shapes and the total strain distribution of the models of case 1 (left) and case 2 (right). Large values develop in the physis, around the screw the strain values are the smallest

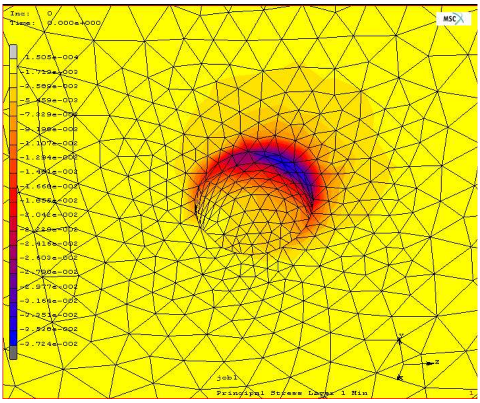

Figure 11. Principal stress (press) value distribution in the whole of the screw in the epiphysis (case 1)

In Figure 10. a) and b) we can compare the deformed shape of the two models and the distribution of total strain. It is clearly seen that the physis is deformed the most, and it is also indicated that the strain distribution in case 1 is more even at the upper border of the plate than in case 2, since in case 2 the tip of the screw is near to the upper surface of the epiphysis, thus it does not allow the physis in its environment to develop high strain values.

4. **Discussion**

Present work showed a way how a common orthopaedic disorder, the Slipped Capital Femoral Epiphysis may be demonstrated and examined through a numerical method, the finite element analysis. Our goal is to answer the question: which screw position is the most favourable in fixation of SCFE? So far there were no experiments to analyze this problem through a numerical method, thus we hope that this research project will answer the question soon in all aspects. With this work we got a step closer to the answer, even if it introduced only two of the planned minimum of five cases. We showed that a screw position close to the upper region of the epiphyis produced higher stress values than the model of a structure with a screw placed in the middle of the common contact surface of the metaphysis and the epiphysis, though the displacement of the epiphysis was greater in the latter case. To find a truly favourable position, we are working on constructing models of case 3, 4, and 5. We hope we can play an important role in establishing the best method to help healing the children who suffer in this disease.

References

1. Aronson, D. D. and Karol, L. A.: Stable Slipped capital femoral epiphysis: Evaluation and management. *J. Am. Acad. Orthop. Surg.*, **4**, (1996), 173-181.

2. Wenger, D. R.: Slipped Capital Femoral Epiphysis. In: Wenger, D. R., Rang, M.: *The art and practice of children's orthopedics.* New York, Raven Press, 1993:331-71
3. Causey, A. L., Smith, E. R., Donaldson, J. J., Kending, R. J. and Fisher, L. C.: Missed Slipped Capital Femoral Epiphysis: Illustrative cases and a review. *J. Em. Med.*, **2**, (1995), 175-89.
4. Rajan R. A., Ibrahim, T., Asirvatham, R. and Aster, A.: *Valgus slipped capital femoral epiphysis. Case report and literature review.* SICOT Online Report E030, 2003.
5. Williams, J. L., Do, P. D., Eick, J. D. and Schmidt, T. L.: Tensile properties of the physis vary with anatomic location, thickness, strain rate and age. *J. Orthop. Res.*, **19**, (2001), 1043-1048.
6. Williams, J. L., Vani, J. N., Eick, J. D., Petersen, E.C. and Schmidt, T. L.: Shear strength of the physis vary with anatomic location and is a function of modulus, inclination, and thickness. J. Orthop. Res., **17**, (1999), 214-222.
7. *Wheeless' Textbook of Orthopaedics.* `http://www.ortho-u.net`
8. *Amersham Health's Medcyclopaedia.* `http://www.amershamhealth.com/medcyclopaedia`
9. Adler, B.: Slipped Capital Femoral Epiphysis. eMedicine.com, Inc., `http://www.emedicine.com`
10. Aronson, D. D. and Carlson W. E.:, Slipped capital femoral epiphysis. A prospective study of fixation with a single screw. *J. Bone Joint Surg. Am.*, **74A**, (1992), 810-819.
11. *Ward, W. T, Stefko, J., Wood, K. B. and Stanitski, C. L.*: Fixation with a single screw for slipped capital femoral epiphysis. *J. Bone Joint Surg. Am.*, **74A**, (1992), 799-809.
12. Orthopaedic Rare Conditions Internet Database (ORCID): *Slipped capital femoral epiphysis - Complication of subtrochanteric fracture.* `http://www.orthogate.com/orcid/scfe.htm`
13. Karagkecrekis, C. B. and Rahman, H.: Subtrochanteric femoral fracture following removal of screw for slipped capital femoral epiphysis. *Injury, Int. J. Care Injured*, **34**, (2003), 320-321.
14. M. Viceconti, Biomechanics European Laboratory: The BEL Repository, Visible Human Male - Bone surfaces `http://www.tecno.ior.it/VRLAB/researchers/repository/BEL_repository.html`
15. Sanatmetal® Manufacturer of Orthopaedic and Traumatologic products, `http://www.sanatmetal.hu/`

Journal of Computational and Applied Mechanics, Vol. 7., No. 1., (2006), pp. 23–39

EXPERIMENTAL AND NUMERICAL BIOMECHANICAL ANALYSIS OF THE HUMAN LUMBAR SPINE

Márta Kurutz
Department of Structural Mechanics
Budapest University of Technology and Economics
H-1521 Budapest, Hungary
`kurutzm@eik.bme.hu`

Béla Fornet
International Medical Center
Dózsa Gy. út 112., H-1062 Budapest, Hungary

Miklós Gálos[1], Árpád Tornyos[2] and Tibor Szabadszállási[2]
[1]Department of Building Materials, [2]Department of Structural Mechanics
Budapest University of Technology and Economics
H-1521 Budapest, Hungary
`mgalos@freemail.hu`

[Received: October 16, 2004]

Abstract. A survey of biomechanical research of the human lumbar spine is presented, conducted by the research group of the Department of Structural Mechanics and the Research Centre for Biomechanics of the Budapest University of Technology and Economics. A complex biomechanical analysis of the human lumbar spine is performed, aimed partly to improve the efficiency of conservative traction therapies and partly to prevent osteoporosis. The former concerns tension, the latter compression of the lumbar spine. As for tension, time-related in vivo elongations were measured during the regular traction hydrotherapy of patients. Based on the experimental results, parameter-dependent viscoelastic numerical tensile models of the lumbar functional spinal units were created for numerical simulation and parameter identification. As for compression, in vitro compression tests were executed for lumbar vertebral bodies, together with measuring bone mineral density and trabecular morphometry, to determine the relations between compressive load bearing capacity and bone architecture. In this paper a survey of these experimental and numerical approaches of biomechanics of the human lumbar spine is reported.

Keywords: human lumbar spine, discs, vertebrae, in vivo elongations, creep, numerical simulation, parameter identification, in vitro compression, morphometry

1. **Introduction**

The present paper gives a survey of the recent results on biomechanical spine research conducted by the research group of the Department of Structural Mechanics and the Research Centre for Biomechanics at the Budapest University of Technology and

Economics. The first part of the report is related to the biomechanics of lumbar traction, to improve the efficiency of conservative traction therapies. The second part is focussed on the biomechanics of lumbar compression, to contribute to the research of osteoporosis.

The goal of the study of lumbar traction was to create a time-related numerical tensile model of human lumbar-lumbosacral motion segments for the numerical simulation of traction therapies. The model has been based on a large-scale experimental analysis of elongations of human lumbar segments in pure centric tension. Time-dependent in vivo elongations of segments L3-L4, L4-L5 and L5-S1 have been measured during the usual traction hydrotherapy of patients, by using a subaqual ultrasound measuring method documented by Kurutz et al. in [1,2]. Elongations of segments were considered to be changes in the distance between two neighbouring spinous processes. Based on the measured elongations of segments in terms of certain biomechanical parameters, parameter-dependent numerical lumbar-lumbosacral L3-S1 FSU models have been created for the numerical simulation and parameter-identification of human lumbar spine segments in traction therapies. 2D and 3D FEM models were created, and the global elongations of FSUs were used for identification of the local material parameters of the component organs of lumbar spine segments.

The goal of the study of lumbar compression was to give the relations between the mechanical properties and bone architecture of human lumbar vertebral bodies, in the framework of osteoporosis research. Image analyses, CT, MR, densitometry and mechanical tests were executed for the lumbar vertebral bodies, to clarify the relations between the compressive load bearing characteristics and bone architecture, in terms of aging and sex. The compressive strength of cadaver lumbar vertebrae was determined by mechanical tests, and the bone architecture was analyzed in CT images. A one-way compressive test was carefully performed on each vertebra up to collapse. The automatically plotted load-displacement diagrams were classified and linearized. Age- and sex-related functions and trends of both strength characteristics and vertebral architecture were obtained for different life periods of osteoporotic elderly. As compressive strength parameters, limit stresses and strains, Young's moduli, proportional stresses and strain limits, ductility and energy absorption capacity were calculated for the lumbar vertebrae L1 and L2, in terms of aging and sex.

In this paper the recent results on biomechanics of lumbar traction and compression are presented.

2. Numerical simulation and parameter identification of lumbar traction

2.1. **Introductory remarks.** Based on the measured elongations of lumbar segments during traction hydrotherapy, parameter-dependent numerical lumbar-lumbosacral FSU models have been created for the numerical simulation of traction treatments.

Suspension hydrotherapy is a Hungarian invention, introduced and described by Moll [4,5,6], and later by Bene [7], while the biomechanics of the therapy has been detailed by Bene and Kurutz [3]. During the traction bath treatment, patients are suspended cervically or by armpit supports in lukewarm water for 20 minutes, loaded by extra lead weights applied on the ankles. In our experiments, cervical suspension has been applied exclusively, since this mode of support provides the most effective stretching load to the lumbar part of the spine, moreover, in this case the effect of muscles can be practically neglected.

2.2. **Force effects in traction hydrotherapy.** Tensile load effects depend on the definition of the tensile deformations. By definition, tensile deformations of segments suspended in water are considered to be a decrease of compressive deformations existing before the treatment. Namely, zero deformation belongs to the common compressed state of segments of the normal upright position of the body. Tensile deformation of segments has been considered to be the change in distance between two spinous processes of neighboring vertebrae.

In the case of cervical suspension, three load effects cause traction deformations along the spinal column: 1. the decompressive force as the removal of the compressive load of the body weight existing before the treatment; 2. the active tensile force due to buoyancy; 3. the extra loads applied for the therapy. In the case of free cervical suspension in water, the effect of muscles can be neglected. The distribution of these traction load effects is illustrated in Figure 1. The compressive loads of the upright standing position are seen to the left of the vertical zero axis, while the active tensile loads of suspension are illustrated to the right.

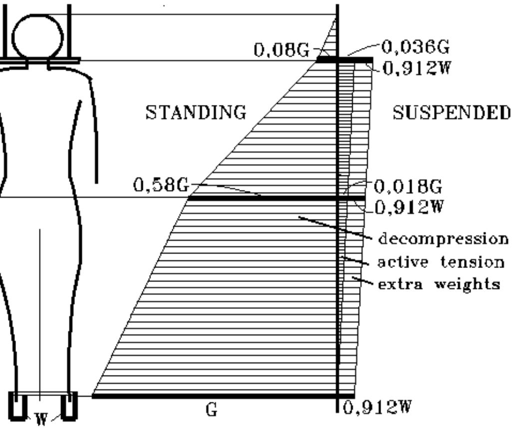

Figure 1. Forces in traction hydrotherapy

The decompressive force is equal to the compressive load acting on the spine before the treatment, in normal upright standing position. This gravitation force increases downwards continuously, starting from zero, namely from the top of the head to the floor, where the total weight G of the body acts. At the cervical level, this force is equal to the weight of the head, that is, about 8% of the body weight. At the lumbar level the decompressive force takes about 58-60 % of the body weight, namely, the weight of the head and trunk together. That is, $F_1 = 0.58G$, seen in Figure 1. For a patient of weight of $G = 700N$, the decompressive force at the lumbar level is about $F_1 = 0,58G = 406N$.

The active tensile force has been calculated in the paper of Bene and Kurutz [3]. It depends on the buoyancy, decreasing continuously along the spinal column, starting from the suspending point where the force has its maximum value, seen in Figure 1. According to [3], being suspended cervically in water without any artificial weights, the value of the active tensile force acting at the suspension point is about

$$0.92G(1 - \rho_w/\rho_b) \ ,$$

where ρ_w and ρ_b are the density of water and the human body, respectively. By considering half of this force at the lumbar level, the active lumbar tensile force reads

$$F_2 = 0.46G(1 - \rho_w/\rho_b) \ .$$

By considering an average human body-density

$$\rho_b = 1040 \ kg/m^3$$

and a normal water density

$$\rho_w = 1000 \ kg/m^3 \ ,$$

it yields

$$F_2 = 0.46G(1 - \rho_w/\rho_b) = 0,018G \ ,$$

seen in Figure 1. For example, in the case of a patient of $G = 700 \ N$ body weight, the lumbar active tensile force yields only

$$F_2 = 0.018 \cdot 700 \ = 12,6 \ N \ \ .$$

Thus, the active tensile load seems to be surprisingly low.

The extra weight loads are applied to provoke a more intensive stretching effect in the lumbar spine. The extra weight load depends on the value, specific weight and the application position of the extra lead weights, detailed also in [3]. Since the extra lead weights are also in the water, their original value W is reduced to

$$F_3 = W \ (1 - \ \rho_w/\rho_l) \ ,$$

due to the buoyancy. By considering the density of the lead to be

$$\rho_l = 11 \ 350 \ kg/m^3 \ ,$$

the extra weight load yields

$$F_3 = W \ (1 - \ \rho_w/\rho_l) = 0.912 \ \mathrm{W} \ ,$$

seen in Figure 1. Thus, by substituting the applied $2 \cdot 20N$ actual weights, that is, $W = 40N$, we obtain

$$F_3 = 0.912 \cdot 40 = 36.48N \ .$$

During the traction bath treatment, the sum of the detailed three tensile forces is to be considered:

$$F = F_1 + F_2 + F_3 = 0.58G + 0.018G + 0.912W \ = 0.598\mathrm{G} + 0.912\mathrm{W} \ ,$$

as seen in Figure 1, by assuming the above-considered densities. By comparing the three component forces, obviously, the dominant stretching load is the decompressive force, if applying cervical suspension. It takes about 97% of the stretching load if no extra loads are applied.

2.3. **Parameter-dependent viscoelastic numerical models of lumbar segments.** Elongation values of lumbar segments L3-4, L4-5 and L5-S1 have been measured. More than 400 lumbar segments of 155 patients have been measured, more than 3000 ultrasound images have been evaluated. The 155 measured subjects have been divided into two groups: 88 patients of less degenerated segments with medically prescribed extra loads, and a group of 67 patients with more degenerated segments without any extra loads. This latter group consisted of patients for whom the extra lead loads have been contraindicated due to certain degeneration of the lumbar segments or discs. Tensile deformability of lumbar segments was measured and evaluated in terms of biomechanical parameters, like sex, aging, body weight and height and body mass index.

Based on the experimental results of lumbar segments L3-4, L4-5 and L5-S1, a so-called general lumbar FSU model L3-S1 has been created for numerical simulations. The functional spinal unit (FSU) consists of two adjacent vertebrae with the disc between them and the related soft tissues, like ligaments, tendons and muscles. FSU model L3-S1 is valid for the lumbar part between segments L3 and S1.

Just being suspended (t=0 min), due to the removal of compression and the buoyancy, unloading of discs and segments occur, thus, even without any extra weights, significant extension was registered. These elongations correspond to the elastic behaviour of segments with a mean value of 0.4-0.8 mm for males, 0.3-0.4 mm for females. Suspended with extra weights (t=3min), 0.6-1.0 mm mean elastic elongations were registered for men, and 0.5-0.8 mm for women. At the end of the treatment (t=20 min), the total mean elongations were 0.9-1.4, and 0.8-1.3 mm with extra loads, and 0.7-1.0 mm and 0.7-0.8 mm without extra weights for men and women, respectively. During the treatment, both the ratio and the value of deformability increased with a decreasing tendency in distal direction.

By considering aging effects, three age groups can be distinguished: young under 40 years, middle aged between 40-60 years and old over 60 years, seen in Figure 2. For the lumbar segment model of less degenerated segments, the mean instant elastic deformations (t=0 min) decrease with aging: 0.90, 0.59, 0.26 mm for males; 0.66, 0.39, 0.21 mm for females; and 0.82, 0.48, 0.23 mm for the whole group, for the three age groups, respectively. At the end of the treatment (t=20 min) the mean deformations decrease with aging again: 1.54, 1.17, 0.37 mm for males; 1.47, 1.19, 0.65 mm for females; and 1.51, 1.19, 0.55 mm for the whole group. The mean final deformations (t=20 min) also decrease with aging, for both males and females. There is no significant difference in age-dependence between men and women. However, the slope of the deformability decrease is slightly larger with increasing treatment time.

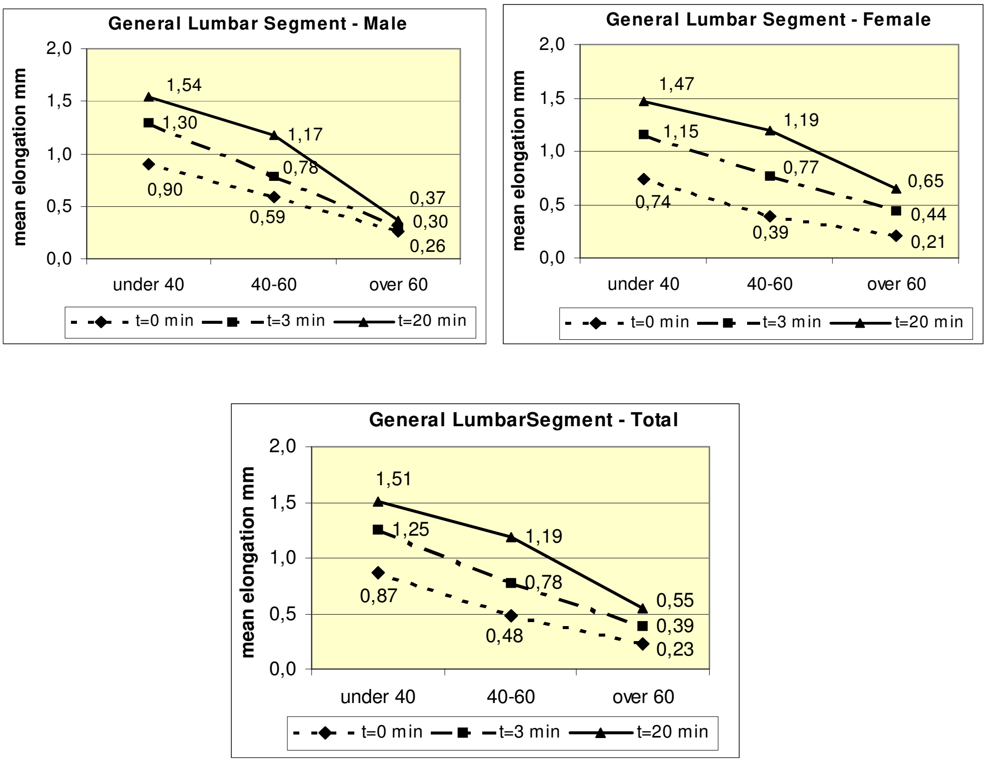

Figure 2. The three parameter spring-dashpot creep model

Since the traction load was constant during the 20 minute-long treatment, a typical creeping process developed and could be documented numerically. The creep process has been measured in the group of patients with less degenerated segments, loaded by 20-20 N extra weights on ankles. For the viscoelastic numerical model, the Poynting-Thomson type three-parameter spring-dashpot model has been used, seen in Figure 3, where spring constants represent the elastic properties and damping coefficients

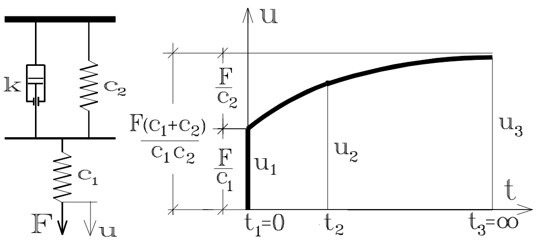

Figure 3. The three parameter spring-dashpot creep model

concern creep effects. The creep function, namely, the deformation in terms of time under constant load yields:

$$u = \frac{F}{c_2}\left(\frac{c_1 + c_2}{c_1} - e^{-c_2 \frac{t}{k}}\right) = \frac{F}{c_2}\left(\frac{c_1 + c_2}{c_1} - e^{-\frac{t}{T}}\right), \qquad T = k\frac{1}{c_2}$$

where T is the time constant. The parameters in this function, namely, the spring constants c_1 and c_2, and the damping coefficient k, were determined by the time-related in vivo measurements. In this way, three elongations have been obtained, from which the parameters of the function u could be calculated. Here we assumed that the last stage at the 20^{th} minute of the treatment concerns the steady state of the creep process. Creep functions of the general lumbar FSU model have been obtained in terms of sex, aging and other parameters.

Table 1. Sex-related parameters and creep moduli of general lumbar FSU model L3-S1

General Lumbar FSU Model LIII-SI				
extra weight 20-20N	units	male	female	total
segments	number	108	128	236
mean age	years	47.9	51.7	50.0
mean body weight	N	758	671	711
mean body height	cm	175	164	169
mean BMI	kg/m^2	24.9	25.1	25.0
elong. at t=0 min u_1	mm	0.66	0.43	0.52
elong. at t=3 min u_2	mm	0.83	0.74	0.78
elong. at t=20min u_3	mm	1.15	1.11	1.13
Creep parameters				
spring coeff. c_1	N/mm	742	1018	887
spring coeff. c_2	N/mm	999	643	756
damping coeff. k	Ns/μm	422	190	245
time constant T	min	7.04	4.93	5.40

Table 1 illustrates the creep moduli of the general lumbar FSU model for numerical purposes, by distinguishing between the sexes. The model is based on the mean values of 108 male, 128 female segments, and overall 236 segments. The mean initial elongation in women is about 66% of the deformation in men. However, the final deformations are quasi equal, since the damping in men is more than double that of women. Spring coefficient c_1 is equal to the initial tensile stiffness. This fact is obvious, by considering the mechanical model seen in Figure 3.

Initial tensile stiffness in males is about 750 N/mm, in females it is about 1000 N/mm. The damping coefficient in males is about 400 Ns/μm, in females it is about 200 Ns/μm. Consequently, after an initially smaller deformability in females, larger creep elongations occur. The final viscoelastic elongations are quasi equal.

Table 2. Age-related parameters and creep moduli of general lumbar FSU model L3-S1

General Lumbar FSU Model LIII-SI				
extra weight 20-20 N	units	under 40 yrs	40-60 years	over 60 yrs
segments	number	35	161	40
mean age	years	26.5	50.7	67.5
mean body weight	N	713	721	670
mean body height	cm	176.7	169.0	160.3
mean BMI	kg/m^2	22.9	25.2	26.0
elongation, t=0 min, u_2	mm	0.94	0.52	0.25
elongation, t=3 min, u_2	mm	1.25	0.78	0.39
elongation, t=20 min, u_2	mm	1.51	1.19	0.55
Creep parameters				
spring constant c_1	N/mm	492	899	1748
spring constant c_2	N/mm	812	698	1456
damping coefficient k	Ns/μm	186	256	417
time constant T	min	3.82	6.11	4.77

Creep behaviour of the general lumbar segment model L3-S1 is significantly different in terms of aging, as seen in Table 2, considering the three age groups. It was numerically verified that the initial stiffness increases, consequently, deformability decreases with aging,. Similarly, damping coefficients also increase, thus, creep deformability decreases with aging. These tendencies are valid for both sexes.

2.4. **Numerical simulation in traction.** As the first step of the numerical simulation, we checked the measured elongations by a simple 2D FEM model. Since the healthy spine segment is a symmetrical structure, the simple 2D model was related to the sagittal plane of the FSU. For the material constants we used the results by Antosik et al. [9] and Ciach et al. [10,11]. For the Young's moduli E and Poisson ratio í, the following data were used. For the vertebral cancellous bone E=1000 MPa and í=0.4, for the vertebral cortical bone E=15000 MPa and í=0.4, for the disc annulus E=5 MPa, í=0.35, for the disc nucleus E=1 MPa, í=0.49, for ligaments E=40 MPa and í=0.35 were considered.

The geometrical data of the FSU were obtained by measuring a typical lumbar segment. The height of a vertebra (including end-plates) was 25 mm, the height of the disc was 8 mm. The end-plates (containing both vertebral and disc bony end-plates) was 3 mm. The support of the structure was along the inferior surface of the lower vertebra. The load was distributed along the superior surface of the upper vertebra.

For the general behaviour of the segment complex, we assumed a bilinear material law. We assumed that the decompression takes place by large stiffness that is valid for compression, and for the active tension and extra weights, we assumed a smaller stiffness. Thus, 500 MPa for compression and 5 MPa for tension were applied as disc moduli.

In the loading phase of decompression, we applied 400 N that caused about 0.1 mm (0.097 mm) segment elongation. For the active tensile load and extra lead weight load together, we applied 49 N. The additional elongation was about 0.5 mm. These results were in good agreement with our measured elongations.

The numerical simulation confirmed our suspicion that in spite of the fact that the active tensile forces compared with the decompressive forces are very small, even a small value of extra weight load can cause a large elongation in the spine segment and disc. Thus, extra loads should be handled very cautiously.

As the second step of the numerical simulation, we refined the 2D FEM model to simulate the viscoelastic creep process, by applying NASTRAN software. For the viscoelastic numerical model, the Poynting-Thomson type three-parameter spring-dashpot models were used. Creep behaviour and creep curves of the general lumbar segment model L3-S1 were significantly different in terms of aging and sex.

For parameter identification, the NASTRAN model has been improved to a 3D configuration of FSU. The segment model has 35 000 nodal points with the relating 110 000 equations. Figure 4 illustrates the mesh of the FSU-model and the mesh of the component organs: cross-section of vertebrae, the disc and the separated ligaments.

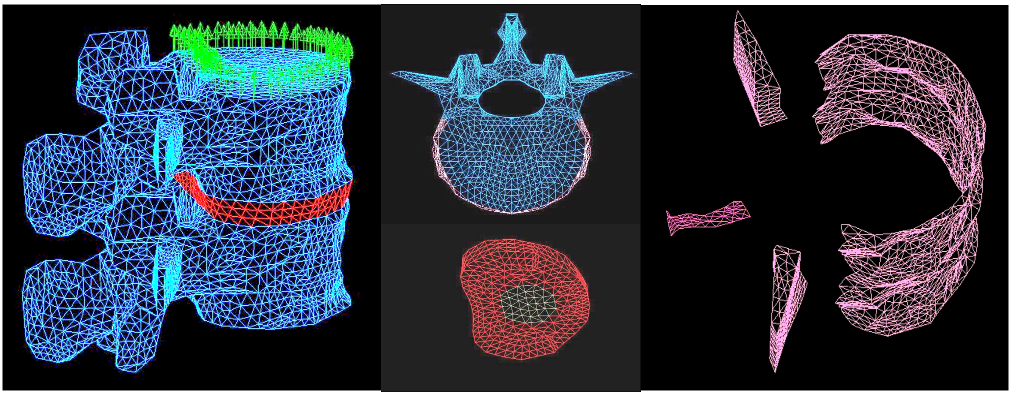

Figure 4. FEM mesh of the FSU model, vertebrae, disc and ligaments

Parameter identification aims to determine the in vivo controlled tensile behaviour and tensile material moduli of the component organs of lumbar segments that are completely missing in the international literature. Namely, except for the results of Kurutz et al. [1,2,3] there can hardly be found any experimental results for in vivo human lumbar spine in pure centric tension, when the effect of muscles are excluded. In the parameter identification process, the in vivo measured global elongations of the lumbar segment complex are used for control parameters in determining the material moduli of the local component organs. In this process, the material moduli of certain organs are kept constant while the material parameters of other organs are considered to be the variables of the problem. Under these parameters, numerical simulation is investigated, and those results are considered to be realistic and are accepted that lead to the in vivo measured elongations. The intervals of material moduli used in parameter identification are as follows: cortical bone 1-20GPa, trabecular bone: 50-1000 MPa, disc annulus 5-500 MPa, disc nucleus 1 MPa, ligaments 10-100 MPa.

The parameter analysis shows that Young's modulus of the annulus has a significant effect on the deformability of the segment complex, and we can hardly assume that the tensile elastic modulus of the annulus is far smaller than the compressive one. This result seems to be evident since the basic property of the annulus is its resistance to compression. Another observation is that changing the stiffness of the cortical bone has no significant effect on the deformability of segments. However, the Young's modulus of the annulus has practically no effect on the stresses occurring in the cortical or trabecular bone, however, it has a significant effect on the stresses of the nucleus and annulus itself.

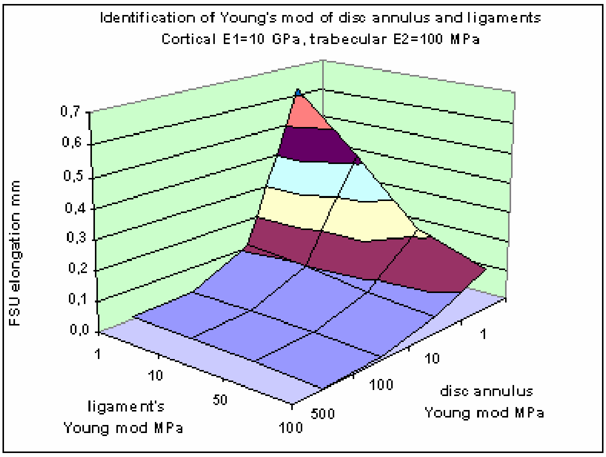

Figure 5. Parameter-identification of Young's moduli of disc annulus and ligaments

In Figure 5 the global elongation of the segment complex is illustrated in terms of the Young's moduli of the disc annulus and the ligaments. By considering the in vivo measured elongation, for example, to be 0.3 mm, the level of this elongation can be projected to the basic coordinate plane to show the possible coincidence of the real Young's moduli of the above mentioned organs.

3. Compressive strength and bone architecture of lumbar vertebrae

Compressive strength of cadaver lumbar vertebrae was determined by mechanical tests, and their bone architecture was analyzed by CT images. Age-related functions and trends of both strength characteristics and vertebral architecture were obtained for different life periods of the osteoporotic elderly.

54 cadaver lumbar L1 and L2 vertebrae without posterior elements were obtained from the spines of 16 males and 38 females. The age of males was between 47-87

years (mean age 65.6 year); the age of females was between 43-93 years (mean age 74.2 year).

Before mechanical testing, areal bone mineral density (aBMD in g/cm^2), CT and MRI analysis were performed for each vertebra. The CT images were used to analyze the bone architecture, to measure the diameters, the distribution and density of trabeculae. The measurements have been repeated in the coronal and sagittal plane and in the horizontal cross-sectional plane of vertebrae.

For mechanical testing, the two end-plates of vertebrae were cleared away, so that the upper and lower planes of vertebrae were parallel and smooth. In this way, the original height of vertebrae decreased by two times 1-4 mm. The reduced height and the upper and lower cross-sectional areas were measured and registered. The average of the two measured cross-sectional areas has been considered to be the cross sectional area of each vertebra.

A one-way compressive test was carefully performed on each vertebra up to the collapse. No cyclic loading and no unloading were performed. The measuring limit of the tester was 12.5 kN with accuracy of 3%. Compressive deformations were measured in three points, by angle of 120 degree from each other, with 0-5 mm measuring limit.

The automatically plotted load-displacement diagrams were linearized, and the related stress-strain diagrams were classified.

3.1. **Experimental compressive strength characteristics of lumbar vertebrae.** Table 1 contains the mean values of the given material or geometrical properties and the measured mechanical characteristics of vertebrae L1 and L2, by distinguishing between sexes. The mean values of areal BMD verify that the analyzed vertebrae belong to the osteoporotic class.

Table 3. Mechanical characteristics of lumbar vertebrae L1-L2 in compression

Lumbar vertebrae L1-L2		Males	Females	Total
Mean age	years	65.6	74.2	71.7
Areal bone mineral density (aBMD)	g/cm^2	0.446	0.347	0.376
Cross sectional area of vertebrae	mm^2	1609	1359	1436
Height of specimen without end-plates	mm	21.9	19.0	19.9
Break load	N	4322	2437	2995
Proportional stress	MPa	2.0	1.3	1.5
Proportional strain	%	3.3	2.9	3.0
Young's modulus	MPa	91	67	74
Limit stress	MPa	2.7	1.9	2.1
Limit strain, ductility	%	5.0	4.9	4.9
Energy absorption capacity	Joule	1.63	0.97	1.18

It can be seen that there is a significant difference in the load bearing properties of males and females, namely, the compressive load bearing capacity of women is about 30% smaller than that of men. The break load of women is 40-50% smaller than that of men. Moreover, since the cross-sectional areas of women are only 15%

smaller, consequently, both the proportional and limit stresses are 30-40% smaller in women than in men. The limit stresses were about 2.7 MPa for men, and 1,9 MPa for women. Young's moduli of women are about 20-30% smaller than that of men. At the same time, there is no significant difference between the sexes in the proportional or limit strains and in duclility. The proportional strains are equally about 3%, the limit strains are equally about 5%. However, there is a significant difference again in the energy absorption capacity of men and women: women have about 1 Joule, namely 35-45% smaller absorption capacity than men with 1.6-1.7 Joule. This comes partly from the smaller limit stresses and partly from the smaller volume of vertebrae of females.

Lindahl [13] and Hansson et al. [12] presented the main compressive strength characteristics of the cancellous bone of lumbar vertebrae. The proportional stress was 1.37-4.0 MPa, the proportional strain 6.0-6.7%, Young's modulus 22.8-55.6 MPa, the limit stress 1.55-4.60 MPa, and the limit strain was 7.4-9.5%. These results concern the cancellus core of vertebrae, proving that due to the high ductility, there is the trabecular bone that is responsible for the energy absorption ability of vertebrae to avoid injury in the case of an accidental dynamical load. Based on compressive tests of lumbar vertebrae, Tanaka et al. [18] found the value of limit stress between 0.14-4.54 MPa.

Figure 6 illustrates the linear approximation of the age-related decline of limit stresses of vertebrae L1-L2, between 43-93 years, by distinguishing between the sexes. A similar tendency has been found for the other strength parameters, as well.

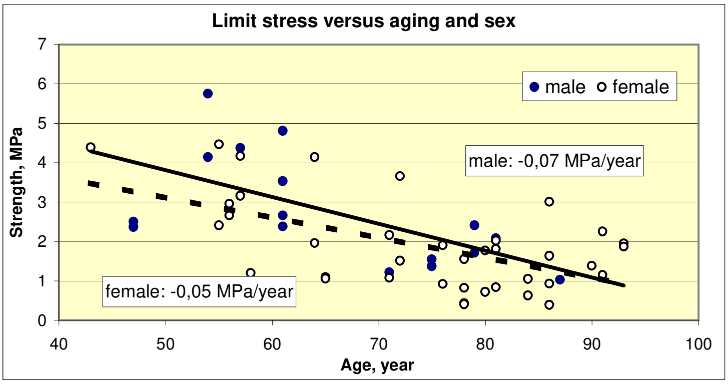

Figure 6. Linear approximation of age-related decline of limit stress of vertebrae L1-L2

Mosekilde [17] emphasized that a basic understanding of age-related changes in the quality and strength of vertebral bone is crucial. Based on his combinative study he demonstrated that age is the major determinant of vertebral bone strength, mass, and microarchitecture. There is, after the age of 50 years, a higher tendency for disconnection of the trabecular network in women than in men.

By applying linear approximation, the decrease trends of the strength characteristics can be calculated numerically. Table 4 contains the values of decrease trends for a year of aging, related to the total analyzed age span, for the main strength parameters, that is, break loads, limit stresses, Young's moduli and energy absorption capacity.

Table 4. Numerical decrease trends of compressive mechanical characteristics with aging

Lumbar vertebrae L1-L2		Males	Femals	Total
Break load	N/year	-90	-56	-80
Limit stress	Mpa/year	-0.07	-0.05	-0.06
Young modulus	Mpa/year	-2.8	-1.7	-2.1
Energy absorption	Joule/year	-0.029	-0.022	-0.028

It can be observed in Table 4 that the decrease trends of women are smaller than those of men. The decrease trends of women are about 60% of those of men, equally for break load, limit stress Young's modulus and energy absorption capacity.

For sex-independent analysis, for the total group, by applying linear approximation for the total age interval 43-93 years, for break load, the approximate mean decrease trend can be considered to be -80 N for a year of aging. For limit stresses, the approximate mean decrease trend can be considered to be -0.06 MPa/year, for compressive Young's moduli -2.1 MPa/year, for energy absorption capacity -0.028 Joule/year.

As a conclusion of our experiments, during the age period between 40-90 years, the strength properties decrease by 60-70% for both sexes. According to the linear regression analysis of McCaldren et al [14] related to the age-dependent changes in the compressive strength of cancellous bone of 255 femoral cadaver specimens from donors in age of 20 to 102 years, the compressive strength decrease yields 8,5% in each decade of aging. This means that the 80 years long decrease period yields 68% of total strength decrease. Mosekilde [16] also mentioned that the decline in strength of the whole vertebral body during normal aging for both men and women is 70-80%. These results are in agreement with our results.

Table 5 contains the correlation coefficients of all compressive mechanical strength characteristics with aging for males and females, respectively.

Table 5. Correlation between strength characteristics and aging

Male **Female**	Age	Break load	Limit stress	Limit strain	Young's mod.	Prop. stress	Energy absorb.
Age	**1.0**	-0.57	-0.62	-0.00	-0.55	-0.64	-0.37
Break load	-0.52	**1.0**	0.9	-0.05	0.95	0.95	0.80
Limit stress	-0.57	0.97	**1.0**	0.03	0.96	0.98	0.80
Limit strain	-0.12	0.11	0.13	**1.0**	-0.18	0.01	0.25
Young's modulus	-0.52	0.86	0.91	-0.17	**1.0**	0.93	0.72
Proportional stress	-0.55	0.93	0.97	0.13	0.86	**1.0**	0.68
Energy absorption	-0,51	0.78	0.76	0.35	0.62	0.64	**1.0**

Obviously, there is a negative correlation between the compressive strength parameters and aging for both sexes, since the load-bearing capacity decreases with aging. The age-dependence in the proportional and limit stresses and in the Young's moduli is slightly larger for men than for women. However, practically, there is no correlation with aging in strains for men, and only a small correlation is found for women. The age-dependence of energy absorption capacity seems to be larger for women than for men.

These results agree with the results of Mori [15] who found the correlation between aging and compressive Young's modulus of normal patients to be -0.527, based on compression tests of bone samples of vertebra L3. Similarly, based on compressive tests of lumbar vertebrae, Tanaka et al. [18] found the correlation significant, namely, -0.66 between limit stresses and aging.

3.2. **Trabecular bone architecture of lumbar vertebrae.** Bone architecture and bone mineral density are in close relation with each other. Figure 7 illustrates the age-related decrease of the areal bone mineral density (aBMD) of the measured vertebrae, by distinguishing between the sexes. It can be observed that in the age period of the experiment (43-93 years) the analyzed vertebrae belong to the strongly osteoporotic group, moreover, women are in an advanced osteoporotic state, having lower bone mineral density than men. It can be concluded that the areal bone mineral density decreases significantly with aging. The decrease trend can be numerically verified by applying linear approximation.

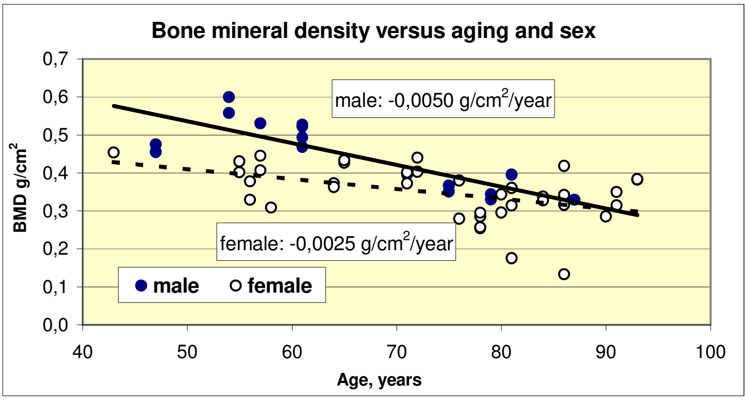

Figure 7. Age-related decline of areal bone mineral density of vertebrae L1-L2

Obviously, all compressive strength parameters increase significantly with bone mineral density, or, inversely, decrease significantly with the age-related decrease of aBMD.

Figure 8 illustrates the age-related weakening of trabecular architecture, namely, the loss of trabecular diameter and the parameters of several trabecular areal ratios.

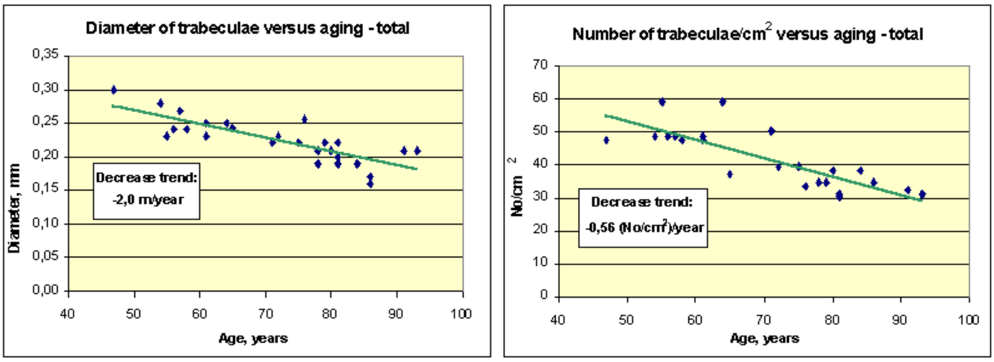

Figure 8. Age-related decrease of trabecular architecture of vertebrae L1-L2

Linear approximation of age-dependence of trabecular diameters, and areal ratio of trabecular bone are illustrated.

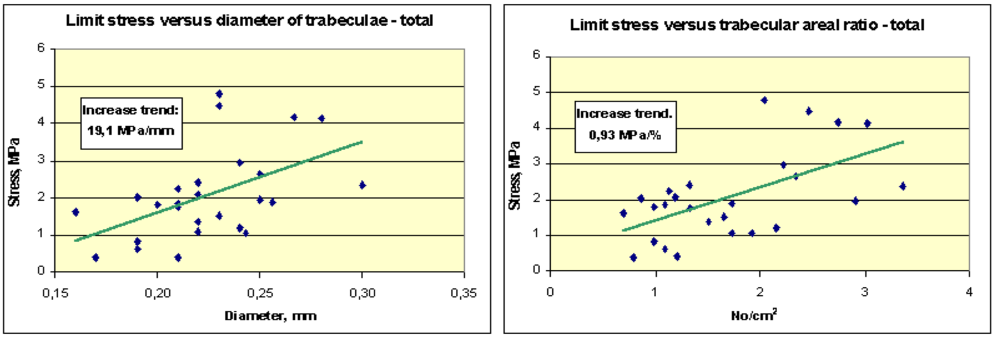

Figure 9. Increase of limit stress versus trabecular architecture of vertebrae L1-L2

In Figure 9 the linear approximation of the increase of limit stress in terms of the diamater and areal ratio of trabeculae is illustrated. It verifies numerically the effect of trabecular weakening on the compressive strength of vertebrae in osteoporosis.

4. **Summary**

Tension and compression analysis of the human lumbar spine was presented. Based on in vivo experiments, a parameter-dependent viscoelastic numerical tensile model of lumbar-lumbosacral functional spinal units was created for numerical simulations of traction therapies. At the sane time, in vitro compression tests and CT morphometry of lumbar vertebrae were compared to obtain the relation between the compressive load bearing capacity and bone architecture of osteoporotic segments.

For the numerical creep models of human lumbar-lumbosacral segments L3-S1, elastic and damping moduli have been calculated for tension. By means of the initial elastic moduli and the damping parameters, it has been numerically shown that the rigidity of segments increases significantly with aging. Moreover, the time related difference between the deformation propagation in male and female patients depends on the different damping properties of sexes. The values of elastic and creep parameters are approximate, since they are very sensitive to the measured deformations. However, their ratio and tendency provide very important information for the numerical simulation of traction therapies. The numerical simulation and parameter-identification of human lumbar spine segments were presented in centric tension. 2D and 3D FEM models were used, and the global elongations of FSUs were used for identification of the local material parameters of the component organs of lumbar spine segments.

Since there are no in vivo experimental results in the international literature for the human lumbar spine segments or discs in pure centric tension when the effect of muscles can be excluded, the results presented may attract the interests of the biomechanical analysts of the human lumbar spine.

The compressive strength of osteoporotic lumbar vertebrae has been measured in vitro, in terms of aging, sex and bone architecture. It has been concluded that the load-bearing capacity decreases with aging, thus, there is a significant negative correlation between compressive strength parameters and aging for both sexes. By applying linear approximation for age-dependence, the decrease trends of compressive strength characteristics were calculated numerically. Bone mineral density and the parameters of trabecular bone loss were compared with the measured compressive strength characteristics.

Acknowledgement. The present study has been supported by the projects OTKA T/022622, T033020, T046755, ETT- 257/2000.

References

1. Kurutz, M., Bene, E., Lovas, A., Molnár, P. and Monori, E.: Extension of the lumbar spine, measured during weightbath therapy, (In Hung.), *Orvosi Hetilap*, **143**(13), (2002), 673-684.
2. Kurutz, M., Bene, E., Lovas, A., Monori, E. and Molnár, P.: In vivo deformability of human lumbar spine segments in pure centric tension, measured during traction bath therapy. *Acta of Bioengineering and Biomechanics*, **4**(Suppl.1), (2002), 219-220.
3. Bene, E. and Kurutz, M.: Application and biomechanics of traction bath, (in Hung.), Orvosi Hetilap, **134**, (1993), 1123-11293.
4. Moll, K.: Treatment of discus hernia with so-called "weightbath" therapy. (In Hung.), *Orvosi Hetilap*, **94**, (1953), 123-126.
5. Kurutz, M.: Die Behandlung der Discushernien mit den sogenannten "Gewichtsbadern". *Contempl. Rheum.*, **97**, (1956), 326-329.
6. Moll, K.: The role of traction therapy in the rehabilitation of discopathy. *Rheum. Balneol. Allerg.*, **3**, (1963), 174-177.
7. Bene, E.: Das Gewichtbad, *Z. Phys. Med. Baln. Klim.*, **17**, (1988), 67-71.

8. Kurutz, M., Bene, E. and Lovas, A.: In vivo deformability of human lumbar spine segments in pure centric tension, measured during traction bath therapy. *Acta of Bioengineering and Biomechanics*, **5**(1), (2003), 67-92.
9. Antosik, T. and Awrejcewicz, J.: Numerical and experimental analysis of biomechanics of three lumbar vertebrae. *Journal of Theoretical and Applied Mechanics*, **3**, (1999), 37.
10. Ciach, M. and Awrejcewicz, J.: Finite element analysis and experimental investigations of the intervertebral discs in the human and porcine lumbar spinal segment, Proc. Conf. Biomech. Modelling, Computational Meth., Experiments and Biomedical Applications, Lodz, Dec. 7-8. 1998.
11. Ciach, M., Maciejczak, A., Awrejcewicz, J. and Radek, A.: A comparison of two surgical techniques using finite element model of cervical spine before and after discectomy with interbody bone graft, Proc. Conf. Biomech. Modelling, Computational Meth., Experiments and Biomedical Applications, Lodz, Dec. 7-8. 1998.
12. Hansson, T.H., Keller, T.S. and Panjabi, M.M.: A study of the compressive properties of lumbar vertebral trabeculae: effects of tissue characteristics. *Spine*, **12**, (1987), 56.
13. Lindahl, O.: Mechanical properties of dried defatted spongy bone, *Acta Orthop. Scand.*, **47**, (1976), 11.
14. McCaldren, R.W., McGeough, J.A. and Court-Brown, C.M.: Age-related changes in the compressive strength of cancellous bone. The relative importance of changes in density and trabecular architecture. *Bone Joint Surg. Am.*, **79**(3), (1997), 421-427.
15. Mori, S.: Effect of aging on compressive strength of lumbar trabecular bone in hemodialyzed and non-hemodialyzed patients. *Nippon Jinzo Gakkai Shi.*, **36**(6), (1994), 752-761.
16. Mosekilde, L.: The effect of modelling and remodelling on human vertebral body architecture. *Technol. Health Care*, **6**(5-6), (1998), 287-297.
17. Mosekilde, L.: Age-related changes in bone mass, structure, and strength effects of loading. *Z. Rheumatol.*, **59**(Suppl.1), (2000), 1-9.
18. Tanaka, Y., Kokubun, S., Sato, T., Iwamoto, M. and Sato, I.: Trabecular domain factor and its influence on the strength of cancellous bone of the vertebral body. *Calcif. Tissue Int.*, **69**, (2001), 287-292

Journal of Computational and Applied Mechanics, Vol. 7., No. 1., (2006), pp. 41–58

NUMERICAL ANALYSIS OF GIANT BRAIN ANEURYSMS

Ferenc Nasztanovics, Brigitta Tóth
Biomechanical Center
Budapest University of Technology and Economics
H-1521 Budapest, Hungary
`naszta@biomech.bme.hu, brigitta.toth@index.hu`

György Paál, Imre Bojtár
Biomechanical Center, Department of Structural Mechanics
Budapest University of Technology and Economics
H-1521 Budapest, Hungary
`paal@vizgep.bme.hu, ibojtar@mail.bme.hu`

István Szikora
National Scientific Institute of Neurosurgery
H-1145 Amerikai u. 57.
`h13424szi@ella.hu`

[Received: September 14, 2004]

Abstract. This paper focuses on the analysis of the haemodynamic pattern and biophysical properties of cerebral aneurysms, diagnosed and delineated in living human individuals. An aneurysm is a bulging out of part of the wall of a blood vessel. The aim of the research is to delineate flow patterns inside the aneurysm and its parent artery, to estimate stresses at critical points of the aneurysm wall, to model the haemodynamic effect of different surgical and endovascular tools in order to define the optimal one in a particular case, and to estimate the likelihood of a later aneurysm rupture.

Keywords: haemodynamic pattern, biophysical properties of cerebral aneurysms

1. Introduction

Brain arterial aneurysms are common forms of arterial deformation occurring in about 5% of the adult population. The aneurysm is a bulge along the artery hanging there embedded in the surrounding tissue. In most situations it usually appears around a joining of two arteries. This bifurcation is the part of the supplier of the brain vascular bed system so if its blow-out (rupture) causees an incalculable chain reaction, there is no safe solution without any side-effect to protect the patient against unpleasant consequences, see for instance [1],[2],[3]. In the majority of the cases the patient does not notice anything about the presence of the aneurysm, in some cases, however, the aneurysm bursts leading to stroke and immediate death. Figure 1 presents a photo of an aneurysm obtained by planar angiography, and its characteristic places in the human brain.

At present, the therapeutic decision for unruptured aneurysms is made purely on the basis of the size and location of the lesion in the belief that those are the only factors influencing the likelihood of rupture. The literature results providing a basis for this practice have been seriously criticized by many and clinical decision is frequently based on the personal experience and judgment of the physician. Our work will provide the physicians - and the patients - with a much more accurate prognosis of the disease that will allow for a more appropriate decision regarding treatment. We note that besides its scientific merit, the potential for providing information about the prognosis of the disease and about the optimal technique for its treatment would greatly enhance the value of modern angiography systems.

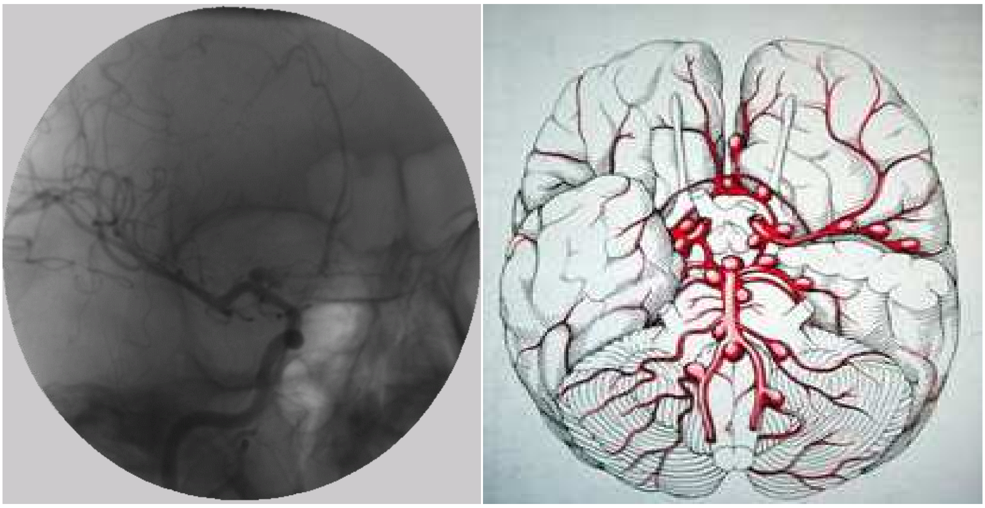

Figure 1. (a) Photo of the aneurysm (b) The usual places where brain anurysm form

The description of the flow in arteries (also called haemodynamics,[4],[5],[6]) is one of the great challenges of current fluid mechanics research. The flow is unsteady, the walls are flexible with complex elastic properties, the geometry is very complicated. The living tissue reacts to fluid mechanical changes in unpredictable ways, which again influences the flow properties. The elastic deformation of the wall interacts with the flow in a complex way. The non-newtonian properties of blood also play a role in some cases. There are substantial variations in all the parameters from patient to patient so it is difficult to draw general conclusions. In addition, it is extremely difficult to make in vivo measurements to test theories or simulations.

Nevertheless the importance of this area cannot be overestimated – the most important causes of death in developed countries are arterial diseases. Research budgets and public interest in this subject grow continuously.

2. Research strategy

The geometrical and morphological data as well as physiological parameters of the patients collected at the National Institute of Neurosurgery are combined with physiological information of the vessel wall and aneurysm wall provided by the Department of Human Physiology. The calculation of the material parameters of the aneurysm wall there is the first step of our work. Based on this information, the researchers of the Center for Biomechanics prepare 3D coupled (flow and solid) finite element models of the aneurysms. On these models we run strength calculations in order to predict their mechanical strength (allowable blood pressure, etc.), and to compare the effects of different possible medical treatments. This is the second step of the research activity.

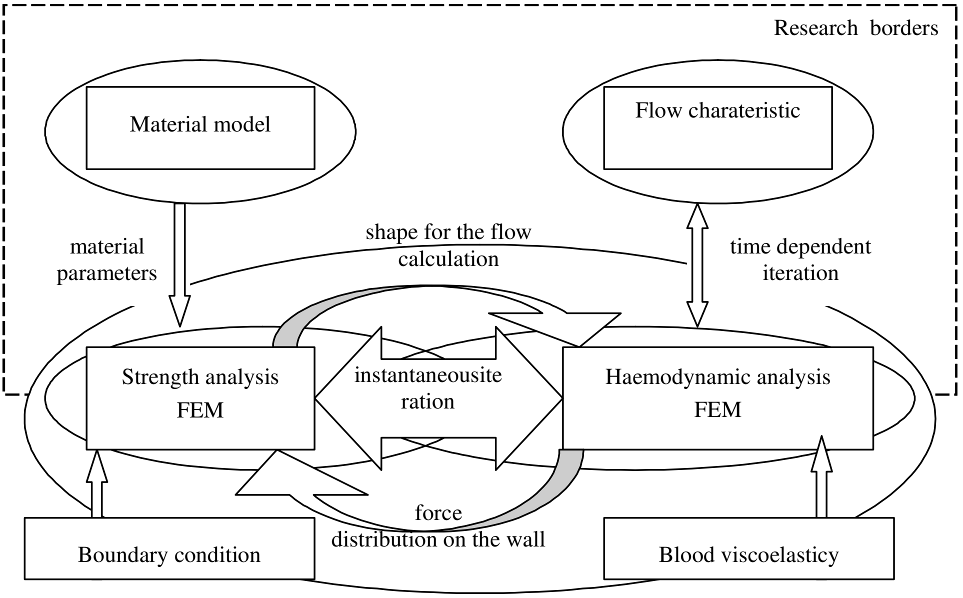

Figure 2. Basic mechanism of the model

The long-term goal of this research program is to work out non-intrusive diagnostic tools detecting the presence of aneurysms and to assess the necessity of medical intervention. To this end detailed studies are being performed on the fluid mechanical behaviour of the blood near aneurisms on the one hand, and on the elasticity behaviour of the blood vessel wall on the other hand. These are performed using commercial software tools.

Since the process is highly unsteady and the elastic deformation of the wall and the flow in the arteries are highly coupled, the solution is far from trivial. After performing simulations on rigid models for fluid mechanics on the one hand and wall only models for the elasticity studies, the next step will be to couple the two phenomena and the data will be transferred in each time step to provide time-dependent boundary conditions for the two simulations.

When the simulations in the realistic model are considered to be reliable the haemodynamic and the wall stress data are carefully analysed and diagnostic criteria for intervention are derived, see Figure 2.

3. Material parameters

3.1. **Introductory remarks.** One of the problems is that the different constitutive models in the literature are based on data from different types of arteries [7],[8],[9]. Moreover, cardiovascular disease like human cerebral aneurysm can only be studied in detail if a reliable constitutive model of the arterial wall is available. In order to get acquainted with the sterically inhomogenous behavior of cerebral aneurysms, we measured the mechanical properties of the aneurysm tissue as a function of strain in different regions (thin and thick) and in different directions (meridional and circumferential). The strips from aneurysm showed typical hyperelastic-plastic behavior at the stress-relaxation tests. Meridional thin strips exhibited greater tensile strenghts than the meridional thick ones, see [10].

Moreover in this point first we have summarized the theoretical framework as a background for the description of the arterial wall mechanics. We begin by giving a brief description of the histological structure of arterial walls and outline the general characteristic of the mechanical response of arteries. An artery is practically treated as a thick-walled circular cylinder which is appropriate for the analysis of bending, extension, inflation and torsion of the tube. In the literature some models are able to provide a full three-dimensional description of the state of stress in the artery, but the large number of material constants may lead to parameter identification problems. Several models use geometrical simplifications as well.

3.2. **Human arterial histology.** In general, arteries are subdivided into two types: elastic and muscular arteries [11],[12]. Elastic arteries have relatively large diameters and are located close to the heart, while muscular arteries are located at the periphery. We focus our attention on the microscopic structure of muscular arterial walls composed of three distinct layers. These are the tunica intima, the tunica media and the tunica adventitia.

The tunica intima is the innermost layer of the artery. A single layer of endothelial cells lines the arterial wall. In healthy young arteries the intima is very thin and does not have any significant contribution to the solid mechanical properties of the human arterial wall. But it is known that pathological changes of the intimal components are associated with significant alterations in the mechanical properties.

The tunica media is the middle layer of the artery and from a mechanical perspective it is the most significant layer. It consists of a complex three-dimensional network of smooth muscle cells and elastin and collagen fibrils. The media is separated by the so-called fenestrated elastic laminae into concentrically fiber-.reinforced layers, and this middle layer is separated from the intima and the adventitia by the internal elastic laminae and the external elastic laminae, respectively. The smooth muscle cells, the elastin and collagen fibrils and the fenestrated elastic laminae constitute a continuous almost circumferentially oriented fibrous helix. This arrangement gives high strength and resilience.

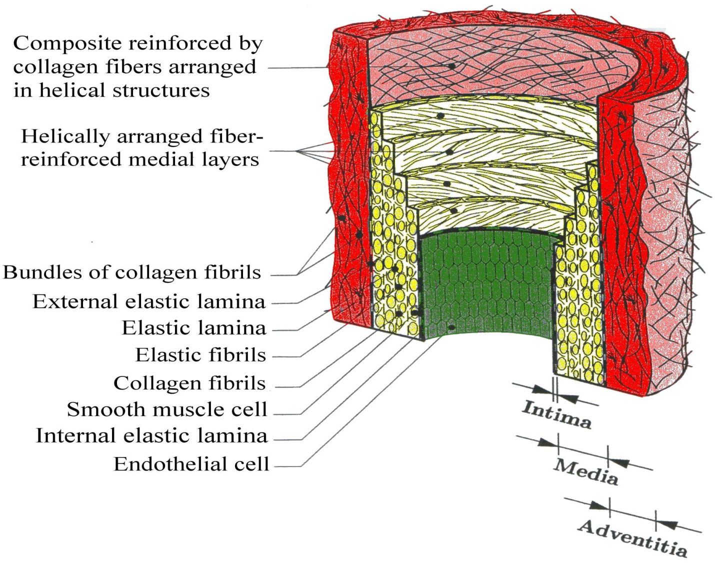

Figure 3. Model of the major components of a healthy artery composed of three layers: intima, media and adventitia

The tunica adventitia is the outermost layer of the artery. The thickness of the adventitia depends on the type of the artery and its topographical site. Apart from a histological ground substance it also consists of fibroblasts, fibrocytes and thick bundles of wavy collagen fibrils, which are arranged in helical structures. They contribute to the strength and stability of the arterial wall. The adventitia is less stiff in a low pressure domain than the media but at higher pressures the collagen fibrils straighten out and the adventitia turns into a stiff tube.

3.3. **Typical mechanical behavior of arterial walls.** The reliability of material parameters is related to the quality of the experimental data [13],[14],[15],[16]. It may come from in vivo tests or from in vitro tests. In in vivo tests the artery is observed under real life conditions, while in vitro tests mimic real loading conditions in a physiological environment. The complex anisotropic material response can only be measured in an in vitro experiment, though the exact physiological circumstances may be rather difficult to simulate.

Arteries do not change their volume in the physiological range of deformation, for this reason they can be regarded as incompressible – rubber-like – materials. Therefore we have set ourselves the task to determine the mechanical properties from biaxial tests: uniaxial extension tests are certainly insufficient to completely quantify the mechanical behavior of arterial walls.

The mechanical behavior of arteries depends on physiological and chemical environmental factors, therefore they were tested in appropriate oxigenated, temperature controlled salt solutions.

Whereas the composition of arterial walls varies along the arterial tree so that the shape of the stress-strain curve for blood vessels depends on the anatomical site, the general mechanical characteristics are the same.

The artery is a heterogeneous system and it can be regarded as a fiber-reinforced composite biomaterial. The layers of the arterial walls are composed mainly of an isotropic matrix material (associated with the elastin) and two families of fibers (associated with the collagen), which are arranged in symmetrical spirals. We note that we have made a simple independent finite element simulation of the biomechanical behavior of the arterial wall to check the effect of the different parameters in different constitutive equations.

3.4. **Continuum-mechanical framework.** Fundamental equations are essential to characterize kinematics, stresses and balance principles, and hold for any continuum body [17]. Generally we use a functional relationship as a constitutive equation, which determines the state of stress at any point x of a continuum body. Our main goal is to study various constitutive equations within the field of solid mechanics appropriate for approximation techniques. We follow the phenomenological approach. It describes the macroscopic behavior of living tissue as continua.

Numerous materials can sustain finite strains without noticeable volume changes. Such types of material can be regarded as incompressible, which is a common idealization in continuum mechanics. Materials which keep the volume constant throughout a motion are characterized by the incompressibility constraint $J = 1$, where J means the determinant of the gradient tensor. In general, these materials are referred to as a constrained materials.

The stress response of hyperelastic materials is derived from the given strain-energy function Ψ:

$$\sigma_{ij} = \frac{\partial \Psi\left(\varepsilon\right)}{\partial \varepsilon_{ij}}$$

In the next subsection we summarize the most important energy functions frequently used in biomechanics.

3.5. **Ogden model for incompressible rubber-like materials.** The postulated strain-energy function Ψ describes the changes of principal stretches

$$\Psi = \Psi\left(\lambda_1,\, \lambda_2,\, \lambda_3\right) = \sum_{p=1}^{N} \frac{\mu_p}{\alpha_p}\left(\lambda_1^{\alpha_p} + \lambda_2^{\alpha_p} + \lambda_3^{\alpha_p} - 3\right)$$

where N is a positive integer which determines the number of terms in the strain-energy function, μ_p are constant shear moduli and α_p are dimensionless constants, $p = 1, \ldots, N$. Only three pairs of constants are required to give an excellent correlation with experimental stress-deformation data.

We find after differentiation that the three principal values σ_a of the Cauchy stresses have the form:

$$\sigma_a = -p + \sum_{p=1}^{N} \mu_p \lambda_a^{\alpha_p}, \quad a = 1,\, 2,\, 3$$

where p is a scalar not specified by a constitutive equation. It is to be determined from a boundary condition of the problem considered.

3.6. **Mooney-Rivlin model for incompressible rubber-like materials.** The Mooney-Rivlin model uses the setting $N = 2$, $\alpha_1 = 2$, $\alpha_2 = -2$. Using the strain invariants I_1, I_2 with the constraint condition $I_3 = \lambda_1^2\lambda_2^2\lambda_3^2 = 1$ we obtain that:

$$\psi = c_1\left(\lambda_1^2 + \lambda_2^2 + \lambda_3^2 - 3\right) + c_2\left(\lambda_1^{-2} + \lambda_2^{-2} + \lambda_3^{-2} - 3\right) = c_1\left(I_1 - 3\right) + c_2\left(I_2 - 3\right)$$

with the constants $c_1 = \mu_1/2$ and $c_2 = -\mu_2/2$.

Derivatives of the strain-energy function of the Mooney-Rivlin model with respect to the invariants I_1 and I_2 give the simple associated stress relations:

$$\boldsymbol{\sigma} = -p\mathbf{I} + 2c_1\mathbf{b} - 2c_2\mathbf{b}^{-1}$$

where the strain tensor b^{-1} is the inverse of the left Cauchy-Green tensor $\mathbf{b}$, which is defined by the help of the strain gradient tensor $\mathbf{F}$ as:

$$\mathbf{b} = \mathbf{F}\mathbf{F}^T$$

($\mathbf{F}$ is on the left). It is an important strain measure in terms of spatial coordinates. $\mathbf{I}$ denotes the second-order unit tensor.

3.7. **Neo-Hookean model for incompressible rubber-like materials.** The neo-Hookean model applies the setting $N = 1$, $\alpha_1 = 2$. Using the first principal strain invariant I_1 we find that:

$$\Psi = \mathrm{c}_1\left(\lambda_1^2 + \lambda_2^2 + \lambda_3^2 - 3\right) = c_1\left(I_1 - 3\right)$$

with the constant $c_1 = \mu_1/2$. The strain-energy function involves a single parameter only and relies on phenomenological considerations.

Derivatives of the strain-energy function of the neo-Hookean model with respect to the invariants I_1 give the simple associated stress relations:

$$\boldsymbol{\sigma} = -p\mathbf{I} + 2c_1\mathbf{b}\ ,$$

where the strain tensor $\mathbf{b}$ is the left Cauchy-Green tensor, and $\mathbf{I}$ is the unit tensor.

3.8. **Some other constitutive models for arterial walls.** We note that in the literature other versions could be found for the constitutive equations of human artery walls, see for instance works by Delfino, Vaishnav, Fung [19] and especially Holzapfel [13],[18]. In these models the active mechanical behavior of arterial walls is governed mainly by the intrinsic properties of elastin and collagen fibers and by the degree of activation of smooth muscles, however the passive mechanical behavior is quite different and is governed mainly by the elastin and the collagen fibers. Most constitutive models describe the artery as a macroscopic system and capture the response near the physiological state.

In our program – based on our laboratory tests – we applied the most common strain-energy functions, mentioned above in Subsections 3.2-3.7. In Figure 4 our uniaxial and biaxial test machines can be seen, both of them are connected to the computer. In our recent numerical simulations the test results of the biaxial specimens were not applied yet, because of the yet insufficient number of experimental results.

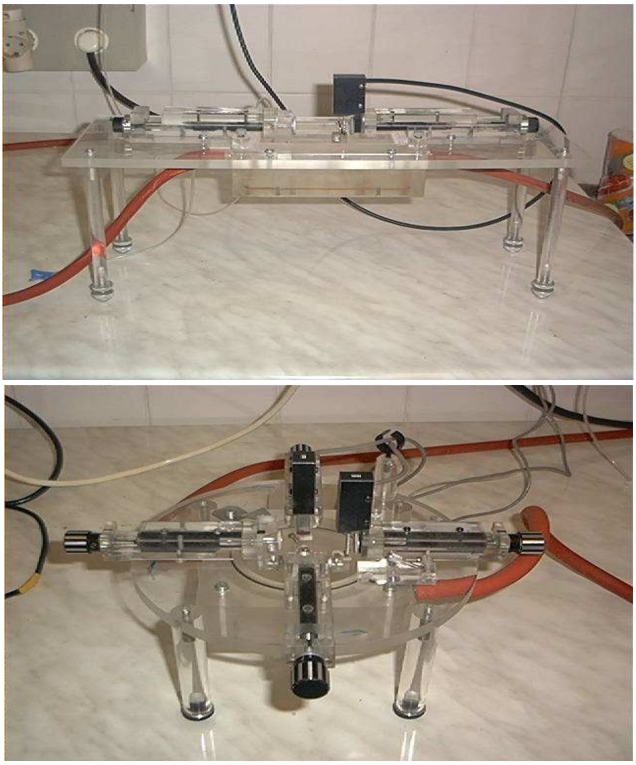

Figure 4. Uniaxial and biaxial laboratory test machines

In Figure 5 we show some characteristic experimental diagrams. We had 53 different specimens from 30 persons. All tests were made immediately after the operations, within 24 hour intervals. Meridian and circumferential strips were cut and measured from the aneurysma sack.

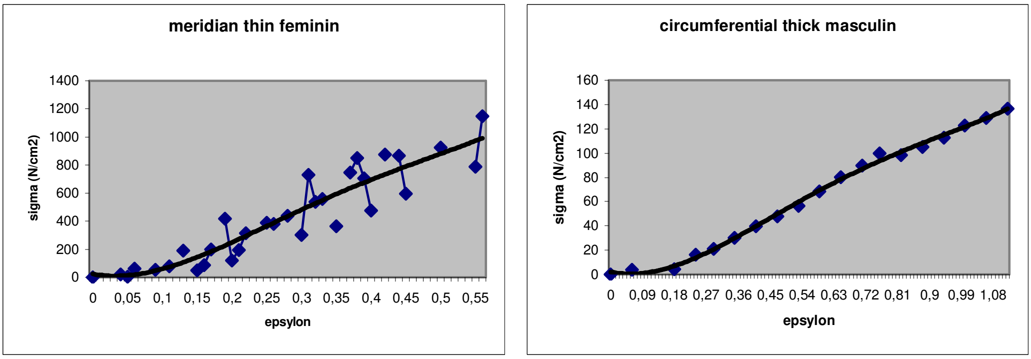

Figure 5. Diagram of an uniaxial stress-strain curve for meridian and circumferential aneurysma strip in passive condition (based on tests performed in the authors' laboratory). The thick solid line indicates the approximate engineering response of the biomaterial.

Based on these experiments we calculated the material parameters of the Mooney-Rivlin and Neo-Hooke nonlinear hyperelastic models, see Table 1. With the help of simple finite element tests all material parameters were checked.

Table 1. Mooney-Rivlin and Neo-Hooke material parameters calculated from experiments

	Mooney-Rivlin				**Neo-Hooke**	
	C10	**C10**	**C01**	**C01**	**C10**	
	Woman	*Man*	*Woman*	*Man*	*Woman*	*Man*
circumferential-thick	5,2	1,6	1,3	0,4	6,5	2,0
circumferential-thin	17,9	14,4	4,5	3,6	22,4	18,0
Meridian-thick	8,7	6,5	2,2	1,6	10,9	8,1
Meridian-thin	22,3	20,3	5,6	5,0	27,9	25,3

4. Flow simulations

4.1. **How to simulate.** The simulations were carried out using the commercial flow simulation software CFX 5.6. It solved the incompressible unsteady Navier-Stokes equations using the finite volume method. The fluid had a constant density of 1050 kg/m^3 and a dynamic viscosity of 0.003 kg/ms so that the non-newtonian behavior of blood was ignored. The simulations were performed on the simplified model introduced in [5]. Figure 6a shows that the aneurysm head sitting on a pipe bifurcation is inclined so that it stands out of the plane of the pipes. In order to have well-defined boundary conditions, the original geometry was extended by straight pipe sections (Figure 6b).

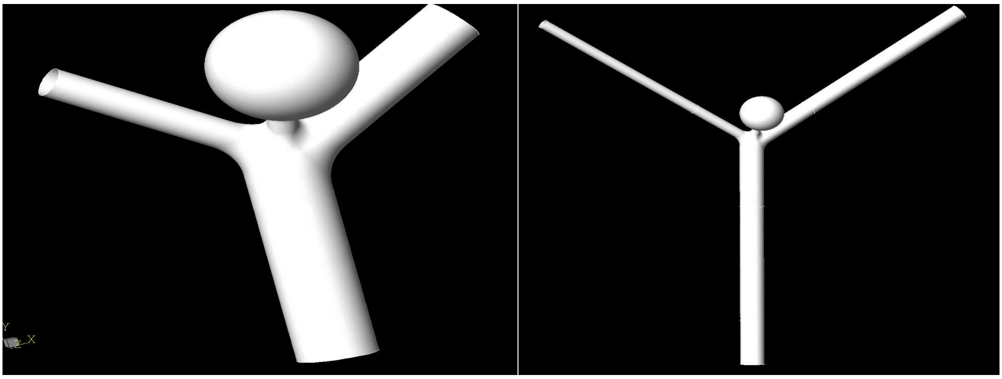

Figure 6. (a) Model of idealized aneurysm geometry (b) Extended geometry

The simulated volume was divided into about 200.000 mainly tetrahedral elements, except near the walls, where prismatic elements were used to achieve better boundary layer resolution. The wall was assumed to be rigid and standard no-slip boundary condition was used with automatic near-wall treatment. The mesh was made significantly finer in regions of high curvature, i. e. near the aneurysm neck.

The inlet boundary condition was an analytic mass flow rate-time function resembling a real blood pulse cycle (Figure 7). Two cycles were simulated and the second one was used to extract results. The extension on the inlet pipe was used in order to be able to use a uniform inlet velocity profile and not to interfere with the flow developing later.

At a later stage of the project the inlet boundary condition will be derived directly from ultrasonic velocity measurements in real patient arteries. These signals are at present very noisy and require filtering and smoothing in order to use them in simulations.

The outlet boundary condition presents an interesting problem. A time-dependent boundary condition cannot be given, since the time delay and the deformation of the pulse passing the aneurysm region cannot be said a priori. On the other hand, far away from the artery, on the level of capillaries, the pressure reaches a nearly constant value. Therefore a constant pressure outlet boundary condition was used and all the blood vessels lying between the region of interest and the region of constant pressure have been simulated by a pipe section filled with "porous material". This had the function to dissipate the pressure variations and arrive at a constant pressure in the end.

The time period was divided into twenty equal time steps and this time step was used for the simulation. The temporal discretisation as well as the spatial discretisation were second order.

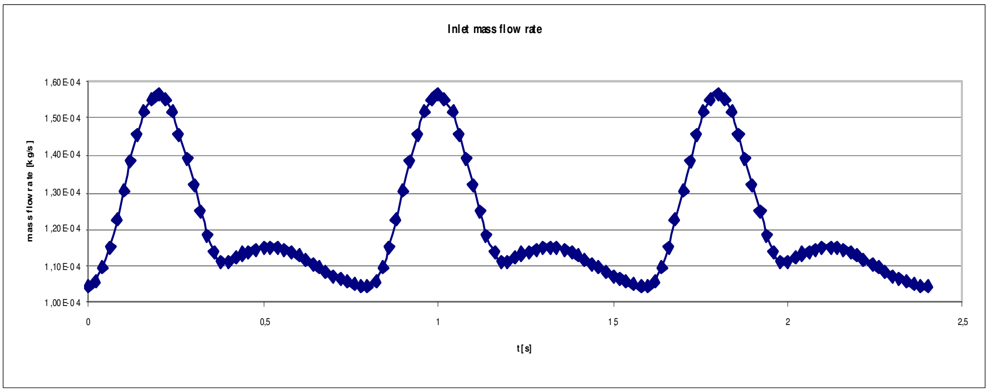

Figure 7. Inlet boundary condition

4.2. **Results of the idealized geometry.** Some preliminary results are shown to demonstrate the capabilities of the simulations. This idealization may be far from the real aneurysm but it is simple enough for testing the model behavior. The idealized model is built up of three cylinders and a sphere skew penetration. The bottom cylinder is the inflow pipe, and the two others are the outflow. Three different types of penetration were applied. The angle and the diameter of the cylinders were changed.

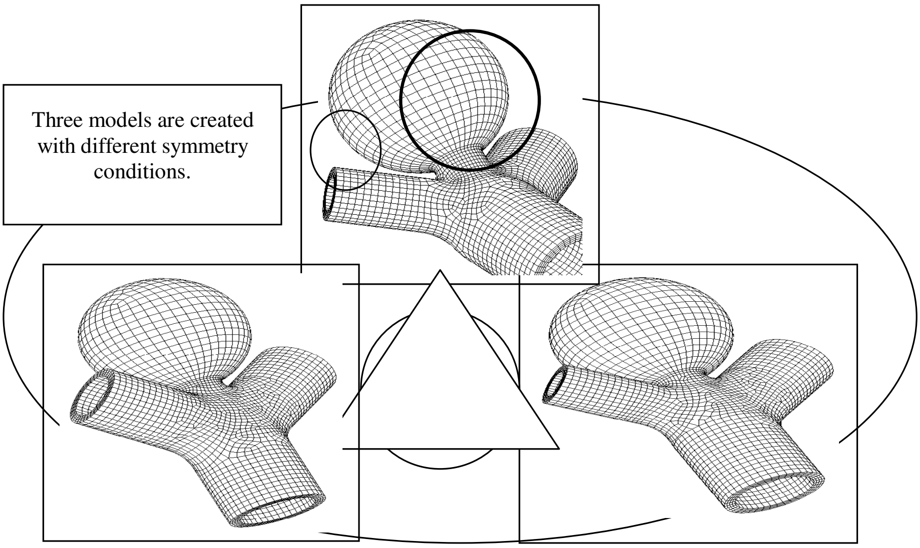

Figure 8. Different ideal geometries

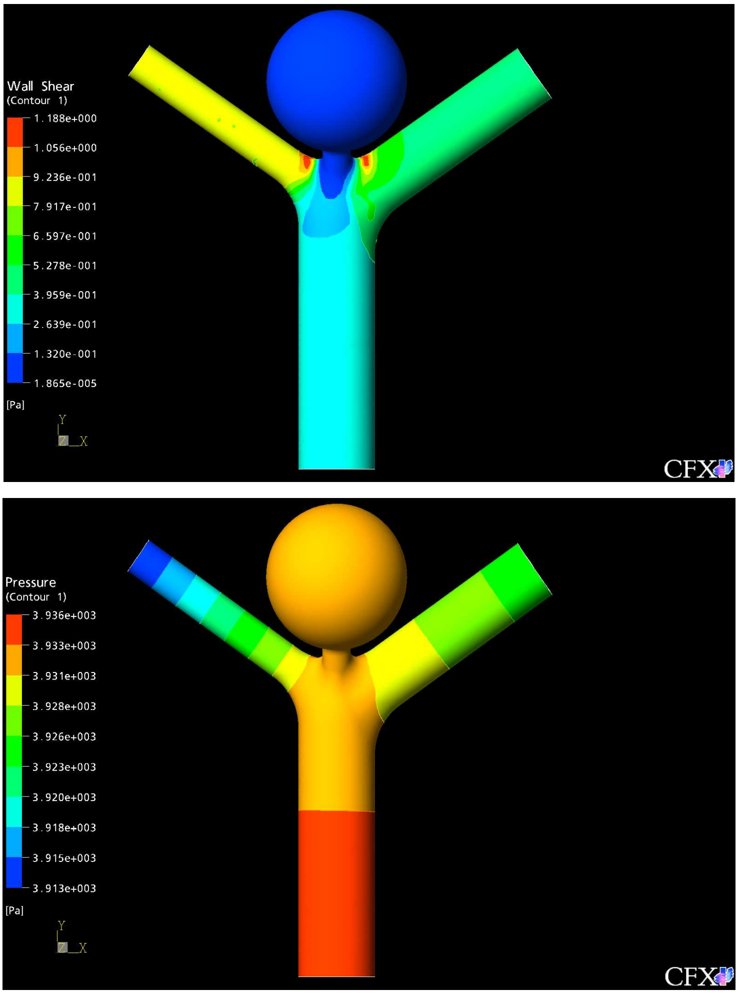

Figure 9. Wall shear stress and pressure distribution along the aneurysm walls

All the figures shown are from an arbitrary time step, practically at the peak systole. Results in all the other time steps look qualitatively similar, only the magnitudes of the variables change significantly.

Figure 9a shows the wall shear stress. In the aneurism 'bulge' itself the shear is negligible, which is a consequence of the negligible flow velocities there (not shown in the paper). In the incoming and outgoing pipes the shear stress is constant. Note that higher wall shear values can only be detected at the 'shoulders' of the aneurysm.

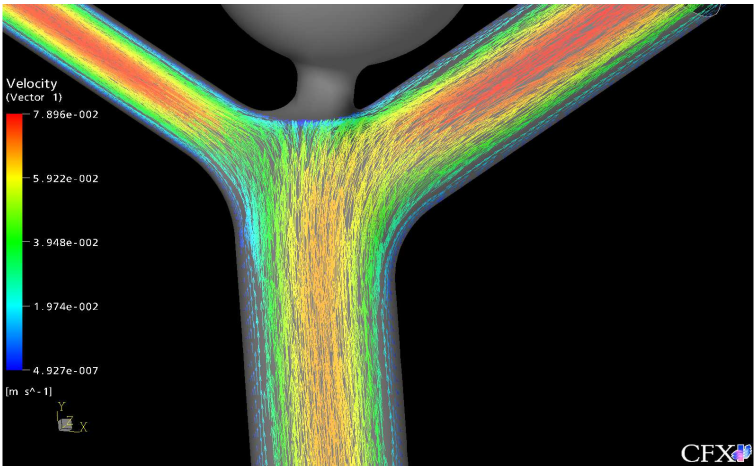

Figure 10. Blood velocity vector field in the model mid-plane

This, however cannot be the cause of the rupture since experience shows that it usually happens along the 'equator' of the aneurysm.

The wall pressure distribution (Figure 9b) shows the expected linear decrease in the pipe regions and a practically constant value in the aneurysm region. It is expected that a better model provides here more information.

Finally the velocity distribution (Figure 10) also presents no dramatic phenomena. The flow is smooth, well-behaved, without any vortices and separations. A more refined model is expected to reveal more anomalies here as well.

4.3. **Results of the real geometry.** With the help of angiography we can build a model of an existent aneurysm, and this model was used for Finite Element Analysis calculation. The angiography allows us to build a real three dimensional model with the original geometry. Using the data of aneurysm material parameters the system could help the physicians to analyze the case, whether it needs an urgent operation or not. This way of geometrical modeling is much more complicated than the previous one. Many different tests are needed to declare that the system works reliably. Moreover, different material models and boundary conditions need more and more calculations. On this part of the task we have just started to work. The system is almost ready for the final testing. Thanks to the engineers of General Electric, we are able to gain three dimensional geometrical data from angiography

At this moment we analyzed two real aneurysm sacks with similar boundary and load conditions as were made in the idealized situations. In Figure 11 the velocities at the moment of the peak systole can be seen. We note that in the second situation – following from the geometry of the aneurysm - the velocity in the sack is smaller than in the first case.

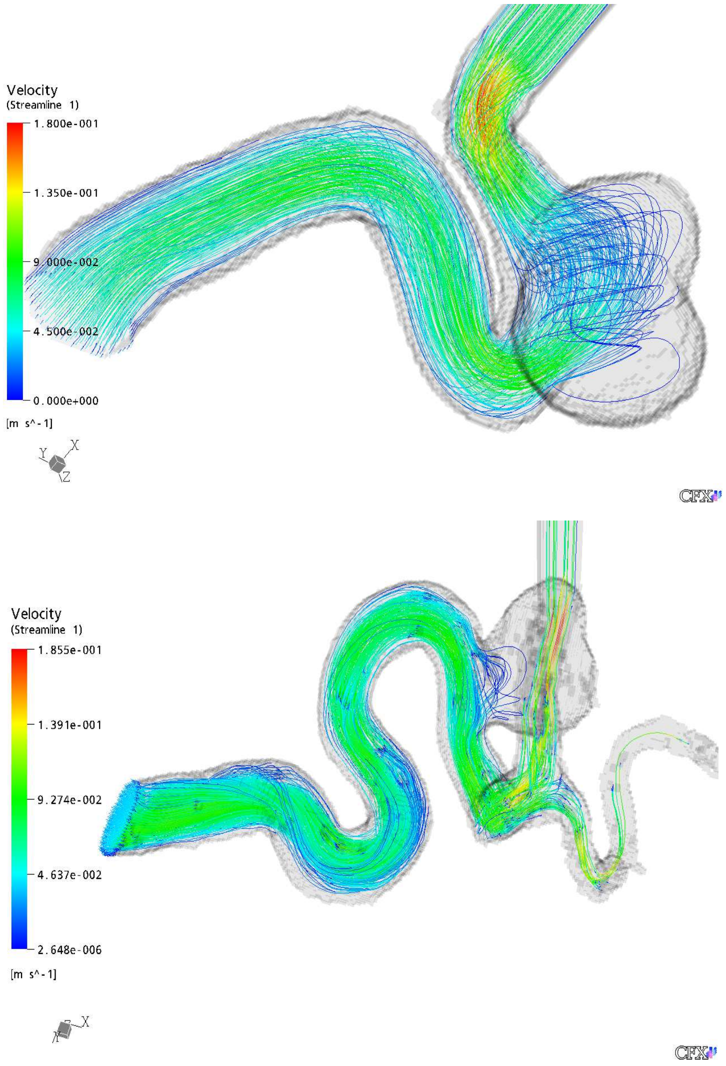

Figure 11. Stream lines in two different aneurysms

The shear stresses could be seen in Figure 12 for these aneurysm sacks. In both situations there are relatively small shear stresses at the internal surface of the balloons.

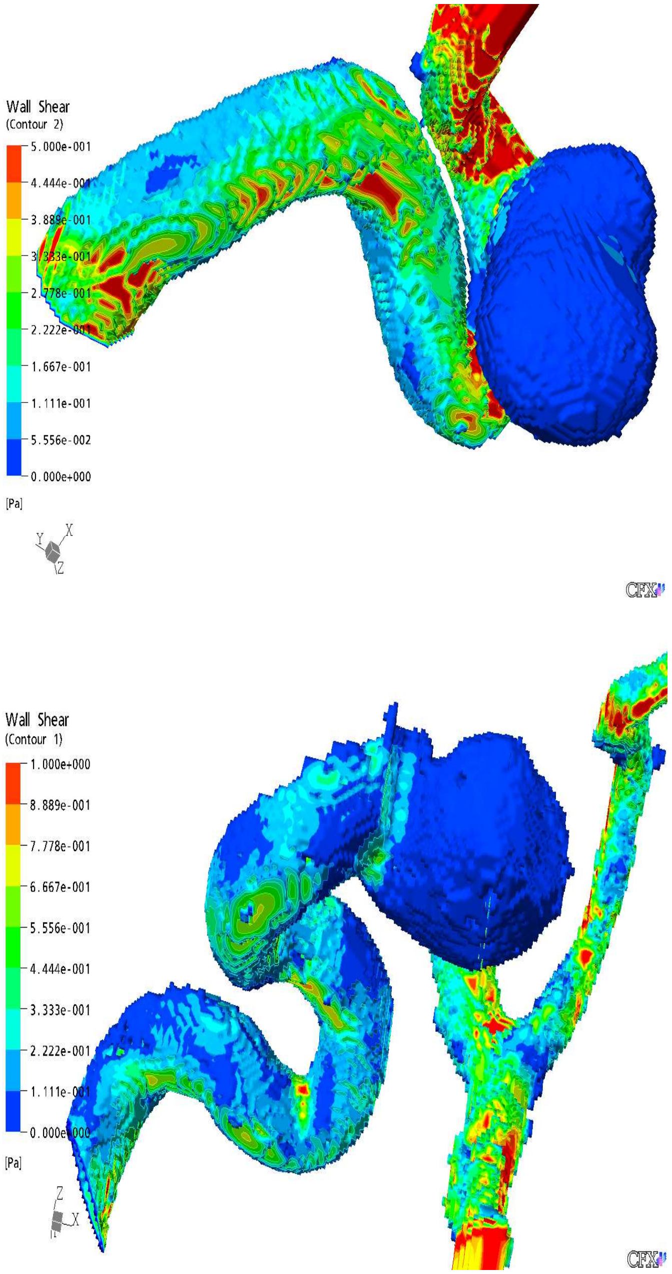

Figure 12. Shear stresses at the internal surfaces of the walls

5. Analysis of the artery wall

The task is to give an approximate computation for the stress changing in the wall caused by the changing of the haemodynamics, surroundings, and wall material. The resource assimilates the study of vascular material changing after evolution of brain aneurysm based on laboratory experiment. The haemodynamical behaviour (contrary to the original state) has definitely changed because of the large local displacements. In this case the bloodstream is interpreted as a function of the wall shape.

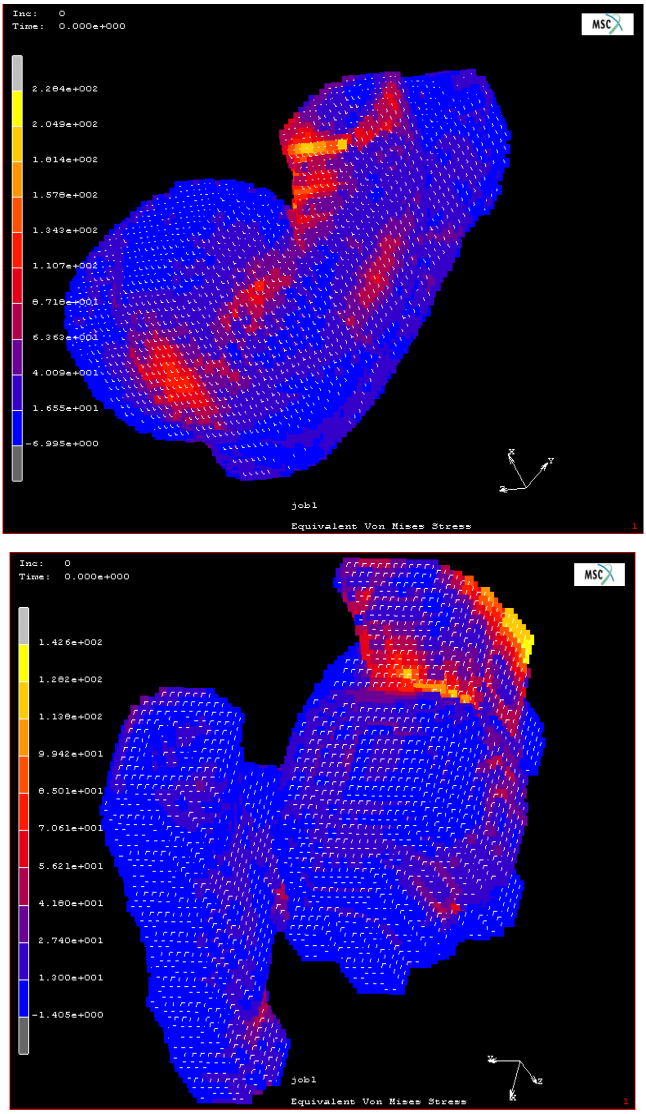

Figure 13. Mises-stresses in the walls of different aneurysms

On the other hand, the shape of the vascular wall is defined by the surroundings and the haemodynamics itself. Therefore all haemodynamical calculations should be done with the help of the current shape of the vascular system.

So far it seems that only one of the two tasks can be solved at a time. This means that the forces expressed by the haemodynamical behavior change the stress distribution inside the wall. Using the stress distribution change and complex material model, the increase in deformation (field of strain) can be calculated. Because this deformation is usually large, so all the calculations have to be done on the changed geometry, not on the original. That is why all the numerical calculations are geometrically nonlinear.

The original aneurysm is taken out from its environment in our approach, and it is analyzed in itself, with the help of numerical methods and connected boundary conditions. This shortcut does not cause large errors in the model. This point is related to the strength analysis so the task is to estimate the stress distribution due to the forces given by the haemodynamical analysis, boundary conditions, and the applied material model. Two different types of geometry were tested during the research: first we used an idealized model to adjust the model parameters and assay the effect of the change of the model; the second type of geometrical data were gained from angiography results.

The well-known finite element method was applied as a numerical approximation for these two different systems. We used MSC Marc and Ansys for both strength calculations. Figure 13 shows the details of the calculated wall-stresses at the maximum systole pressure in the real geometry.

6. **Summary**

In cooperation with the staff of the National Institute of Neurosurgery and Human Sciences we made the first steps in the complex numerical simulations of brain aneurysms. Our connected system can calculate the dynamic flow parameters of blood and from this effect can determine the displacements and stresses in the vessel wall. In the future we plan to continue our work by refining the finite element mesh and then we want to simulate the load bearing capacity of the rupturing balloon of the aneurysm sack.

Acknowledgement. This work was done with the help of an OTKA-grant (leader dr. István Szikora, National Institute of Neurosurgery).

References

1. Thubrikar, M.J.: Wall stress studies of abdominal aortic aneurysm in a clinical model., *Annals of vascular surgery*, **15**, (2001), 355-366.
2. Lermusiaux, P., Leroux, C., etc.: Aortic aneurysm: construction of a life-size model by rapid prototyping. *Annals of vascular surgery*, **15**, (2001), 131-135
3. Steinman, D.A., etc.: Image-based computational simulation of flow dynamics in a giant intracranial aneurysm.*American J. of Neuroradiology*, **24**, (2003), 559-566.

4. Fung, Y. C.: *Biomechanics: Circulation.* Springer, New York, 1997.
5. Liepsch, D.: An introduction to biofluid mechanics – basic models and applications. *J. of Biomechanics*, 35, (2002), 415-435.
6. Egelhoff, C.J., etc.: Model studies of the flow in abdominal aortic aneurysm during resting and exercise conditions. *J. of Biomechanics*, **32**, (1999), 1319-1329.
7. O'Rourke M.F.: Vascular mechanics in the clinic. *J. of Biomechanics*, **36**, (2003), 623-630.
8. Choung, C.J. and Fung, Y.C.: Three-dimensional stress distribution in arteries. *J. Biomech. Engr.*, **105**, (1983), 268-274
9. Vorp, D.A., Rajagopal, K.R., Smolinsky, P.J. and Borovetz, H.S.: Identification of elastic properties of homogeneous orthotropic vascular segments in distension. *J. Biomech.*, 28, (1995), 501-512.
10. Tóth, M., Nádasy, G.l., Nyáry, I., T. Kerényi, T., Orosz, M., Molnárka, G. and Monos, E.: Sterically inhomogeneous viscoelastic behavior of human saccular cerebral aneurysms. *J. Vasc. Res.,* **35**, (1998) 345-355.
11. Fonyó, A.: *Textbook of Medical Physiology.* Medicina, Budapest, 1999. (in Hungarian)
12. Mónos, E.: Hemodynamics: dynamics of the blood circulation. Lecture notes, Budapest, 2001. (in Hungarian)
13. Holzapfel, G.A., Gasser, T.C. and Ogden, R.W.: A new constitutive framework for arterial wall mechanics and a comparative study of material modes. *Journal of Elasticity,* **61**, (2000), 1-48.
14. Finlay, H.M., McCullough, L. and Canham, P.B.: Three-dimensional collagen organization of human brain arteries at different transmural pressures. *J. Vasc. Res.*, **32**, (1995), 301-312.
15. Weizsäcker, H.W. and Pinto, J.G.: Isotropy and anisotropy of the arterial wall. *J. Biomech.*, **21**, (1988), 477-487.
16. Rhodin, J.A.G.: Architecture of vessel vall. In Sparks, H.V. Jr., Bohr, D.F., Somlyo A.D. and Geiger, S.R., editors, Handbook of Physiology, The Cardiovascular System II. 1-31. American Physiologial Society, Bethesda, Maryland, 1980.
17. Silver, F.H., Christiansen, D.L. and Buntin, C.M.: Mechanical Properties of the Aorta: *Critical Rewiews in Biomed. Engr.*, 17, (1989), 323-358.
18. Holzapfel, G.A.: Nonlinear Solid Mechanics. A Continuum Approach for Engineering. John Wiley & Sons, Chichester, 2000.
19. Fung, Y. C.:. *Biomechanics: Mechanical Properties of Living Tissue.* Springer-Verlag, New York, 2. ed., 1993

Journal of Computational and Applied Mechanics, Vol. 7., No. 1., (2006), pp. 59–74

EFFECT OF THERAPEUTIC RIDING ON THE COORDINATION OF MOVEMENTS OF DOWN-SYNDROME CHILDREN

Henriette Steiner
Institute of Behavioural Sciences, Semmelweis University, Budapest, Hungary
`henisoft@axelero.hu`
Tibor Szilágyi
Biomechanics laboratory, Department of Biomechanics
Institute of Kinesiology and Sport Medicine, Semmelweis University, Budapest, Hungary
`szilagyi@mail.hupe.hu`

[Received: September 8, 2004]

Abstract. We examined the effect of therapeutic riding on the development of Down-syndrome children. Examination of walking is appropriate for assessing the coordination of movement and for following the changes. We found therapeutic riding should be considered as a new form of rehabilitation. Pupils of a school for handicapped children participated in therapeutic riding. This raised the question how therapeutic riding affects the development of motion, so we researched it.

We selected riding and non-riding children and conducted walk analyses one month before and after therapeutic riding to follow the changes in their coordination. We chose to analyse walking. We used four video cameras from four different views. We processed the data by the APAS video analyser system. We used the Dempster model. For the construction of the model we conducted anthropometric measurements. This method made it possible to follow the movements of the selected points of the body in three dimensions. Statistical analysis was based on T-probe.

We found significant differences between the test and control groups. In the case of the children who participated in therapeutic riding several parameters were similar to the relevant parameters of healthy children. Their gait asymmetry and hip-motion asymmetry were decreased. We made several movement analyses of the same group and these data were compared.

According to our results, therapeutic riding may be successfully used as an additional therapy for Down-syndrome children and may represent a form of rehabilitation in cases when other means of therapy are not successful.

Keywords: therapeutic riding, Down-syndrome, hip-motion asymmetry, asymmetry, coordination of movements

1. Introduction

1.1. **Some concepts.** Before the description of the measurements, we have to write some words about the biomechanics of gait and Down-syndrome.

1.2. **Hip.** The hip in Down-yndrome is retroverted, with excessive external rotation both in flexion and extension, resulting in out-toe gait. Five percent of children with Down-syndrome develop a dislocatable or dislocated hip. These children are usually delayed in walking; their hips are hypermobile but not dislocatable until at two to four years of age, the affected hip spontaneously becomes dislocated and relocated. Presenting complains are a click in the hip, an increasing limp or ´giving way' and refusal to walk With recurrent dislocation, physical activity diminishes. The dislocations are not painful. If untreated, eventually subluxation or dislocation may become fixed. The recurring dislocated hip is usually treated surgically [1–6].

1.3. **Atlantoaxial instability.** Atlantoaxial instability is an established entity in Down-syndrome It occurs in 10% to 20% of these patients. Atlantoaxial instability in Down-syndrome is caused by ligamentous laxity of the transverse ligament that holds the odontoid process close to the anterior arch of the atlas. This instability results in loose joints, where the cervical vertebrae slip forward and the spinal cord is vulnerable to compression.

The neurologic manifestations of spinal compression are fatigue in walking, gait disturbance, progressive clumsiness, incoordination, spasticity, hyperfiexion, clonus, and toe-extensor reflex. Onset of neck pain, headache and torticollis are indicative of malposition of the odontoid [7,8,9].

1.4. **Motor development and gait.** Children with Down-syndrome show a longer period of stance than independent walkers, comparable to that of the supported walking of infants. There is a decrease in hip extension and early hip extension near the end of swing. This is seen as an attempt to make a flatfoot contact instead of the initial heel contact. There is a decrease in ankle sagittal plane rotation, and exaggerated abduction of the swing limb appears to be necessary for foot clearance. There also appears to be a relationship between sitting patterns and gait patterns of children with Down-syndrome. Clinical observation suggests that children with Down-syndrome usually have excessive external rotation and abduction of the hip, demonstrated by their sitting with widespread legs, and this excessive external rotation and abduction is displayed when they learn to sit. The wide-angled gait is caused by marked hip retroversion, genu valgum of the knee, external tibial torsion, and excessively pronated feet. It has been proven that ambulation performance, including balance and jumping, can be significantly improved in children with Down-syndrome with even minimal physical therapy sessions, such as jumping classes. This type of therapy should be encouraged [10].

1.5. **Considerations in the correction of congenital deformities.** Early detection and treatment of congenital pedal deformities is important in a child with Down-syndrome. Since these children are subject to a multiplicity of orthopedic problems, an aggressive program to maintain proper skeletal alignment can significantly decrease the severity of these problems and allow the individual to function much more efficiently. In a report on the management of foot and knee deformities in the mentally retarded, Lindsey and Drennan asserted that "proper alignment of the immature foot will frequently decrease the external rotation of the limb and result in development of a more appropriate gait pattern." Rather than being aggressively treated, many of the common congenital deformities, such as metatarsus adductus and tibial torsion, are overlooked because of the patients' many other medical and orthopedic problems, and no treatment is rendered [11,12]. The treatment modalities used in the correction of congenital foot and torsional abnormalities in the child with Down-syndrome are the same that would be used in the normal patient. These include serial immobilization casting, corrective shoes and splints, and surgery. Due to the prolonged excessive ligamentous laxity and the relatively slower foot growth, corrective modalities often are required for longer periods of time in the child with Down-syndrome. Immobilization modalities that impede walking, such as plaster casts or restrictive splinting, should be avoided in the older child, since these can further delay the progression of neuromotor development in a child that will already exhibit a significant delay in learning to walk. The use of properly modified corrective shoes should be encouraged when correcting foot pathology in children with Down-syndrome who have progressed beyond the states of sitting independently and crawling. Reduction of Out-Toe Gait and Genu Valgum [13,14].

2. Methodology

2.1. **Work hypothesis.** Our work hypothesis is that if riding changes the coordination of movements in these children it will exert effects on their walking as well. Walking requires coordinated work by many muscles, virtually the whole body. Execution of these complex movements requires not only appropriate development of the muscular and the osseous systems but it requires adequate control of movements (e.g. faultless working of flexor and extensor reflexes) as well. We started our examinations (with methods learned from experience abroad) in Budapest, March 1998. We established two groups of the pupils of the school for handicapped children school: one group consisted of riding Down-syndrome children, the other group consisted of non-riding Down-syndrome children. We conducted measurements on the coordination of movements before and after the therapy. We would like to write about four measurements, which are designated by four numbers: (1) before therapy in March 1998, (2) after therapy in May 1998, before therapy in September 2000 and (4) after therapy in October 2000.

2.2. **Criteria of investigation.** Subjects had to have the presence of Down-syndrome and their age had to be in the range of 10-13 years. We examined 30 children, but four of them left the groups, because of illness (staying in hospital).

Table 1. The two groups examined

Features	**Children participating in therapeutic riding**	**Control group**
Disease	Down-syndrome	Down-syndrome
Age	10-13 years	10-13 years
Number of children	13	13
Therapy	Western style riding (with western saddle and hackamore or pelham)	Exercises: physioball, sitting up, leg raising on wall-bars
Duration	1998-2000	1998-2000

2.3. **Subjects of investigation.** We selected riding and non-riding children and conducted walk analysis before and after therapeutic riding to follow the changes in their coordination. We chose gait analysis. The pupils of the school for handicapped children were examined by the physician of the school and all of them were advised to participate in our investigation. The parents of the 30 children signed an agreement that they would accept the result of the random drawing that formed the riding and the non-riding groups. While the riding group participated in therapeutic riding the other group did their habitual exercises (as before). The physician of the school advised every child to participate in therapeutic riding. Orthopedic doctors radiographed functional cervical radiogram. The parents of the children decided whether their child should participate in therapeutic riding or not. Our examination is a comparative study of the two therapeutic methods.

Before testing, the subject signed an informed consent form approved by the Policy and Review Committee on Human Research of Semmelweis University, the children's guardians and school.

2.4. **Therapeutic methods.** We analyzed two different methods to compare the effectiveness of rehabilitational techniques. The investigated population was divided into two groups. For the control group (group 1) three times a week 1 hour of classical kinesitherapy was conducted. In the test group (group 2) once a week the children trained by special riding for 15 minutes [15].

2.5. **Type of special riding.** As for some aspects western style riding fits best for therapeutic riding. In case of backward children special attention has to be paid to the safety of the riders during therapeutic riding. This requires increased attention and tolerance of the trainer and unconditional obedience of the horse.

2.6. **Gait analysis.** We made video recordings of the walk of the children one month before and after the therapy. The walk was recorded from four views (front, rear, left and right). The video recordings were processed by the APAS (Ariel Performance Analysis System). This system made it possible to present three dimensional kinematics parameters by the analysis of video recordings made in everyday situations.

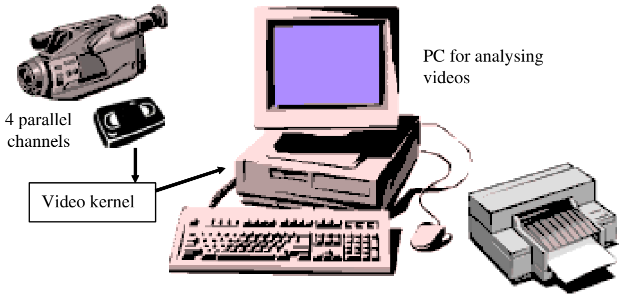

Figure 1. Equipment for the analysis

2.7. **Equipment for analysis.** We used four video cameras (type: Panasonic M10) from four different views. Sampling frequency was 50 frames/second (sampling rate

0.02 second) with shutter speed of 1/250 second. We processed the data by the APAS video analyzer system (VCR is Panasonic AG-7350, Computer is AST Bravo 486/25). Digitalization of landmarks was made manually (relative digitalization error 3-5%). The system generated the 3D database with direct linear transformation (DLT). We used the software version APAS rev. 6.73. We made smoothing (noise filtering) through quintal spline algorithm (built in the APAS [16]).

2.8. **The validation system.** After setting the cameras calibration was performed. For our investigations we used an eight-point calibration parallelepiped like cubic structure. After the measurement situation was set and recorded the parallelepiped was removed so as not to bother the children in moving. The coordinates of the eight control points are in Figure 2. The coordinates of the first point are not zero in all three dimensions because we shifted the coordinates in relation to a virtual origo to enable easier visualization of the data (none of the coordinates fall below zero). The eight points determine the three dimensions of space. The two bold black marks indicate a 200 cm long section in which the two gait cycles were analyzed.

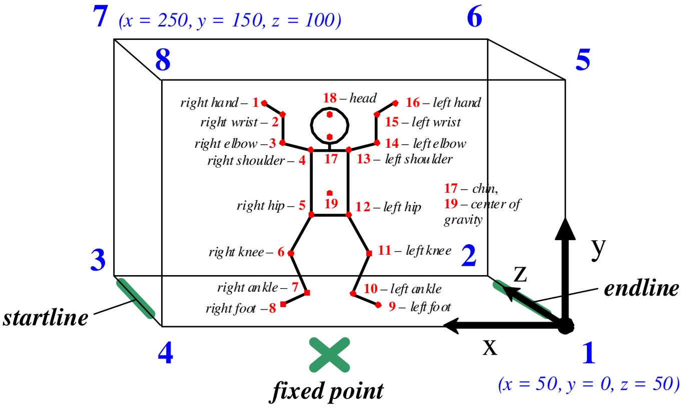

Figure 2. Control points and the body model

2.9. **The body model.** We used a body model to follow the movements of several points of the body. On processing the data we applied a modified form of Dempster's body model that consists of eighteen points and several lines that connect them. The nineteenth point is the center of mass of the body. Dempster's model was modified in the following way. We defined the landmarks, segments, and interconnections of the model. For the construction of the model we conducted anthropometric measurements. The global and local anthropometric data of every child were taken into consideration (segment lengths, relative body masses, radiuses of gyration). Height and body weight were measured and the partial centres of mass of the body segments were calculated. The final model was constructed after using these data. This method made it possible to follow the movements of the selected points of the body in three dimensions [17,18].

2.10. **Statistical analysis.** The basis of statistical analysis was T-probe. We compared the differences between mean values of parameters of selected groups (length of gait cycle). The equality of standard deviation in the statistical populations was checked by F-probe.

3. Results

Data on the coordination of movements of ´riding' and ´non-riding' children were compared. The data of only 13-13 children were processed because 2 children in each group could not participate in the second measurement series. In the next Section the coordination of movements of 1 child from both groups will be analyzed.

The headway (x-axis) motion of both legs of the ´riding' child was plotted against time (Figures 3-4). The first figure shows that the two legs were exposed to unequal loading. The child made shorter steps with the right leg and the foot spent longer time on the ground (the straight sections of the curves are longer). The enclosed areas of the two curves are not equal because of unequal loading. The vertical lines indicate the sections of the curve when both feet are on the ground at the same time (double supporting). Asymmetry of motion can be observed. The right leg of the child was weaker than the left. The second figure indicates that the influence of riding was that asymmetry of the motion of the two legs decreased (the areas enclosed by the curves are nearly equal) and the speed of walking increased (the duration of double supporting decreased).

Figure A

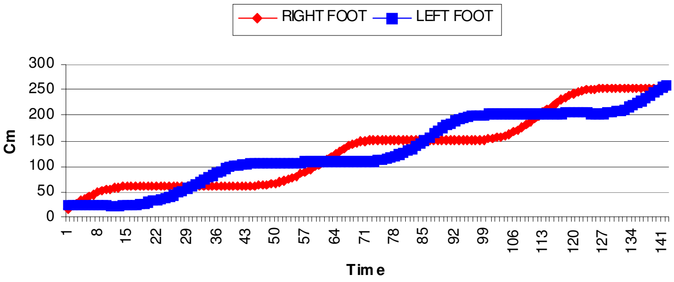

Figure B

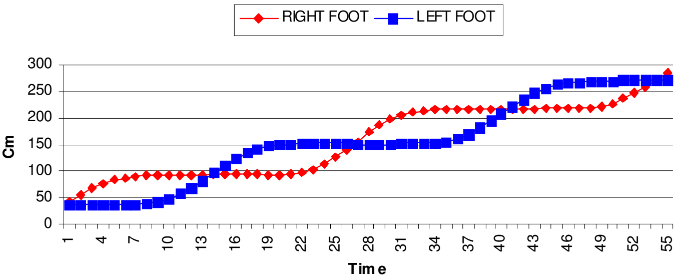

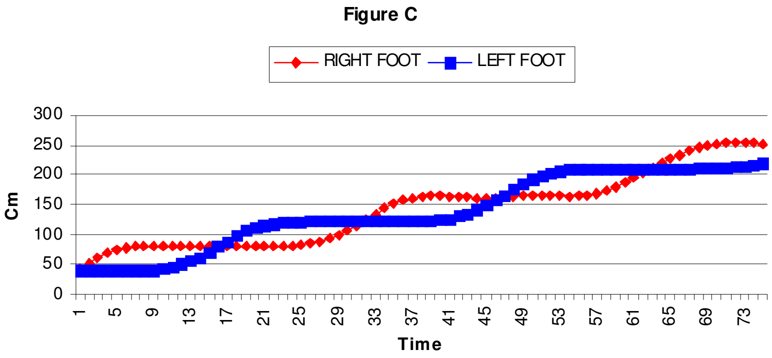

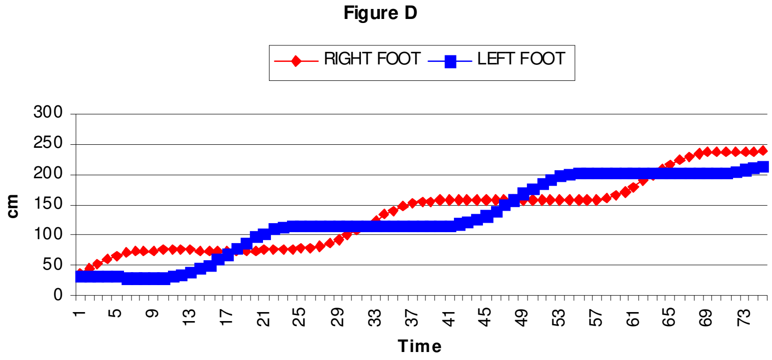

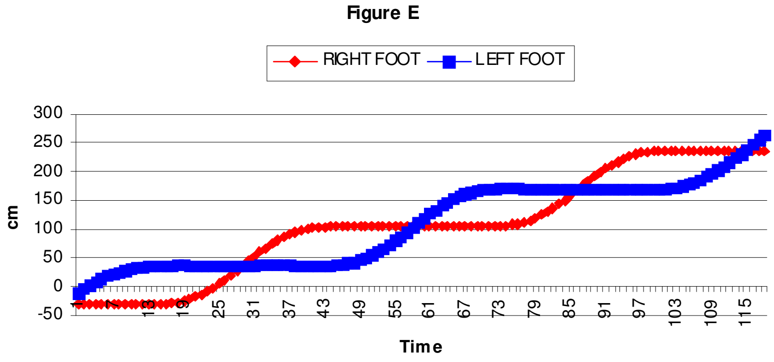

Figure 3. Motion of both legs. Figure A: riding child before therapeutic riding, Figure B: riding child after therapeutic riding, Figure C: non-riding child before therapy, Figure D: non-riding child after therapy, Figure E: Normal child.

Figure A

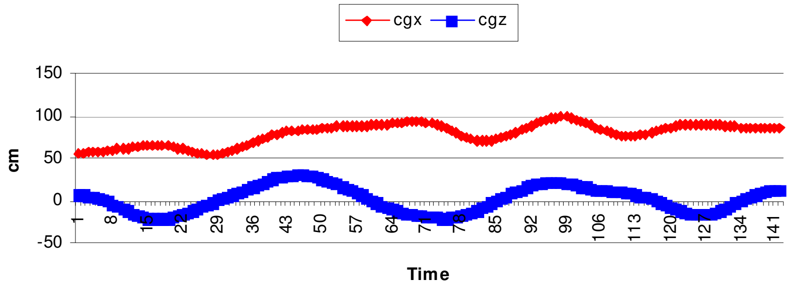

Figure B

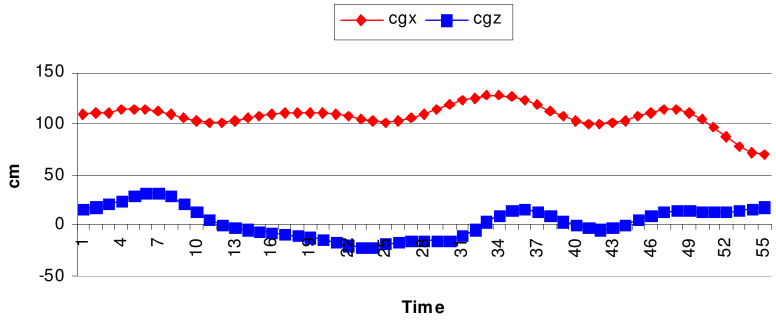

Figure C

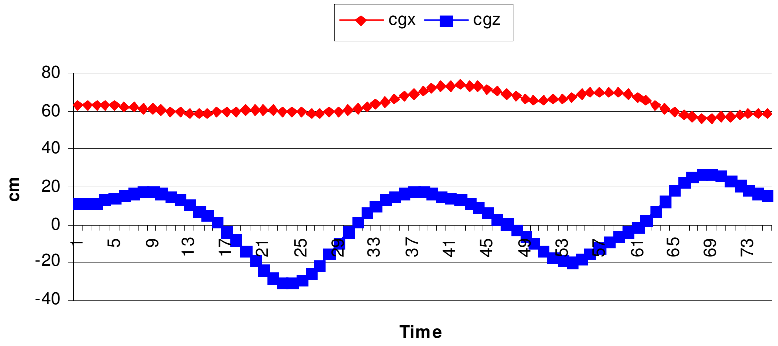

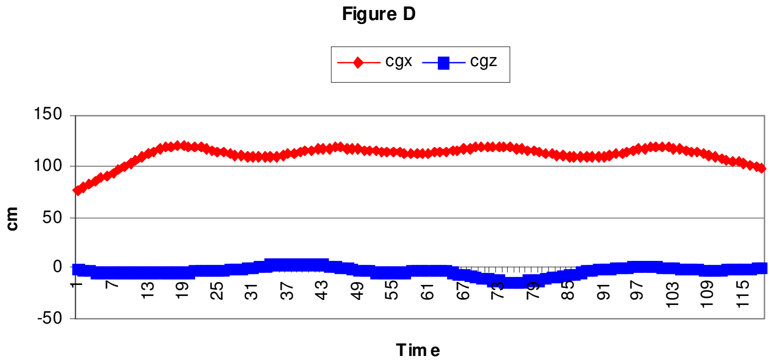

Figure 4. Motion of the center of gravity. Figure A: riding child before therapeutic riding figure B: riding child after therapeutic riding figure C: of non- riding child before therapy Figure D: non- riding child after therapy

The headway (x-axis) motion of both legs of the ´non-riding' child was similarly plotted against time (Figures 5-6). The areas enclosed by the curves are not equal due to asymmetric loading. The vertical lines indicate double supporting. Asymmetry of motion is clearly visible. No betterment was observed in the walking technique of these children after the treatment. During the second series of measurements higher speed was observed, but the duration of double supporting showed significant increase. There is a seeming contradiction between the higher speed and the longer duration of double supporting (that is slow walking) but this can be construed by the worsening of balance and that this balance is corrected by conscious motor control (longer double supporting). The swing phase of the step became quicker and the resultant of these two factors is higher speed.

In the next step we analyzed the motion of the hip during walking (Figure 5). The three dimensional motion of the hip before the treatment can be characterized in the following way: the motion is performed more or less in opposite phase but the left side of the hip moves with much greater amplitude during walking. Asymmetry is clearly visible. The three phases of the healthy motion of the hip (supporting, rolling and pushing off) cannot be found because the hip is stiff.

In Figure 5 the motion of the two hips is compared after therapeutic riding. The two sides moved more symmetrically than before. The shape of the curve changed because one component of the healthy step cycle appeared in the motion of the hips. The Figure shows the motion of the hip of a healthy child of similar age. The three phases of motion can be followed and identified (0.5–1.0 sec). Its appearance is like the inverse of the first figure because a Down-syndrome child does not step on the ground quickly like healthy people do. This difference is compensated by a quick pushing off.

The analysis of the motion of the center of gravity shows the balance of the gait. In two dimension measurements (x and z) the center of gravity often moves with a bigger amplitude.

Figure A

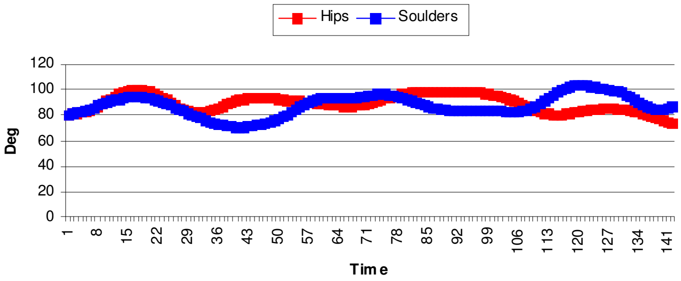

Figure B

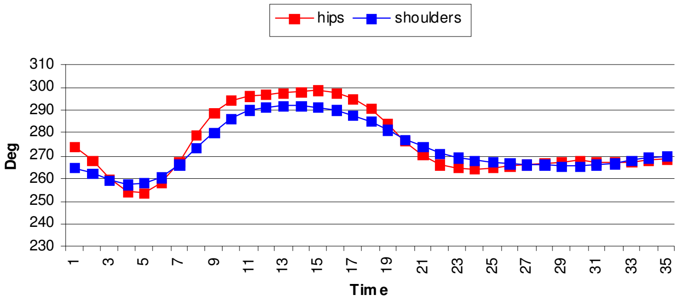

Figure C

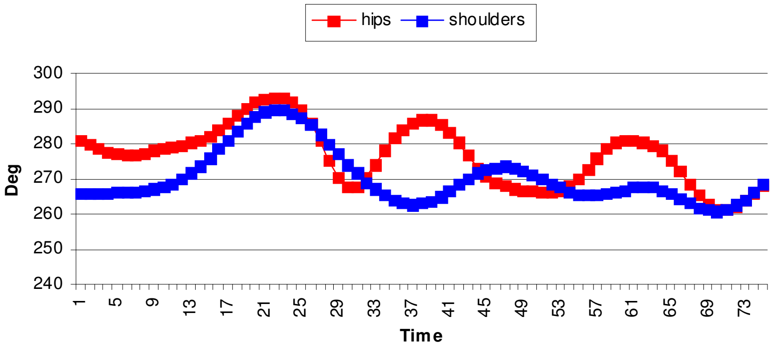

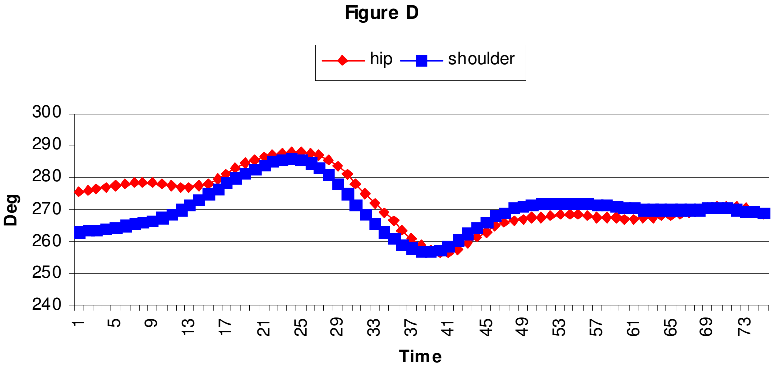

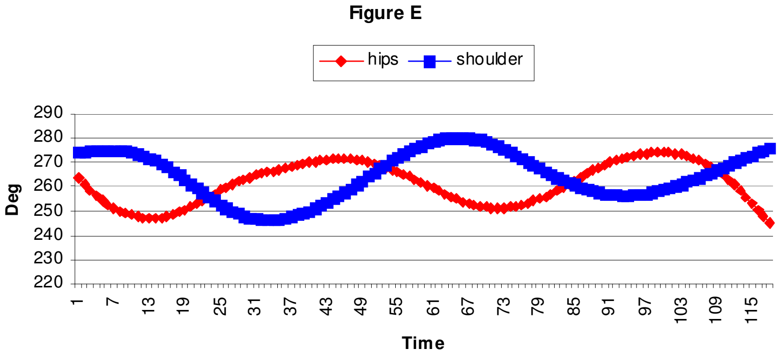

Figure 5. Motion of the hip and shoulder. Figure A: riding child before therapeutic riding Figure B: riding child after therapeutic riding Figure C: non-riding child before therapy Figure D: non-riding child after therapy Figure E: Normal child

Analysis of the motion of the shoulder and the hip axes gives an insight into the motion of the spine and the motion of the hip and the shoulder of the same side (Figure 5). Before treatment the hips moved stiffly while the shoulders made significant excursions during the step cycle. The stiffness of the hips is compensated by the movements of the shoulders (0.5–1.0 sec). After therapeutic riding we observed that the hips and the shoulders moved in the same phase (the hips and shoulders of the same side moved together) because the turning of the trunk that helped walking. The amplitude of the excursion of the two hips increased and were nearly equal.

The hips and shoulders of a healthy child move in the opposite phase. With therapeutic riding a transitional condition was achieved that may be further developed.

Figure A

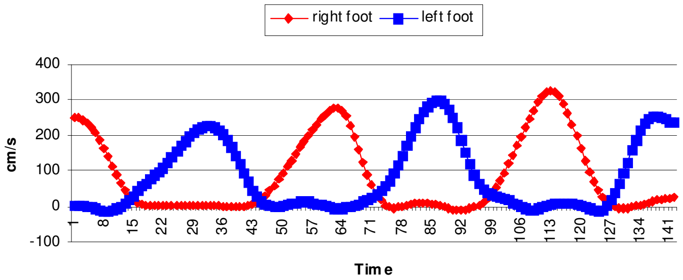

Figure B

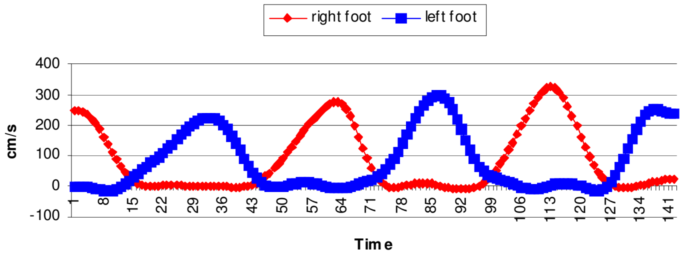

Figure C

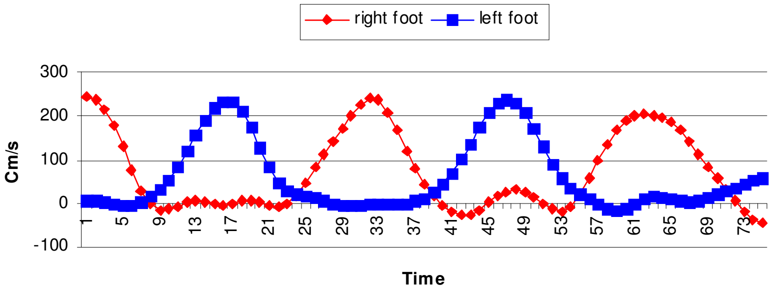

Figure D

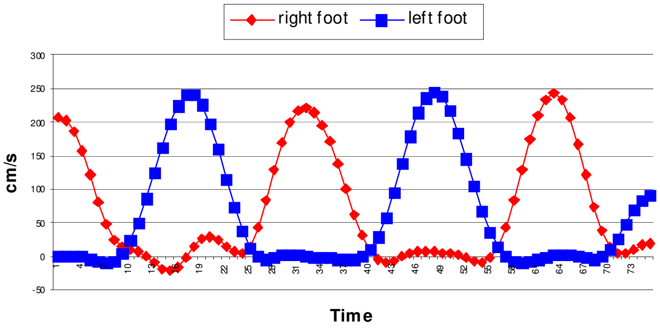

Figure E

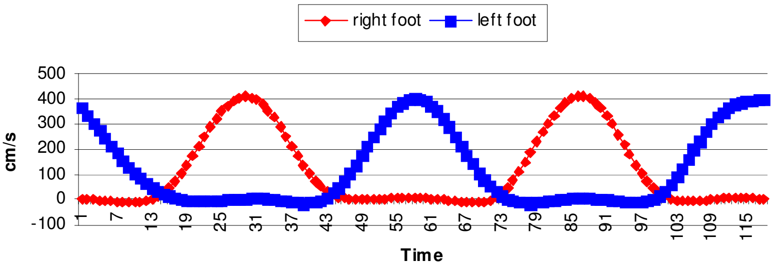

Figure 6. Velocity of feet. Figure A: riding child before therapeutic riding Figure B: riding child after therapeutic riding Figure C: non-riding child before therapy Figure D: non-riding child after therapy Figure E: Normal child

Analysis of the Velocity of feet was given new information from the asymmetry. The right side is weaker, but after the therapeutic riding the asymmetry is nearer the normal gait (in normal gait we measured a little asymmetry, but statistically it is not significant).

When we compared the ´riding' and the ´non-riding' groups several considerations had to be made. For the analysis of the coordination of movements we had to choose a parameter that adequately indicates the occurring changes: improvement or relapse had to be followed by consistent changes of the parameter. The parameter had to give information on the extent of hip - motion asymmetry, asymmetry and balance, altogether: the coordination of movements. The length of the steps is considered to be a parameter of this kind (increase in the length of the steps indicates higher speed, better balance and better coordination of movements). As the motion of a Down-syndrome child is asymmetric, we measured the length of steps between two supporting phases of one leg by using the selected points of the body model (in cm). The measurements were performed one month before and one month after the therapy

(March 1998 and May 1988 for 1 and 2, September 2000 and October 2000 for 3 and 4). Means and coefficients of variance were calculated. With dual T-probe we checked whether significant changes can be found in the motion of the two sides.

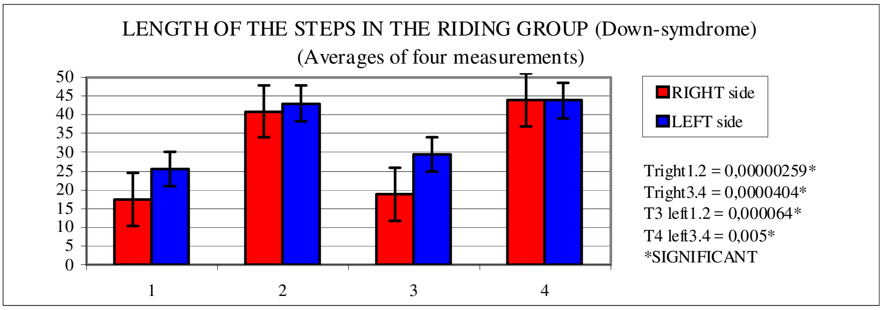

Figure 7. Length of steps in the riding group

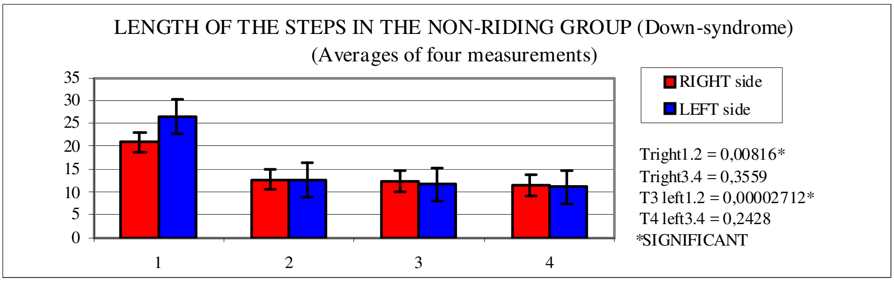

Figure 8. Length of steps in the non-riding group

Significant increase was detected in the length of the steps of both legs, which indicates better coordination of movements and decrease of hip-motion asymmetry. We measured the same groups for two years and looked for the asymmetry of two sides. There are no differences between the sides, as in healthy children (Figure 7-8).

4. **Conclusions**

Thus, as we have shown previously, coordination of movements is controlled by several factors. For the development of motion the extent of asymmetry and muscular atrophy/hypotony have to be diminished and appropriate working of muscles and coordination of movements have to be developed. For this purpose special exercises are used to cure muscular hypotony, to help the establishment of normal muscular tension and help to strengthen the ´less developed side' of the children. Our parameters help us to control the changes of motion. As you can see in the results, therapeutic riding makes better balance, smaller asymmetry, and hip-motion asymmetry.

Last but not least it is important to examine the costs of therapeutic riding and how it compares with the costs of other rehabilitation treatments.

Table 2. Costs of therapies (therapeutic riding vs. other rehabilitation) OEP

Costs of therapeutic riding		**Costs of rehabilitation**	
Therapeutic riding	**Costs (USD)**	**Rehabilitation**	**Cost (USD)OEP**
One child/hour	100	Physiotherapeutist with one child one day in hospital rehabilitation	23
Costs per year	52 x 100 = 5200	Costs per year	8561

According to our results therapeutic riding may be successfully used as an additional therapy for Down-syndrome children and it may present a form of rehabilitation in cases when other means of therapy are not applicable (e.g. because of psychic and physical conditions).

References

1. Bennet, G. C., Rang, M., Roye, D. P. and Aprin, H.: Dislocation of the hip in trisomy 21. *Bone Joint Surg. Br.*, **64**(3) (1982), 289-294.
2. Aprin, H., Zink, W. P. and Hall, J. E.: Management of dislocation of the hip in Down-syndrome. *J. Pediatr. Orthop.*, **5**, (1985), 428–431.
3. Parker, A. W. and Bronks, R.: Gait of children with Down-syndrome. *Arch. Phys. Med. Rehabil.*, **61**, (1980), 343–351.
4. Parker, A. W., Bronks, R. and Snyder, C. W.: Walking patterns in Down's syndrome. J. Ment. Defic. Res., **30**, (1986), 317–330.
5. Aprin, H., Zink, W. P. and Hall, J. E.: Management of dislocation of the hip in Down-syndrome. *J. Pediatr. Orthop.* **5**, (1985), 428–431.
6. Can, J.: Mental and motor development in young Mongol children. *J. Ment. Defic. Res.*, **14**, (1970), 205–220.
7. Hreidarsson, S., Magran, G. and Singer, H.: Symptomatic atlantoaxial dislocation in Down-syndrome. *Pediatrics*, 69: 568,(1982), 568–571.
8. Committee on Sports Medicine: Atlantoaxial instability in Down-syndrome. *Pediatrics*, **74**, (1984), 152–154.
9. Pueschel, S. M. and Scola, F. H.: Atlantoaxial instability in individuals with Down-syndrome: epidemiologic radiographic, and clinical studies. *Pediatrics*, **80**, (1987), 555–560.
10. Caselli, M. A., Cohen-Sobel, E., Thompson, J., Adler, J. and Gonzalez, L.: Biomechanical management of children and adolescents with Down-syndrome. *J. Am. Podiatr. Med. Assoc.*, **81**,(1991), 119–127.
11. Dugdale, T. W. and Renshaw, T. S.: Instability of the patellofemoral joint in Down-syndrome. *J. Bone Joint Surg.*, **68A**, (1986), 405–413.
12. Wang, W. Y., Ju, Y. H.: Promoting balance and jumping skills in children with Down-syndrome. Percept Mot. Skills, **94**, (2002), 443–448.
13. Diamond, L. S., Lynne, D. Sigman, B.: Orthopedic disorders in patients with Down's syndrome. *Orthop. Clin. North Am.*, **12**, (1981), 57–71.

14. Diamond, L. S.: Management of inanderited disorders of the skeleton. Instr. Course Lect., 25, (1976), 107-134.
15. Turner, M. L.: Rebecca's ride. *Am. J. Nurs.*, **94**(1), (1994), 96.
16. APAS System Description and User's Guide Ariel Life System Incorporated, San Diego, CA, USA, 1993, pp. 1, 14-34, 53.
17. Barton, J.: *Bevezetés a biomechanikába (An Introduction to Biomechanics)*. Egészségügyi Főiskolák tankönyve, AESCULART, Budapest, Hungary, 1996, pp. 90-109. (in Hungarian)
18. Szilágyi T., Bartos G., Tóth Sz., Szántó M.: A mozgásanalízis felhasználásának lehetőségei a klinikai gyakorlatban (Utilization of Motion Analysis in Clinical Practice). Mozgásterápia (Motion Therapy), IV.(4), (1996), 3-10. (in Hungarian)

Journal of Computational and Applied Mechanics, Vol. 7., No. 1., (2006), pp. 75–83

BALANCING WITH DISTRIBUTED REFLEX DELAY

Gábor Stépán
Department of Applied Mechanics, Budapest University of Technology and Economics
H-1111 Budapest, Hungary
`stepan@mm.bme.hu`

Dénes Takács
MSc student, Mechanical Engineering, Budapest University of Technology and Economics
H-1111 Budapest, Hungary
`denestakacs@yahoo.co.uk`

[Received: September 12, 2004]

Abstract. From a dynamics view-point, human self-balancing is a very complex process. The vertical position of the body is unstable in the gravitational space, and the human control tries to stabilize it when we stand still. The dynamic study of the control of the inverted pendulum provides important conclusions for balancing. The role of the delay of human reflexes is emphasized in this report. Different kinds of time delays are investigated. The critical delays of reflexes are determined with discrete delays, and also with delays distributed over the past. The numerical values fit well the experimentally determined ones.

Mathematical Subject Classification: 34D20, 37G05
Keywords: time delay, balancing, linear stability, reflex, labyrinth

1. **Introduction**

The dynamics of human balancing is still not understood perfectly. Recently, neurologists [1] have started using balancing experiments to test the behavior of the human brain, to identify and quantify certain disorders. Such an experiment could be, for example, how long a patient can balance a half a meter long stick on his/her fingertip. From the results of these experiments, one can draw conclusions on the ability to concentrate and on the speed of reflexes.

Clearly, there is a unique correlation between the speed of reflexes and the performance of balancing. Self-balancing of a human body is much more complex than balancing a stick on a fingertip, but the role of time delay in the control is the same, and the arising vibration frequencies are also in the same range. The number of fall-overs of elderly people in retirement homes is proven to be correlated with the increased reflex time and increased threshold of perception [2]. It is also well-known, that the consumption of alcohol increases the reflex delay and jeopardizes not only self-balancing, but also any other human control aiming at stabilization, like driving a car. The loss of stability leads to oscillations about the desired but unstable equilibrium. The vibration frequencies are also measured and known not only on patients but also in sportsmen when balancing is important like in target-shooting [3].

In this report, a mechanical model of the inverted pendulum is given and analyzed in the presence of delayed PD control that imitates a spring-damper support. Simple formulae are derived for the critical time delays where balancing is still possible. The results are compared for different time delay models: discrete delays and delays distributed over the past with certain realistic weight functions imitating probability distributions. In unstable cases, the range of vibration frequencies is also determined. The results are compared with the qualitative behavior of the human balancing organ, the labyrinth.

Finally, a qualitative explanation is given for the chaotic nature of successful balancing. Precise measurements show that there are small-amplitude irregular oscillations even in cases when balancing is considered to be successful. These small oscillations can be modeled as chaotic ones. The dynamic models presenting chaos may give a new insight into the classical problem of the energy consumption of balancing, and also into the stochastic nature of fall-overs.

2. **Delayed dynamic model of balancing**

Figure 1 shows the simplest possible mechanical model of balancing a stick. The model has 2 degrees of freedom (DoF), the corresponding general coordinates are the horizontal displacement x of the lowest point of the stick, and the angle φ between the stick and the vertical direction. The horizontal force Q controls the beam of mass m and length l.

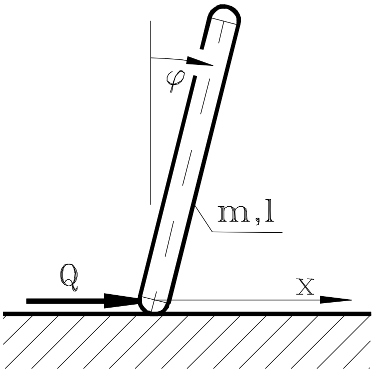

Figure 1. Mechanical model of balancing a beam

The derivation of the system of nonlinear differential equations is given in [4]. The variational system is obtained by linearisation at the upper vertical position $\varphi = 0$.

Its matrix differential equation assumes the form

$$\begin{pmatrix} m & \frac{1}{2}ml \\ \frac{1}{2}ml & \frac{1}{3}ml^2 \end{pmatrix}\begin{pmatrix} \ddot{x} \\ \ddot{\varphi} \end{pmatrix}+\begin{pmatrix} 0 & 0 \\ 0 & -\frac{1}{2}mgl \end{pmatrix}\begin{pmatrix} x \\ \varphi \end{pmatrix}=\begin{pmatrix} Q \\ 0 \end{pmatrix} \tag{2.1}$$

Dot stands for differentiation with respect to time. The control force is considered in the form of a simple PD controller

$$Q(t) = P\int_{-\infty}^{0} w_n(\vartheta)\varphi(t+\vartheta)\mathrm{d}\vartheta + D\int_{-\infty}^{0} w_n(\vartheta)\dot{\varphi}(t+\vartheta)\mathrm{d}\vartheta \tag{2.2}$$

where the weight function

$$w_n(\vartheta) = (-1)^n\frac{n^{n+1}}{\tau^{n+1}n!}\vartheta^n \mathrm{e}^{n\vartheta/\tau}, \quad \vartheta \in (-\infty, 0] \tag{2.3}$$

describes the weights of the delayed values of the angle and angular velocity of the beam in the control. Its integral between $-\infty$ and 0 is 1, and its maximum is at $-\tau$ for the parameters $n > 0$ (see Figure 2).

The delay of the operator's reflexes is characterized by the value τ, while the deviation of the reflex delay is characterized by the integer n: the larger it is, the smaller the deviation is. In some sense, the weight function characterizes the probability distribution of the somewhat stochastically varying reflex delay around τ. As n tends to infinity, the weight function converges to the Dirac delta function (which tends to infinity at $-\tau$ and is zero elsewhere):

$$\lim_{n\to\infty} w_n(\vartheta) = \delta(\vartheta+\tau) \tag{2.4}$$

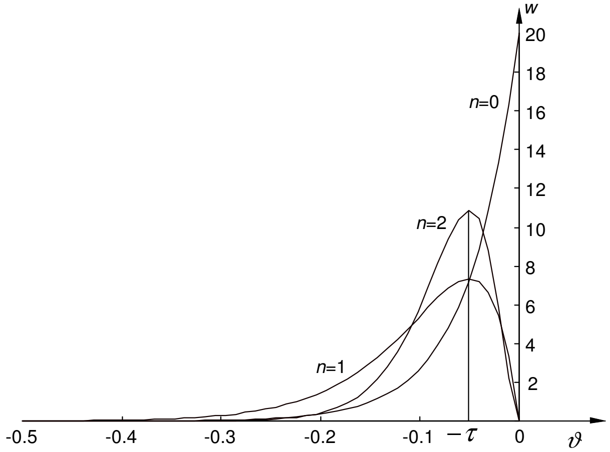

Figure 2. Weight function with respect to the past for $\tau = 0.05$ [s]

All this means that the horizontal control force Q applied by the operator's hand at the lowest point of the stick must be proportional to the sum of the delayed values of the perceived angle and angular velocity of the beam. If this force is substituted into the linear system (2.1) of differential equations, the coordinate x can be eliminated and a scalar delay differential equation (DDE) is obtained for the angle in the form:

$$\ddot{\varphi}(t)-\frac{6g}{l}\varphi(t)+\frac{6}{ml}D\int_{-\infty}^{0}w_n(\vartheta)\dot{\varphi}(t+\vartheta)\mathrm{d}\vartheta+\frac{6}{ml}P\int_{-\infty}^{0}w_n(\vartheta)\varphi(t+\vartheta)\mathrm{d}\vartheta=0\ . \quad (2.5)$$

When the weight function is the Dirac delta function ($n \to \infty$), the DDE (2.5) simplifies to a discrete delay equation:

$$\ddot{\varphi}(t)-\frac{6g}{l}\varphi(t)+\frac{6}{ml}D\dot{\varphi}(t-\tau)+\frac{6}{ml}P\varphi(t-\tau)=0. \quad (2.6)$$

The DDE (2.5) and consequently, its special case (2.6), are satisfied by the trivial solution, which corresponds to the upper equilibrium position of the beam. However, its stability analysis is usually not trivial since the DDE is not an ordinary differential equation, its state space and spectrum are usually infinite dimensional.

3. **Stability analysis**

Several special cases are studied to analyze the stability of the controlled inverted pendulum. First, check the case when there is no time delay in the system:

$$\ddot{\varphi}(t)+\frac{6}{ml}D\dot{\varphi}(t)+\frac{6}{ml}(P-mg)\varphi(t)=0. \quad (3.1)$$

The well-known Routh-Hurwitz criterion [5] proves that in this case, asymptotic stability is equivalent to the positiveness of all the coefficients, that is,

$$D>0, \quad P>mg \quad (3.2)$$

guarantees that both characteristic roots $\lambda_{1,2}$ of the characteristic equation

$$\lambda^2+\frac{6}{ml}D\lambda+\frac{6}{ml}(P-mg)=0 \quad (3.3)$$

have negative real parts. This means that balancing should always be successful for any large gains P and D without time delay in the system.

If the characteristic time delay τ is positive in (2.5) with weights (2.3), the DDE is infinite dimensional and it has infinitely many characteristic roots satisfying the transcendental characteristic equation

$$\lambda^2-\frac{6g}{l}+\frac{6}{ml}D\iiint\limits_{-\infty}^{0}w_n(\vartheta)\lambda e^{\lambda\vartheta}\mathrm{d}\vartheta+\frac{6}{ml}P\iiint\limits_{-\infty}^{0}w_n(\vartheta)e^{\lambda\vartheta}\mathrm{d}\vartheta=0\ , \quad (3.4)$$

which is obtained by substituting the exponential trial solution $x(t)=Ae^{\lambda t}$ into the DDE (2.5). When the reflex delay has no deviation, that is the weight function is the Dirac delta, the characteristic equation assumes the simple form

$$\lambda^2-\frac{6g}{l}+\frac{6}{ml}D\lambda\mathrm{e}^{-\lambda\tau}+\frac{6}{ml}P\mathrm{e}^{-\lambda\tau}=0\ . \quad (3.5)$$

In order to have asymptotic stability for a set of control parameters P, D and τ, all the infinitely many characteristic roots must be located in the left half of the complex plane. The lengthy but exact stability analysis can be found in [6]. In order to simplify the stability analysis to a finite dimensional one, suppose that the time delay is a small parameter, and use the power series expansion of the exponential expressions in the characteristic function (3.5) till their 2^{nd} degree terms with respect to τ :

$$\mathrm{e}^{-\lambda\tau} \approx 1 - \lambda\tau + \frac{1}{2}\lambda^2\tau^2 \qquad \Rightarrow \tag{3.6}$$

$$\frac{1}{ml}\left[\underbrace{3D\tau^2}_{a_3}a_3\lambda^3 + \underbrace{\left(ml + 3P\tau^2 - 6D\tau\right)}_{a_2}\lambda^2 + \underbrace{6\,(D - P\tau)}_{a_1}a_1\lambda + \underbrace{6\,(P - mg)}_{a_0}\right] = 0\ .$$

Although this approximation is not convergent [6], it gives a quite reliable quantitative result at this 2^{nd} order approximation. The Routh-Hurwitz stability conditions imply that

$$a_k > 0, k = 0, ..., 3 \ \text{ and } \ H_2 = a_1a_2 - a_0a_3 > 0 \ \Rightarrow$$

$$P > mg, \ \ D > P\tau, \ \ D < \frac{ml}{6\tau} + \frac{\tau}{2}P \quad \text{and}$$

$$\begin{pmatrix} P & D \end{pmatrix}\begin{pmatrix} -\tau^2 & \tau \\ \tau & -2 \end{pmatrix}\begin{pmatrix} P \\ D \end{pmatrix} + ml\begin{pmatrix} \frac{1}{3} & \frac{1}{3\tau} + \frac{g}{l}\tau \end{pmatrix}\begin{pmatrix} P \\ D \end{pmatrix} > 0 \tag{3.7}$$

The corresponding stability domain in the plane of the gain parameters is presented in Figure 3 for a fixed delay parameter. This domain is essentially separated from the axes, it is bordered by the vertical line $a_0 = 0$ and by the ellipse $H_2 = 0$. This means that there is no way to stabilize the inverted pendulum without using both signals, namely the angle and the angular velocity of the beam.

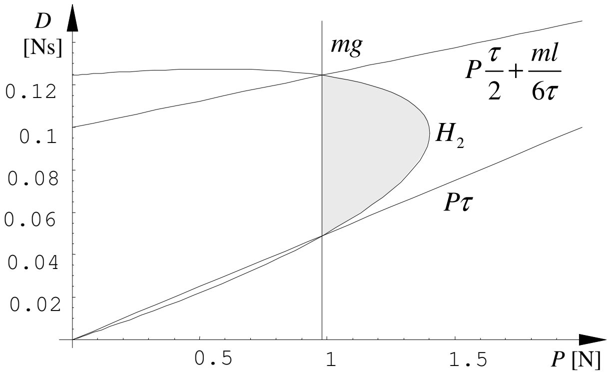

Figure 2. Stability domain (shaded) without reflex deviation for $m = 0.1$ [kg], $l = 0.3$ [m], $\tau = 0.05$ [s] with $n \to \infty$

If the deviation of the reflex delay is also modeled by the use of distributed time delays over the past, the weight function (2.3) can be applied in the equation of motion (2.5). The advantage of these polynomial-exponential weight functions is that the otherwise infinite dimensional system becomes finite dimensional. Consider the $n = 2$ case, that is,

$$w_2(\vartheta) = \frac{4}{\tau^3}\vartheta^2 e^{2\vartheta/\tau}, \;\; \vartheta \in (-\infty, 0] \tag{3.8}$$

In this case, the integrals can be calculated in closed form in the characteristic function (3.4). The multiplication of the characteristic function by λ^3 results the polynomial

$$\begin{aligned}\lambda^5 + \frac{6}{\tau}\lambda^4 + \frac{6g}{l\tau^2}\left(2\frac{l}{g} - \tau^2\right)\lambda^3 + \frac{12g}{l\tau^3}\left(\frac{2l}{3g} - \tau^2\right)\lambda^2 + \\ \frac{48}{ml\tau^3}\left(D - \frac{3}{2}mg\tau\right)\lambda + \frac{48}{ml\tau^3}(P - mg) = \sum_{k=0}^{5} a_k\lambda^k = 0\end{aligned} \tag{3.9}$$

The Routh-Hurwitz criterion leads to the necessary and sufficient exponential stability conditions

$$\begin{aligned}
a_k > 0, k = 0,1,2 \;\; &\Rightarrow \;\; P > mg, \; D > \frac{3}{2}mg\tau, \; \tau < \sqrt{\frac{2}{3}\frac{l}{g}} \\
H_2 > 0 \;\; &\Rightarrow \;\; D < \frac{7}{9}mg\tau + \frac{8ml}{27\tau} + \frac{mg^2\tau^3}{6l} + \frac{\tau}{6}P \\
H_3 > 0 \;\; &\Rightarrow \begin{pmatrix} P & D \end{pmatrix}\begin{pmatrix} -3l\tau^3 & 18l\tau^2 \\ 18l\tau^2 & -108l\tau \end{pmatrix}\begin{pmatrix} P \\ D \end{pmatrix} + \\
m\begin{pmatrix} -48l^2\tau - 6gl\tau^3 - 9g^2\tau^5 & 18g^2\tau^4 + 32l^2 + 228gl\tau^2 \end{pmatrix}&\begin{pmatrix} P \\ D \end{pmatrix} - \\
&18m^2g^2\tau^3(8l + g\tau^2) > 0,
\end{aligned} \tag{3.10}$$

while $a_{3,4,5} > 0$ and $H_{1,4} > 0$ are already satisfied. In this case, the stability chart in Figure 4 is bordered by the vertical line $a_0 = 0$, again, and by the parabola $H_3 = 0$.

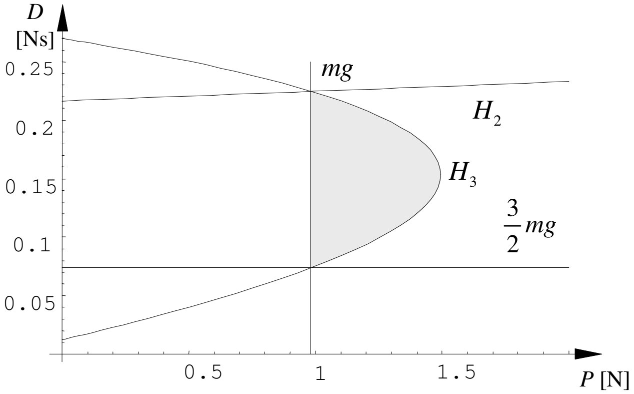

Figure 3. Stability domain (shaded) with reflex deviation for $m = 0.1$ [kg], $l = 0.3$ [m], $\tau = 0.05$ [s] with $n = 2$

The structure of the stability chart is the same as in the case of the 2^{nd} degree approximation of the discrete delay case in Figure 3 without deviation in the reflex delay.

Note that apart from the similar structure of the stability chart in the two cases, a condition appears for the time delay with $a_2>0$ in the latter case. This condition is not represented in Figure 4.

4. **Vibration frequencies**

In both stability charts, saddle-node bifurcation occurs when the proportional control gain P decreases below the weight mg of the beam, and the upper vertical position becomes unstable. When the proportional gain P increases and the corresponding parameter point crosses the $H_2=0$ or the $H_3=0$ stability limit, Hopf bifurcation occurs. This means, that self-excited vibrations arise around the upper vertical position with frequency

$$f=\frac{\omega}{2\pi}=\frac{1}{2\pi}\sqrt{\frac{a_1}{a_3}} \qquad [\mathrm{Hz}]\ , \tag{4.1}$$

where the coefficients of the corresponding characteristic polynomials (3.6) and (3.9) should be calculated at the corresponding stability limit. When the reflex delay deviation is zero, this frequency varies between

$$0<f<\frac{\sqrt{2}}{2\pi}\frac{1}{\tau}\sqrt{\frac{l-3g\tau^2}{l+3g\tau^2}}\ . \tag{4.2}$$

The formula is much more complicated for the non-zero reflex delay deviation case, but it provides a similar range of frequencies.

5. **Critical reflex delay**

The stability domains in Figures 3 and 4 shrink as the characteristic time delay τ is increased either with zero or with non-zero reflex deviation characterized by 1/n. The critical time delay, where the stability domain disappears, can easily be calculated.

In the zero-deviation case, the stability conditions (3.6) lead to an empty set when

$$a_0=0, a_1=0, a_2=0 \ \Rightarrow\ \tau_{\mathrm{cr},n\to\infty}=\sqrt{\frac{l}{3g}}\ . \tag{5.1}$$

Similarly, the critical characteristic time delay is obtained from the stability conditions (3.9):

$$a_0=0, a_1=0, H_2=0 \ \Rightarrow\ \tau_{\mathrm{cr},n=2}=\sqrt{\frac{2l}{3g}}\ . \tag{5.2}$$

6. **Conclusions**

Some direct conclusions can be derived from the above linear theory of balancing an inverted pendulum. First of all, the stability charts clearly express the requirement of a combined application of proportional and differential controllers, that is, both the angle and angular velocity signals must be measured. Stabilization is impossible with one of the angle or the angular velocity signals only, when either P or D is zero. Although the self-balancing of the human body is a much more complicated process, but the balancing organ, the so-called labyrinth, in the inner ear of human beings also provides these signals. The corresponding two parts of the labyrinth are called static and dynamic receptors (see Figure 5), which provide a signal about the spatial inclination and angular velocity of the head.

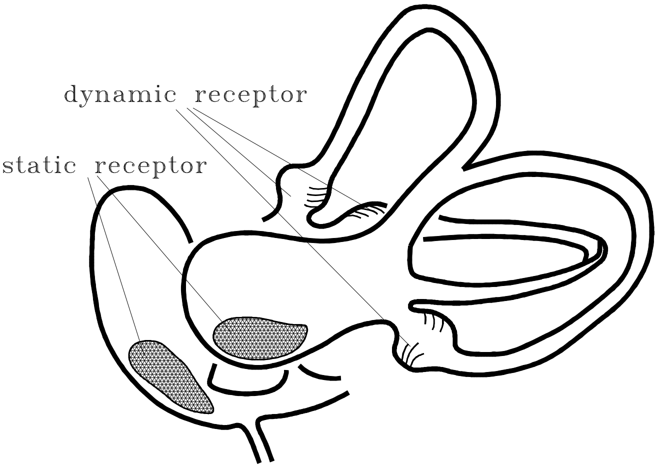

Figure 5. The labyrinth

The vibration frequencies given by formula (4.2) at the loss of stability also provide realistic numerical results. For the parameters given in Figure 3, the frequency range

$$0 < f < 3.5 \quad [\mathrm{Hz}]$$

fits to the experimental observations well [7].

In [6], the critical time delay was determined for the infinite dimensional model (2.6) exactly, without using the small time delay approximation in (3.6). Still, the result is exactly the same as in (5.1). For a 0.3 [m] long stick, this formula means a 0.1 [s] critical reflex delay. This is just about the mean value of the reflex delay from the eye through the brain and the arm to the fingers. After some practice, anybody can balance a stick of length 30 [cm], but we cannot do this with shorter ones. On the other hand, we are able to balance a sweep of length 1.5 [m] even on our toe, in spite of the fact that the time delay is much more in that direction, it is in the range of 0.7 [s]. When the deviation of the reflex delay is non-zero, the critical value of the characteristic delay is larger by a factor of $\sqrt{2}$ in accordance with formula (5.2).

Finally, some comments are given on the observation that balancing is never perfect, small amplitude stochastic oscillations persist even in cases when the balancing should be exponentially stable. This vibration is called micro-chaos [8,9,10]. The mechanism of this vibration is as follows. There is a certain threshold of our senses: below a certain angle, for example, our senses are not able to make a distinction between the tiny angle values and zero. Consequently, the control is switched off without input signals, and the stick starts falling from the close vicinity of the unstable upper position till the angle signal reaches the perception threshold, where the human control is switched on, again, and starts pushing back the pendulum close to the upper vertical position. Then, below the threshold level, again, the stick is left without control, and so on. This process leads to a small amplitude chaotic oscillation.

Similar micro-chaotic oscillation is observed in the walking of drunken people. While an increasing amount of alcohol first decreases, later increases the threshold level of perception, any small amount of alcohol consumed increases the reflex delay. The result is instability and a small amplitude random oscillation with low-frequency components at about 1 [Hz] in its continuous spectrum.

References

1. Moss, F. and Milton, JG.: Medical technology - Balancing the unbalanced. *Nature*, **425**, (2003), 911-912.
2. Stépán, G.: Micro-chaos in digitally controlled mechanical systems, in Nonlinearity and Chaos in Engineering Dynamics (Eds.: J.M.T. Thompson and S.R. Bishop), John Wiley & Sons, Chichester, 1994,. 143-154.
3. Bretz, K. and Kaske, R. J.: Some parameters of multiloop biofeedback control of posture. *Proceedings of XII Int. Symposium on Biomechanics in Sport*, (Siófok, 1994), 124-128.
4. Stépán, G. and Kollár, L.: Balancing with reflex delay. *Mathematical and Computer Modelling*, **31**, (2000), 199-205.
5. Kuo, B. C.: *Digital Control Systems.* SRL Publishing Company, Champaign, Illinois, 1977.
6. Stépán, G.: *Retarded Dynamical Systems.* Longman, Harlow UK, 1989.
7. Kawazoe, Y.: Manual control and computer control of an inverted pendulum on a cart, *Proc. 1st Int. Conf. on Motion and Vibration Control*, (Yokohama, 1992), 930-935.
8. Haller, G. and Stépán, G.: Micro-chaos in digital control. *Journal of Nonlinear Science*, **6**, (1996), 415–448.
9. Enikov, E. and Stépán, G.: Micro-chaotic motion of digitally controlled machines. *Journal of Vibration and Control*, **4**, (1998), 427-443.
10. Chen, G. and Dong, X.: *From Order to Chaos: Perspectives, Methodologies, and Applications.* World Scientific, Singapore, 1997.

Journal of Computational and Applied Mechanics, Vol. 7., No. 1., (2006), pp. 85–101

INDUSTRIAL ROBOT APPLIED IN NEUROREHABILITATION
[Arm and shoulder exercising by robot]

András Tóth, Gustáv Arz, László L. Kovács, Gábor Stépán
Budapest University of Technology and Economics
Műegytem rkp. 3-5., H-1521 Budapest, Hungary
`{toth|arz}@manuf.bme.hu, {kovacs|stepan}mm.bme.hu`

Gábor Fazekas
National Institute for Medical Rehabilitation
Szanatórium utca 19., H-1528 Budakeszi, Hungary
`kassai@alarmix.net`

[Received: August 31, 2004]

Abstract. This paper reports the latest results of the REHAROB IST-1999-13109 project. The objectives of the project; the structure of the REHAROB Therapeutic System, and the architecture of the applied teaching in force controller are presented. The paper also describes the results of the first clinical trial with the REHAROB Therapeutic System. The results proved that using industrial robots for passive motion therapy is a promising approach to improving motor deficit after stroke.

Keywords: stroke, neurorehabilitation, industrial robots, teaching in, force control

1. **Introduction**

A characteristic neurological impairment of stroke patients is the spastic hemiparesis of the limbs. Annual incidence of stroke is between 150 and 400 cases for each 100000 population in the European Union while it is 214 annual cases in the United States of America and 400 cases in Hungary [1]. Eighty percent of stroke survivors have significant neurological impairment. Sixty-nine percent of them can be rehabilitated successfully while the rest of the survivors need help in everyday activities. Evidence has shown that early and intensive motion therapy positively affects the restoration of the motor function after stroke [2]. Budget constraints, however, limit the realization of a labour-intensive, one-to-one, two times per day physiotherapy in the rehabilitation practice. Widely available Continuous Passive Motion (CPM) exercising machines used for post-surgical rehabilitation are not suitable for antispastic physiotherapy.

Research groups in the US, Asia, and Europe are attempting to develop robotic systems that would assist the physiotherapists in gait, trunk, balance, arm, hand, and finger rehabilitation of spastic hemiparetic patients. The ARM Guide [3], the MIME [4], the MIT-MANUS [5], ArmTrainer and the GENTLE/S [6] are the best known spastic arm physiotherapy systems. The MIT-MANUS has gained commercial success with a few installations, whilst the others remain operational in the developers' rehabilitation organizations.

2. The REHAROB therapeutic system

The REHAROB Therapeutic System [7] (shown in Figure 1) was designed to bring advances in three fundamental features of robotic antispastic physiotherapy:

1. REHAROB uses two robotic manipulators for controlled moving of the upper arm and the lower arm of the patient
2. REHAROB performs complex full anatomic Range of Motion (ROM) exercises on all possible shoulder girdle and elbow motions: shoulder protraction-retraction, shoulder elevation-depression, shoulder flexion-extension, shoulder abduction-adduction, shoulder external-internal rotation, elbow flexion-extension, and lower arm pronation-supination
3. REHAROB was built from mass produced commercial components like industrial robots in order to cut product costs and to achieve critical mass for viable production

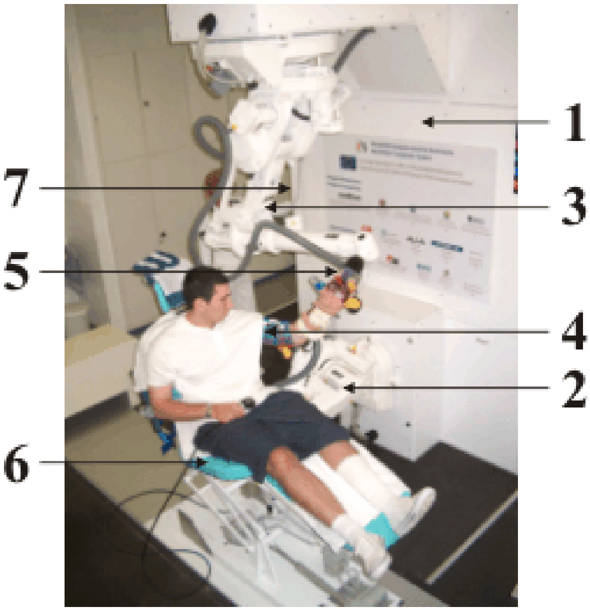

Figure 1. The REHAROB Therapeutic System: 1 Frame, 2 IRB 140 industrial robot, 3 IRB 1400H industrial robot, 4 Upper-arm orthosis, 5 Lower-arm orthosis, 6 Couch, and 7 Operating panel

Programming of the system is realized by demonstration of the exercises through force controlled industrial robots. For delivery of exercises to the patient two ABB industrial robots were selected: the wall mounted 0.8m reach IRB 140 industrial robot is connected to the upper arm and the inverted 1.4m reach IRB 1400H industrial robot is connected to the lower arm. A powered turnable couch positions the patient according to the required treatment which can be lying or sitting, and left arm or right arm for any patient size. Mechanical design of the frame and the couch was completed so that REHAROB is fully symmetrical to left arm and right arm therapy.

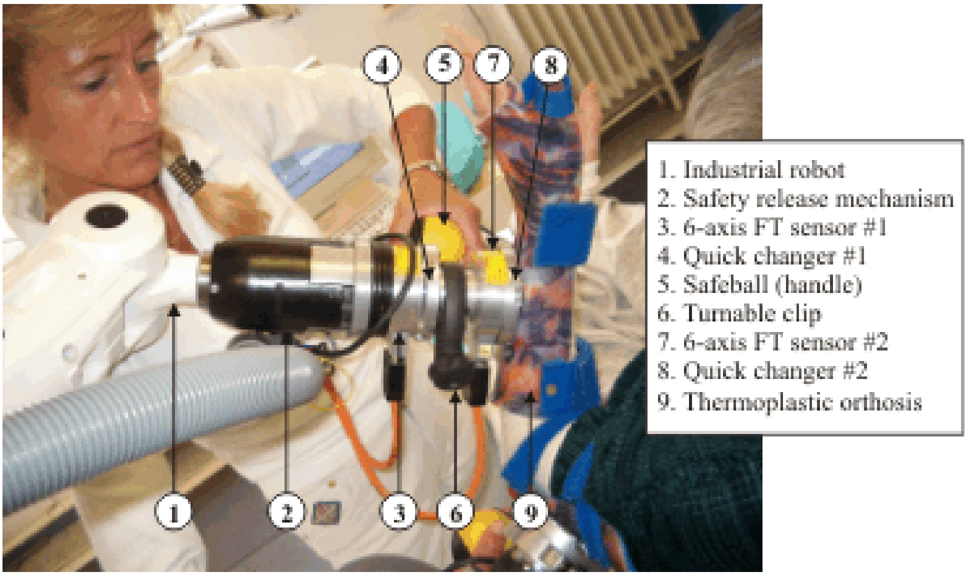

Figure 2. Teaching in of the physiotherapy exercises with the help of instrumented orthoses

The instrumented orthoses, which connect the patient's arm to the robots, include safety, control and coupling devices as follows (from left to right in Figure 2): Safety release mechanism, six DOF F/T sensor for force control, quick changer #1, safeball® with a turnable clip, six DOF F/T sensor for force monitoring, quick changer #2, three sized thermoplastic orthosis. The control system of REHAROB involves the two industrial robot controllers, the four sets of 6-axis force/torque measurement systems, the so-called watchdog PC and the high level controller PC. We have developed a novel outer-loop indirect force control method for programming the standard industrial robots [8]. This is called teaching in, during which the physiotherapist freely exercises the patient by leading the orthoses through the required trajectory with grasping the safeballs®, while the robots follow and learn the trajectories (see Figure 2). The operating devices and the user interface of the control system were designed not only for safety but also for the maximum comfort of the physiotherapist (PT). In addition to the control devices assembled on the orthoses and on the couch, there is an operating panel on the frame. The panel includes a Touch Screen Display, a keyboard, 3 buttons, and 3 switches only.

Figure 3. The operating panel and the user interface

Industrial robots, defined by the industrial robot safety standard EN ISO 8373:1994, must not be used in applications where contact with the human body can happen. The IRB 140 and the IRB 1400H industrial robots meet the requirements of 18 safety and harmonized standards (not listed here due to space limitations), which is a great advantage but does not make yet the system eligible for robotic physiotherapy. Special safety devices and monitoring programs were developed for, and tested with the robotic rehabilitation system. The REHAROB Therapeutic System is a medical device, so it meets fully the requirements of the relevant European directive, the Medical Device Directive [9].

3. **Mechanical model of the teaching in device**

The teaching in device of the robot is the part of the instrumented orthosis system. The main units of the device are: the safety release mechanism (SRM), the 6-axis FT sensor #1 and the safeball® as shown in Figure 4.

In the model presented the mass m_1 stands for the inertia of the SRM flange and half of the 6-xis FT sensor #1 (see Figure 2). The mass m_2 represents the mass of remaining part of the instrumented orthosis towards the patient's arm and also the mass of the patient's arm itself [10]. Stiffness s_1 is the effective stiffness of the elements located in the SRM, while s_2 denotes the stiffness of the FT sensor #1. The damping factors k_1 and k_2 model the small material damping of the helical springs of the SRM and the FT sensor #1, respectively. The dynamical parameters of the physiotherapist's hand are identified by stiffness s_3 and damping factor k_3.

In Figure 4 the coordinates x_1 and x_2 denote the positions of the center point of the FT sensor #1 and the safeball, respectively. The position of the robot is

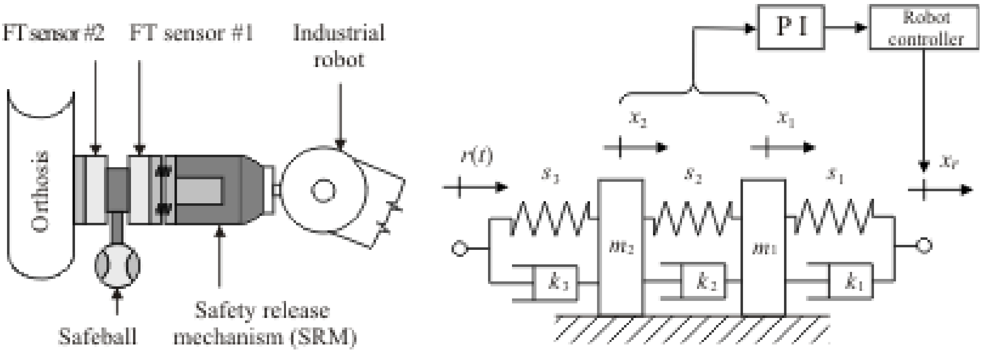

Figure 4. Mechanical model of the teaching in device

measured by the coordinate x_r and the physiotherapist's motion is described by the time dependent displacement function $r(t)$.

The equations of motion of the above one-dimensional mechanical model, i.e. the simplified model of the teaching in device, are as follows

$$\begin{aligned} m_1\ddot{x}_1 &= s_1(x_r - x_1) - s_2(x_2 - x_1) + k_1(\dot{x}_r - \dot{x}_1) - k_1(\dot{x}_r - \dot{x}_1) \\ m_2\ddot{x}_2 &= s_2(x_1 - x_2) - s_2(x_2 - r(t)) + k_2(\dot{x}_1 - \dot{x}_2) - k_1(\dot{x}_2 - \dot{r}(t)) \\ \dot{x}_r &= v_n \qquad t \in [t, t+\Delta t) \end{aligned} \tag{1}$$

where Δt is the controller's sampling time and v_n is the velocity of the robot for the actual sampling period. Then, using the notation $t_n = n\Delta t$ to denote time instants and introducing the state vector $\mathbf{x} = (x_1, x_2, \dot{x}_1, \dot{x}_2)$ the integration of the third equation in (1) yields the vector form

$$\dot{\mathbf{x}} = \mathbf{A}\mathbf{x} + [x_{r,n} + v_n(t - t_n)]\,\mathbf{b}_o + v_n\mathbf{b}_1 + \mathbf{u}(t)\,, \qquad t \in [t_n, t_{n+1})\,, \tag{2}$$

where the coefficient matrix $\mathbf{A}$ is

$$\begin{bmatrix} 0 & 0 & 1 & 0 \\ 0 & 0 & 0 & 1 \\ -\dfrac{s_1+s_2}{m_1} & \dfrac{s_2}{m_1} & -\dfrac{k_1+k_2}{m_1} & -\dfrac{k_2}{m_1} \\ \dfrac{s_2}{m_2} & -\dfrac{s_2+s_3}{m_2} & \dfrac{k_2}{m_2} & -\dfrac{k_2+k_3}{m_2} \end{bmatrix}, \tag{3}$$

and the non-homogeneous vector terms $\mathbf{b}_o$, $\mathbf{b}_1$ and $\mathbf{u}(t)$ are

$$\mathbf{b}_o = \begin{bmatrix} 0 \\ 0 \\ s_1/m_1 \\ 0 \end{bmatrix}, \quad \mathbf{b}_1 = \begin{bmatrix} 0 \\ 0 \\ k_1/m_1 \\ 0 \end{bmatrix}, \quad \mathbf{b}_o = \begin{bmatrix} 0 \\ 0 \\ 0 \\ r(t)\,s_3/m_2 + \dot{r}(t)\,k_3/m_2 \end{bmatrix}. \tag{4}$$

4. Teaching in force control strategy

The control strategy applied in REHAROB is defined as outer-loop or indirect force control in the literature [11]. The block scheme of the control is presented in Figure 5. Using this approach, the outer-loop force controller commands the position/orientation inputs to the robot controller. In this way, industrial robots become easily programmable by the technically not well-qualified physiotherapists.

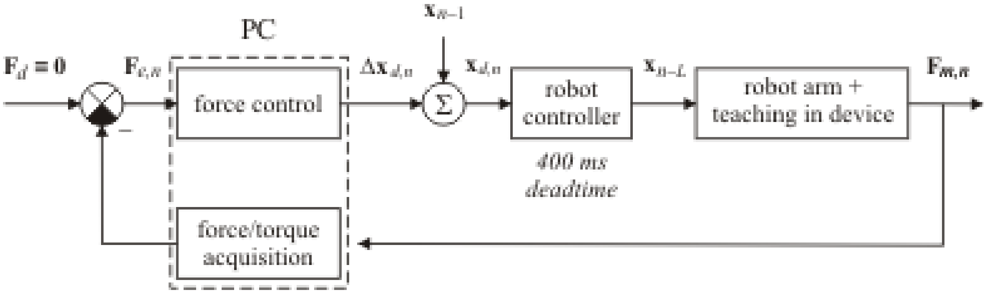

Figure 5. Outer-loop indirect force control

Figure 5 shows that the reference signal $\mathbf{F}_{e,n}$ of the outer-loop force controller is equal to the measured force $\mathbf{F}_{n,n}$ since the desired contact force $\mathbf{F}_d = 0$, or in other words, the robot is required to follow the physiotherapist's motion without any resistance. The outer-loop force controller commands the desired robot position/orientation $\mathbf{x}_{d,n}$ relative to the position $\mathbf{x}_{n-1}$ realized at the end of the previous sampling interval. In addition to the digital sampling effect, the control is also influenced by the 400 ms deadtime (confirmed by ABB) of the robot controller. This deadtime is modeled as the product of an integer L and the sampling time of the outer force control loop.

In REHAROB, the outer-loop force controller is integrated with the signal-processing unit of the 6-axis FT sensor. The commanded pose data are directly transferred to the robot using standard serial connection and the FT sensor can be sampled up to 1 kHz. However, due to the limitations in the communication speed (115 Kbit/s) and the limited number of executable motion instructions in a certain time period (approximately 65 instructions in a second) of the applied industrial robots, the feasible control frequency was found to be 10 Hz as a maximum.

The relatively low sampling frequency of the discrete time control and also the presence of the large deadtime in the system are against the stability of the outer force control loop. This also made it difficult to tune the parameters of the empirically derived PI control law

$$v_n = -K_p\left(x_{1,n-L} - x_{2,n-L}\right) - K_l \sum_{i=1}^{n} f_d^{n-j}\left(x_{1,j-L} - x_{2,j-L}\right)\Delta t\,, \quad t \in [t_n\, t_{n+1}) \tag{5}$$

where K_p and K_l are the proportional and integral gains of the controller, respectively. In addition, $f_d < 1$ is the weight factor of the special integral term, which provides descending weights for the past values of the measured force, expressed here via the deformation $x_1 - x_2$ of FT sensor #1.

5. **Stability analysis**

The stability of the simplified, one-dimensional model (see Figure 4) is investigated by the solution of the equation of motion (2). It is assumed in the form

$$\mathbf{x} = \mathbf{x}_r^d + \boldsymbol{\xi} \tag{6}$$

where $\boldsymbol{\xi}$ is a small perturbation around the desired robot motion which satisfies equation (2). Thus, the asymptotic stability of the zero trivial solution of the corresponding variational system

$$\dot{\boldsymbol{\xi}} = \mathbf{A}\boldsymbol{\xi} + \left[\xi_{r,n} + \vartheta_n (t - t_n)\right] \mathbf{b}_o + \vartheta_n \mathbf{b}_1 \ , \qquad t \in [t_n, t_{n+1}) \tag{7}$$

with the perturbed velocity

$$\vartheta_n = -K_p \left(\xi_{1,n-L} - \xi_{2,n-L}\right) - K_l \sum_{i=1}^{n} f_d^{n-j} \left(\xi_{1,j-L} - \xi_{2,j-L}\right) \Delta t \ , \quad t \in [t_n \, t_{n+1}) \tag{8}$$

refers to the realization of the desired robot motion and zero contact force. Note that the trajectory error corresponding to the error of the outer force control loop is a function of the control and mechanical parameters.

The stability investigation of the piecewise continuous system (7) is carried out via the analytical construction of a discrete mapping possessing the same stability properties [12]. In order to construct this mapping the following four-step algorithm is advised

1. The general solution of (7) has to be calculated for the interval.
2. The constant of the general solution has to be determined by the substitution of the initial condition into the general solution of (7).
3. The state variable has to be calculated at the end of the n^{th} sampling period.
4. Choosing an appropriate discrete state vector, it is practical to arrange the results in a dense matrix form.

According to the above algorithm, the stability of the trivial solution of (7) can be investigated by the convergence of the discrete mapping

$$\boldsymbol{\xi} = \mathbf{P}\boldsymbol{\xi}_n + \mathbf{Q}\mathbf{b}_o\vartheta_n + \mathbf{R}\mathbf{b}_o\boldsymbol{\xi}_{r,n} + \mathbf{R}\mathbf{b}_1\vartheta_n \tag{9}$$

where the corresponding coefficient matrices are

$$\begin{aligned} &\mathbf{P} = \exp\left(\mathbf{A}\Delta t\right) \ , \quad \mathbf{Q} = \exp\left(\mathbf{A}\Delta t\right) \mathbf{A}^{-2} - \mathbf{A}^{-2} - \mathbf{A}^{-1}\Delta t \ , \\ &\mathbf{R} = \exp\left(\mathbf{A}\Delta t\right) \mathbf{A}^{-1} - \mathbf{A}^{-2} \end{aligned} \tag{10}$$

In addition, the perturbed velocity (8) of the robot can be formulated as

$$\vartheta_n = -P \left(\xi_{1,n-L} - \xi_{2,n-L}\right) - I\xi_{int,n-L} \tag{11}$$

where $\xi_{int,n-L}$ is defined by the recursive formula

$$\xi_{int,n-L} = f_d\, \xi_{int,n-L-1} + (\xi_{1,n-L} - \xi_{2,n-L})\, \Delta t\ . \tag{12}$$

Applying the notation $\Delta\xi_n = \xi_{1,n} - \xi_{2,n}$ for the perturbed deformation of the FT sensor #1, the discrete mapping (9) can be expressed in the form

$$\mathbf{z}_{n+1} = \mathbf{D}\, \mathbf{z}_n \tag{13}$$

where the discrete state vector is

$$\mathbf{z}_n = \Big[\xi_{r,n},\ \xi_{1,n},\ \xi_{2,n},\ \dot{\xi}_{1,n},\ \dot{\xi}_{2,n},\ \xi_{int,n-L-1},\ \Delta\xi_{n-L},\ \Delta\xi_{n-L+1}\,, \ldots, \Delta\xi_{n-1}\Big]^T\ . \tag{14}$$

Finally, the so-called transition matrix has the form

$$\mathbf{D} = \begin{bmatrix}
1 & 0 & 0 & 0 & 0 & -\hat{K}_l\Delta t & -\hat{K}_p\Delta t & 0 & 0 & \cdots & 0 & 0 \\
R_{13}\frac{s_1}{m_1} & P_{11} & P_{12} & P_{13} & P_{14} & D_{26} & D_{27} & 0 & 0 & \cdots & 0 & 0 \\
R_{23}\frac{s_1}{m_1} & P_{21} & P_{22} & P_{23} & P_{24} & D_{36} & D_{37} & 0 & 0 & \cdots & 0 & 0 \\
R_{33}\frac{s_1}{m_1} & P_{31} & P_{32} & P_{33} & P_{34} & D_{46} & D_{47} & 0 & 0 & \cdots & 0 & 0 \\
R_{43}\frac{s_1}{m_1} & P_{41} & P_{42} & P_{43} & P_{44} & D_{56} & D_{57} & 0 & 0 & \cdots & 0 & 0 \\
0 & 0 & 0 & 0 & 0 & f_d & \Delta t & 0 & 0 & \cdots & 0 & 0 \\
0 & 0 & 0 & 0 & 0 & 0 & 0 & 1 & 0 & \cdots & 0 & 0 \\
0 & 0 & 0 & 0 & 0 & 0 & 0 & 0 & 1 & \cdots & 0 & 0 \\
0 & 0 & 0 & 0 & 0 & 0 & 0 & 0 & 0 & \cdots & 0 & 0 \\
\vdots & \vdots & \vdots & \vdots & \vdots & \vdots & \vdots & \vdots & \vdots & \ddots & \vdots & \vdots \\
0 & 0 & 0 & 0 & 0 & 0 & 0 & 0 & 0 & \cdots & 0 & 1 \\
0 & 1 & -1 & 0 & 0 & 0 & 0 & 0 & 0 & \cdots & 0 & 0
\end{bmatrix} \tag{15}$$

in which

$$D_{i6} = -\hat{K}_l \left(Q_{i-1,3}\frac{s_1}{m_1} + R_{i-1,3}\frac{k_1}{m_1}\right)\ , \quad D_{i7} = -\hat{K}_p \left(Q_{i-1,3}\frac{s_1}{m_1} + R_{i-1,3}\frac{k_1}{m_1}\right)\ . \qquad i = 2, \ldots, 5 \tag{16a}$$

The modified control gains $\hat{K}_p$ and $\hat{K}_l$ are defined by

$$\hat{K}_p = K_p + K_l\, \Delta t \qquad \text{and} \qquad \hat{K}_l = f_d\, K_l\ . \tag{16b}$$

Stability of the zero trivial solution of (7) is determined by the eigenvalues of the coefficient matrix (15). If all the eigenvalues μ_k $k = 1, 2, \ldots, L+6$ of the transition matrix $\mathbf{D}$ (the so-called characteristic multipliers) are located inside the open unit disc of the complex plane, then the system is asymptotically stable [12,13].

Taking into consideration the model parameters listed in Table 1 and Table 2, the corresponding stability chart is shown in Figure 6. The dynamic parameters of the physiotherapist's hand were estimated by simple experiments and intuition. These parameters can, naturally, vary in a certain range. Table 1 defines the range of the stiffness parameter between 2000 and 5000 N/m, while the corresponding damping factors are given to provide a realistic (relative) damping ratio of 80%.

Table 1. Mechanical parameters

Symbol	**Value**	**Symbol**	**Value**
m_1	0.1 [kg]	m_2	4 [kg]
s_1	15000 [N/m]	s_2	10^7 [N/m]
s_3	2000 t 5000 [N/m]	k_1	1 [Ns/m]
k_1	1 [Ns/m]	k_2	143 – 226[Ns/m]

Table 2. Control parameters

Symbol	**Description**	**Value**
K_p	Proportional gain	4000 [1/s]
K_l	Integral gain	4000 [1/s^2]
f_d	Dissipation factor of the integral term	0.7 [-]
Δt	Sampling time	100 [ms]
L	Deadtime parameter	4 [-]

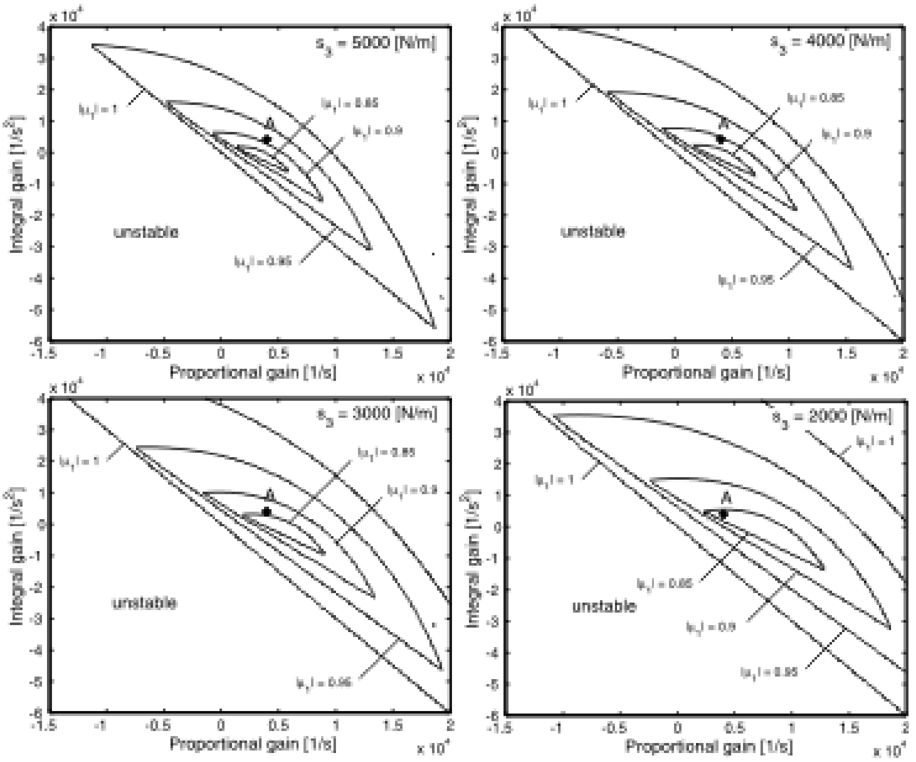

Figure 6. Stability chart of the control gains varying with stiffness s_3

The experimentally tuned gain parameters $K_p = 4000\,[1/s]$ and $K_f = 4000\,[1/s^2]$ are denoted by point A. This point is near the central region of each chart where the characteristic multiplier $|\mu_1| \leqslant 0.85$ is small enough to provide fast decaying control.

6. **Simulation and experimental results**

The stability charts presented in the previous section are calculated semi-analytically. These charts correspond to the simplified, one-dimensional mechanical model shown in Figure 4 with the measured and estimated mechanical and control parameters listed in Table 1 and Table 2, respectively. The accuracy of the charts presented was tested by simulation and experiments.

During the clinical test of REHAROB (see Section 5 for details) a large number of exercises were recorded. A typical taught in trajectory in one direction is presented in Figure 7.

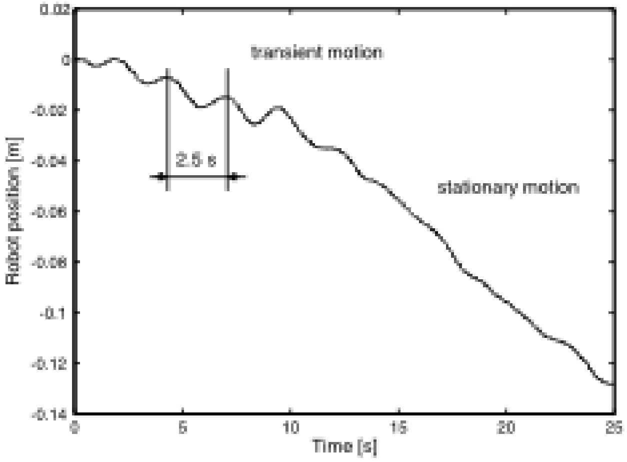

Figure 7. Measured robot trajectory

Figure 7 shows that each exercise segment starts with a transient because even a skilled physiotherapist cannot compensate completely for the deadtime during start of teaching in an exercise. The frequency of these transient vibrations can be estimated by

$$f = \frac{Im(\ln \mu_{A,1})}{2\pi\Delta t} = 0.422\ [\mathrm{Hz}]\ , \tag{17}$$

where $\mu_{A,1} = 0.8812 + 0.2393i$ is the largest characteristic multiplier at point A. The good agreement between this analytical result and the measured frequency 0.4 Hz of the transient motion presented in Figure 7 verifies the simplified, one-dimensional model and its parameters. The transient motion of the model was simulated by Simulink® Matlab®. The simplified block scheme of the Simulink® model is presented in Figure 8.

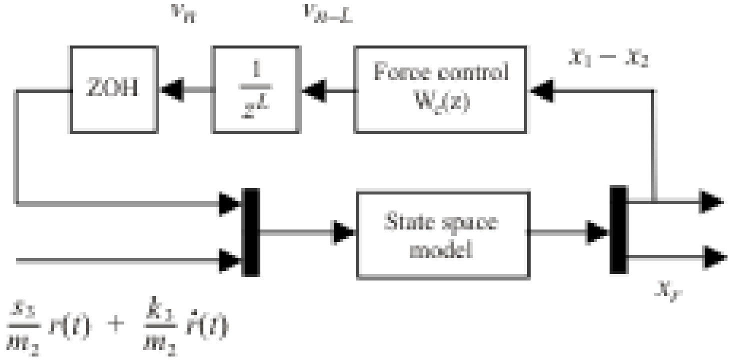

Figure 8. Simplified block scheme of the Simulink® model

In the simulation, the dynamics of the system was modeled by the state-space representation of (1) as follows

$$\begin{bmatrix}\dot{x}_r\\ \dot{\mathbf{x}}\end{bmatrix} = \left(\begin{bmatrix}0\\ \mathbf{b}_o\end{bmatrix}\begin{bmatrix}1&0&0&0&0\end{bmatrix} + \begin{bmatrix}0&\mathbf{0}^T\\ \mathbf{0}&\mathbf{A}\end{bmatrix}\right)\begin{bmatrix}x_r\\ \mathbf{x}\end{bmatrix} + \\ + \begin{bmatrix}1&0&0&0&0\\ 0&0&0&0&1\end{bmatrix}^T \begin{bmatrix}v_n\\ \mathbf{u}(t)\end{bmatrix}, \tag{18}$$

$$\begin{bmatrix}x_1 - x_2\\ x_r\end{bmatrix} = \begin{bmatrix}0&1&-1&0&0\\ 1&0&0&0&0\end{bmatrix}\begin{bmatrix}x_r\\ \mathbf{x}\end{bmatrix} + \begin{bmatrix}0&0\\ 0&0\end{bmatrix}\begin{bmatrix}v_n\\ u(t)\end{bmatrix}. \tag{19}$$

According to the expression (5) of the control law, the outer-loop force controller has the impulse transfer function

$$W_c(z) = \frac{v_n(z)}{x_{1,n}(z) - x_{2,n}(z)} = \frac{-(K_P + K_I \Delta t)z + K_P f_d}{z - f_d}, \tag{20}$$

which transforms the impulse sequence of the sensor deformations $x_1 - x_2$ into the prescribed velocities at discrete time instants. The input $r(t)$, i.e. the motion that the physiotherapist would achieve, is generated from the measured robot trajectory presented in Figure 7. The desired motion is calculated by the 9^{th} order polynomial approximation of the measured data. The desired, simulated and measured robot trajectories are presented in Figure 9, which shows that the transient vibration in the simulated time history can be observed for the initial 2 seconds only, which is in contrast with the measurements. A possible explanation for this is that the mechanical and the control model of the physiotherapist is oversimplified. Note that in the one-dimensional model applied only the stiffness s_3 and the damping k_3 dynamic parameters represent the physiotherapist. However, the reflex delay of the physiotherapist shall also affect the system dynamics in a somewhat destabilizing way [14].

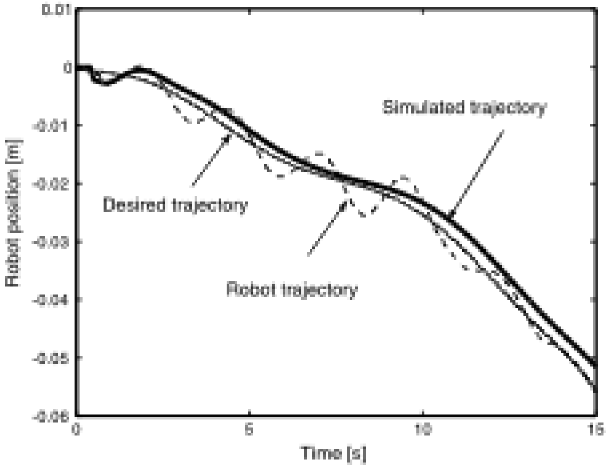

Figure 9. Desired, simulated and the measured robot trajectories

7. **Clinical testing**

The REHAROB Therapeutic System was installed in the National Institute for Medical Rehabilitation, Budapest, Hungary for clinical testing. It is very important to note that clinical testing is the formal part of medical certification, and its objective is not the study of the clinical efficiency but, as quoted to verify that, under normal conditions of use, the performance of the devices conform to those intended by the manufacturer, and to determine any undesirable side-effects, under normal conditions of use, and assess whether they constitute risks when weighed against the intended performance of the device. The clinical testing started on the 6^{th} of April 2003 with three healthy female and one male volunteers of age from 28 to 44. The second group and the third group of subjects included patients. The patient's clinical data are shown in Table 3. Each subject received 30 minutes net robotic physiotherapy, excluding sitting in- and out, and teaching in the exercises on 20 consecutive working days. After 7200 minutes total robotic physiotherapy the clinical trial ended on the 8^{th} of July 2003.

Table 3. Clinical data of the patients

Patient #	**Sex**	**Age**	**Diagnosis**	**Setting up**	**Hand affected**
R1	Male	71	Ischaemic stroke	9 years ago	Right
R2	Male	64	Ischaemic stroke	9 years ago	Right
R3	Male	26	Subdural haemorrhage	5 years ago	Right
R4	Female	56	Subarachnoideal haemorrhage	3 years ago	Right
R5	Female	66	Ischaemic stroke	5 weeks ago	Left
R6	Male	20	Epidural haemorrhage	9 months ago	Left
R7	Male	46	Basilar artery thrombosis	22 months ago	Right
R8	Male	25	Cavernoma pontis	8 weeks ago	Right

Each patient was assessed at the entry to and at the discharge from the robotic therapy session, as well as in a month follow up period. Traditional scales were used for the assessment of the impairment status and the disability of the patients. The traditional semi-quantitative scales were the Modified Ashwort Score, the FIM score (Total FIM score and separately the self-care score), and the Barthel index. Assessment of the motion ranges at two anatomic joints was made by biomechanical measurements: the CMS HS type Motion Analyzing System of zebris Medizintechnik Ltd was used [15]. Tables 4, 5, 6, and 7 show the assessment results.

The average score of shoulder adductors at admission was 1.25, while at discharge it was 1.125 which means a 10% improvement. The average score of elbow flexors at admission was 1.75, while at discharge it was 1.375 which means a 21,4% improvement. The Ashworth score of the patient #R8 has increased. When starting the therapy he had flaccid hemiparesis, as it is usual during the first weeks after the brain damage. Spasticity appeared later, as it is frequent in such cases. We suppose that without the robot-mediated physiotherapy, the increase in Ashworth score could have been higher.

Table 4. Modified Ashworth score of shoulder adductors and elbow flexors of the affected side

Patient #	**Shoulder adductors**		**Elbow flexors**	
	Admission	**Discharge**	**Admission**	**Discharge**
R1	1	1	2	1
R2	2	2	3	2
R3	0	0	1	0
R4	1	1	2	2
R5	2	2	3	2
R6	1	0	2	1
R7	3	2	3	3
R8	0	1	0	1

Table 5. Range of movement of elbow flexion-extension and pronation-supination of of the affected side

Patient #	**Elbow flexion-extension [degree]**		**Pronation-supination [degree]**	
	Admission	**Discharge**	**Admission**	**Discharge**
R1	80	87	133	137
R2	84	96	75	107
R3	106	107	120	124
R4	46	78	35	65
R5	89	99	97	97
R6	71	88	53	59
R7	29	52	47	69
R8	82	71	41	89

Table 6. FIM and self care scores (self care is a part of the total FIM score)

Patient #	**Total FIM score**		**Self-care**	
	Admission	**Discharge**	**Admission**	**Discharge**
R1	121	122	42	42
R2	115	122	36	42
R3	106	126	36	42
R4	115	115	36	36
R5	86	89	25	26
R6	98	106	32	35
R7	111	113	36	36
R8	103	115	29	36

Table 7. Barthel index

Patient #	**Admission**	**Discharge**
R1	100	100
R2	100	100
R3	100	100
R4	90	100
R5	70	80
R6	85	95
R7	90	95
R8	65	100

The average elbow flexion at admission was 69.5 degrees, while at discharge it was 84.75 degrees which means a 21.9% improvement. The average pronation-supination at admission was 75.1 degrees, while at discharge it was 93.4 degrees which means a 24,3% improvement.

The average FIM (Functional Independence Measure) score at admission was 106.875, while at discharge it was 113.5, which means a 6.2% improvement. The average self-care score at admission was 34, while at discharge it was 36.875, which means a 8,46% improvement. The average Barthel index at admission was 87.5, while at discharge it was 96.25, which means a 10% improvement.

The Tables show that most of our patients were not seriously disabled; we have selected them intentionally to start the first clinical trial of the REHAROB Therapeutic System with non-serious cases. Most of our patients had their brain damage years ago, nevertheless robotic physiotherapy has improved their state regarding both the level of impairment and disability. Follow up assessments proved that all patients retained their discharge statuses. To prove the clinical and economic efficiency of the robotized physiotherapy will be the objective of a second controlled trial, which is planned for next year. The most important conclusions of the current clinical trial are as follows:

1. The robotic physiotherapy system was working continuously, reliably and safely; there were no delays due to technical or other problems.
2. The patients were not afraid of the robots; they found the robotized therapy interesting and useful.
3. The physiotherapists learnt easily how to work with the robots; the user interface proved to be really user friendly.
4. Based on the physiotherapists experience smaller improvement of the system is planned such as the improvement of the safety release mechanism, the armpit support, the headrest of the couch, and the patient enabling device.

6. Conclusions

The first prototype robotic physiotherapy system has proved that standard industrial robots are suitable for robotic physiotherapy. The REHAROB Therapeutic System has some unrivalled features among the passive physiotherapy machines and robots for spastic hemiparetic patients. Such features are that REHAROB uses two synchronized robotic arms, and exercises the spastic limb over the full ranges of the 5 shoulder and shoulder girdle joints as well as the 2 elbow joints.

An attempt was made to uncover the background of the realized, and successful force control of the industrial robots. A simplified, one-dimensional model of the teaching in device was used to analyse the stability of the outer-loop, digital force control. The effect of the digital sampling and the deadtime of the robot controller is presented in the form of stability charts. These stability charts derived from the simple model confirmed the experimental results. The investigation also revealed the intricate dynamics of discrete time systems with deadtime. Results drew the attention of engineers to the destabilizing effect of digital sampling and deadtime. The current standard industrial robot controllers limit the use of these devices to physiotherapy, but with evolution of the controllers due to industrial market needs the limitations will soon disappear. In case of REHAROB the two S4C+ controllers will be replaced by the new generation of IRC5 controllers, which offers a radical improvement in the performance of outer-loop control.

All the patients included in the clinical trial have shown significant improvement in their impairment and disability indicators. Patients have found the duration, the constancy, the power, and the complexity of robotic exercises effective and calming compared with the traditional manual passive physiotherapy. As beside the robotic approach our patients received traditional physiotherapy as well, we cannot conclude with certainty that the positive changes in the status of the patients were due to the robot-mediated therapy alone. It will be the aim of the second clinical trial to prove the true clinical efficacy of the system. After minor system improvements, one year long, controlled trial is planned for 2004 and 2005 in the framework of the FIZIOROBOT project supported by the Ministry of Health, Social and Family Affairs, Hungary. The cost of the first prototype system is rather high, approx. Euro 250,000 in comparison with the average patient day costs, that is Euro 500 in Europe and Euro 1000 in the USA for large rehabilitation centres. Based on the outcome of the second controlled trial, the REHAROB system can be optimised, and prepared for serial production and introduction to the market.

We believe that medical robotics applications must benefit from the use of mass produced and reliable industrial robots. The REHAROB Therapeutic System opens up a strong perspective of moving from taught in passive repetitive exercising to biomechanical-knowledge-based automatic passive, and later purely active upper and lower limb physiotherapy. In this respect the REHAROB Therapeutic System could cover all physiotherapy needs of a spastic hemiparetic stroke patient. In the distant future a customized physiotherapy and rehabilitation strategy for each patient can be developed and delivered automatically.

Acknowledgement. This research is sponsored by the European Commission through the IST-1999-13109 project, and by the Ministry of Health, Social and Family Affairs, Hungary through the ETT-073/2003 project and by the Hungarian National Science Foundation under grant No. OTKA T043368. Special thanks are due to the engineering and medical colleagues Mihály Jurák, Györgyi Stefanik, and Zsuzsanna Boros.

References

1. Feher, M. and Denes, Z.: *Neuro-rehabilitation in Medical Rehabilitation.* Medicina Publisher Co., Budapest, 2005. (in Hungarian)
2. Taub, E., Miller, N. E., Novak, T. A., Cook, E. W., Fleming, W. C., Nepomuceno, C. S., Connell, J. S. and Crago J. E.: Technique to improve chronic motor deficit after stroke. *Arch Phys Med Rehabil,* **74(4)**, (1993), 347-354.
3. Lum, P., Reinkensmeyer, D., Mahoney, R., Rymer, W. Z. and Burgar, C.: Robotic devices for movement therapy after stroke: current status and challenges to clinical acceptance. *Top Stroke Rehabil.*, **8**(4), (2002), 40-53.
4. Burgar, C. G., Lum, P. S., Shor, P. C. and Van der Loos H. F. M.: Development of robots for reha-bilitation therapy: The Palo Alto VA/Stanford experience. *J. Rehabil. Res. Dev.*, **37**(6), (2000), 663-673.
5. Krebs, H. I., Volpe, B. T., Ferraro, M., Fasoli, S., Palazzolo, J., Rohrer, B., Edelstein, L. and Hogan, N.: Robot-aided neurorehabilitation: from evidence-based to science-based rehabilitation. *Top Stroke Rehabil.*, **8**(4), (2002), 54-70.
6. Amirabdollahian, F., Loureiro, R., Driessen, B. and Harwin, W.: Error Correction Movement for Machine Assisted Stroke Rehabilitation. In M. Mokhtari (ed.), *Integration of Assistive Technology in the Information Age*, IOS Press, Amsterdam, 2001, pp. 109-116.
7. Arz, G., Toth, A., Fazekas, G., Bratanov, D. and Zlatov, N.: Three-dimensional Anti-spastic Physiotherapy with the Industrial Robots of "REHAROB". *In Proc 8th Int Con Rehabilitation Robotics*, KAIST 2003, pp. 215-218.
8. Kovacs, L.~L., Toth, A., Stepan, G., Arz, G. and Magyar, G.: Industrial Robot in a Medical Application – Back to Walk-through Programming. In D.~T. Pham, S.~S. Dimov, V.~O. O'Hagan (eds.), *Advances in Manufacturing Technology – XV.*, Professional Engineering Publishing Limited, London, 2001, pp. 479-484.
9. Council Directive 93/42/EEC of 14 June 1993 concerning medical devices.
10. Hall, S. J.: *Basic Biomechanics.* WCB McGraw-Hill, 1999.

11. Pires, J. N., Ramming, J., Rauch, S. and Araúio R.: Force/Torque sensing applied to industrial robotic deburring. *Sensor Review*, **22**(3), (2002), 232-241.
12. Kuo, B. C.: *Digital Control Systems.* SRL Publishing Company, Champaign, Illinois, 1977.
13. Lakshmikantham, V. and Trigiante, D.: *Theory of Difference Equations, Numerical Methods and Applications.* Academic Press, London, 1988.
14. Stépán, G., Kollár, L.: Balancing with reflex delay. *Mathematical and Computer Modelling*, **31**, (2000), 199-205.
15. Fazekas, G., Feher, M., Kocsis, L., Stefanik, G., Boros, Z. and Jurak, M.: Application of kinematical parameters for the assessment and monitoring of central motoneuron impair-ments. *Clin. Neurosci./Ideggy. Szle.*, **55**(7-8), (2002), 268-272. (in Hungarian)

Journal of Computational and Applied Mechanics, Vol. 7., No. 1., (2006), pp. 103–112

A SIMPLE MEMBRANE MODEL DOING DIVISION

József Verhás
Institute of Physics, Budapest University of Technology and Economy.
H-1111 Budapest, Hungary
`verhas@phy.bme.hu`

[Received: September 16, 2004]

Abstract. The continuous deformations of a fluid membrane bounded vesicle starting from a sphere are determined by minimizing the bending energy. Particular choice of the parameters and the fine points of the computations are presented. The computations show the pathway to cell division and to gastrulation.

Mathematical Subject Classification: 76M99
Keywords: bending energy, cell proliferation, gastrulation

1. Introduction

The mechanical properties of a fluid membrane with bending energy explain a number of phenomena. Perhaps the most important application of the model concerns biology – namely, the origin of life – but it also applies for the formation and structure of micro emulsions [1], moreover, for the theory of washing [2]. The shape transformation of a vesicle bounded with such a membrane explains quantitatively the form of the human red blood cell [3], gives a simple model of cell proliferation [4], gastrulation [5], and budding [2]. Moreover, combined with adhesion [6], it can model the formation of more complicated biological structures.

The mathematical model for the contribution of bending to the free energy or to the free enthalpy (or best to the availability) – the mathematical expression is the same – was introduced by Helfrich [1, 3, 7] and applied to the shape of the red blood cell and the formation of micro spheres from floating films [1]. The model is a two dimensional specialization of the Oseen–Frank [7, 8] theory of three dimensional liquid crystals. However, the area of the membrane and – in the case of a closed vesicle – the surrounded volume changes during the process, when looking for the shape the contribution of bending may be assumed minimal at constant volume and constant area. The representativity of the shapes obtained from the minimum of one of the above potential functions is based on the hypothesis that the mechanical motion runs on a much faster time scale than the osmotic or the chemical processes.

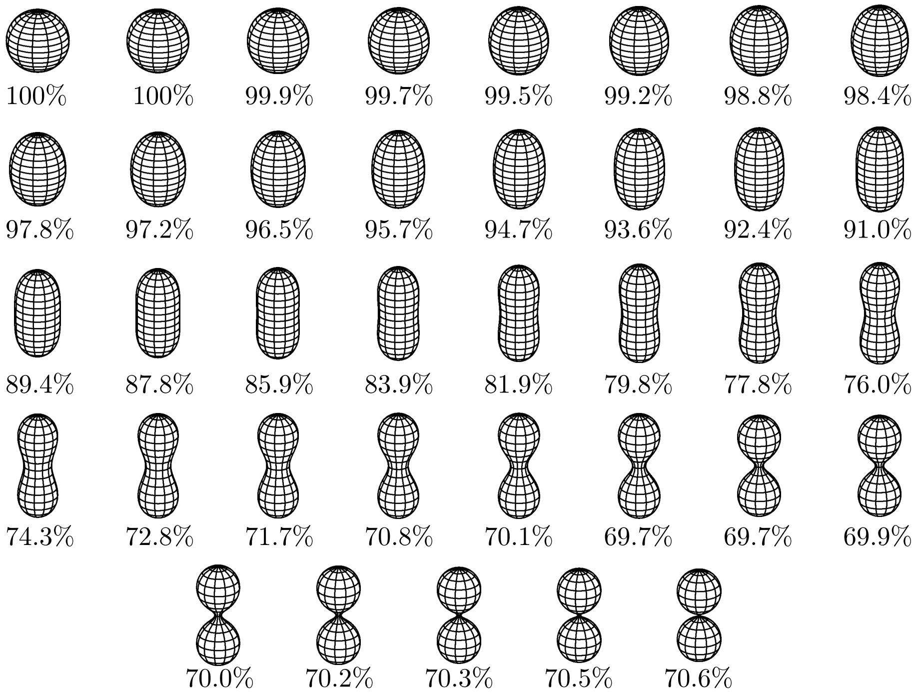

Percentage under 70.7% shows that the shape is unstable; the process is fast.

Figure 1. Forms of self-reproduction and degree of saturation*.

*The WEB page "http://newton.phy.bme.hu/˜verhas/" shows them in animation.

In most works, axisymmetric forms are presumed, which reduces the computational difficulties, so are they in this paper as well. Recently the break of axial symmetry is also investigated [9]. Although, the mathematical tools for treating the the above variational problem have been worked out in mathematics and can be found in textbooks, the representation of the variables used may lead to unusual situations emerging; so the mathematical analysis of the variational technics is not superfluous.

A number of works assume the membrane as a liquid bilayer and the quantitative properties of the membrane are analysed by statistical methods [10], however, the model may apply for other types of surfaces, e.g., for an interface between two phases – water and oil – in the presence of a surfactant [2]. The membrane may be even a tissue of cells as well.

As it has been mentioned, the variational principle displays a great variety of forms. The computations of the present author show only two continuous pathways of shape transformation starting from a sphere and leading to forms of biological relevance. The first one — which was the goal of the original research — leads to proliferation as shown in Figure 1 together with the percentage of the volume to the maximal one having room in the same envelope.

First the spherical symmetry loses stability and elongated shapes form; later neck formation occurs and the neck becomes narrower and narrower. The lateral symmetry holds for all the forms. The importance of this pathway lies in the fact that the membrane model is simple enough and the spontaneous formation under prebiotic circumstances can be imagined. The mechanism of proliferation in case of a modern organism is more complicated but it may only be the result of evolution. On the other hand, there is no evolution without proliferation. The first living beings had to proliferate with a simpler mechanism than the modern ones. On the other hand, evolution insists on 'good solutions'; some details of the present sketch are present nowadays, [11, 12, 13, 14] as well.

The other pathway leads to gastrulation as shown in Figure 2. First the spherical symmetry breaks and flattened shapes with lateral symmetry form; later the lateral symmetry loses stability and the gastrulated forms develop. Over the explanation of gastrulation an alternative mechanism for the formation of the first micro spheres is also obtained. The hole decreases and its closure is possible. Along this pathway, a droplet with a particular surface may transform into a micro sphere, moreover, a second, third, etc. gastrulations can occur as many times as the conditions are suitable. This way, self-generated membranes with a rather complicated structure can emerge out of the ancient broth.

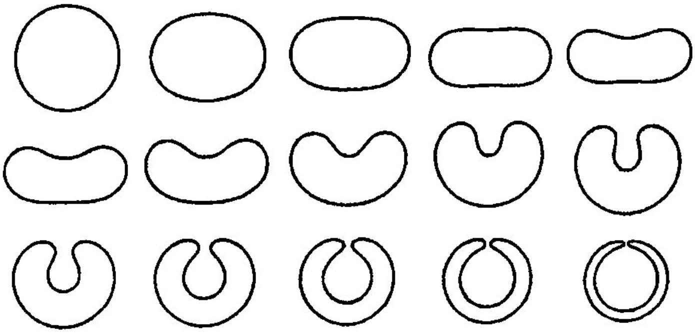

Figure 2. Forms of gastrulation

2. The mathematical model

The determination of the vesicle shape is based on the variational principle with the Lagrangian

$$2\pi x \left\{ K_0(c_1 + c_2 - a)^2 + K_0 c_1 c_2 \right\}. \tag{2.1}$$

where c_1 and c_2 are the principal curvatures, K_0, K_1, and a are material constants characteristic of the membrane. In general, the variational problem is rather difficult; it is easier if axisymmetric forms are taken into account. In this case, the contour is to be determined and the variational problem leads to ordinary differential equations.

Set a Cartesian frame the axis y of which is the axis of symmetry and take the contour curve in the x–y plane. For a smooth surface, the curve intersects the axis y orthogonally and does not intersect itself. To determine the curve, the internal representation is chosen, i.e., the arc length of the curve measured from the bottom (or from the top) and the angle α between the tangent of the curve and the axis x. For convenience, the redundant variable, the coordinate x of the point is also introduced (Figure 3); it is determined by the differential equation

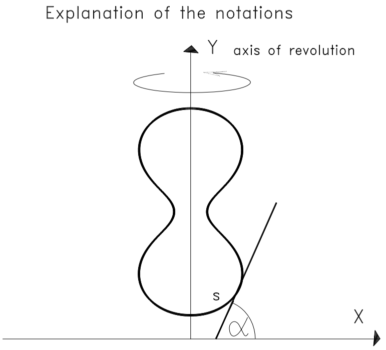

Figure 3. The notation

$$\frac{dx}{ds} = \cos\alpha\ . \tag{2.2}$$

The expressions for the principal curvatures are well known from the differential geometry:

$$c_1 = \frac{d\alpha}{ds} \qquad \text{and} \qquad c_2 = \frac{\sin\alpha}{x}. \tag{2.3}$$

The contribution of bending to the free energy takes the form

$$\int \left[K_0 \left(\frac{d\alpha}{ds} + \frac{\sin\alpha}{x} - a^* \right)^2 + K_1 \frac{\sin\alpha}{x}\frac{d\alpha}{ds} \right] 2\pi x\, ds \tag{2.4}$$

in the representation used. The area of the membrane and the surrounded volume are given as

$$\Omega = \int 2\pi x\, ds \qquad \text{and} \qquad F = \int \pi x^2 \sin\alpha\, ds \tag{2.5}$$

The integrations are extended from the bottom to the top.

3. **Calculations**

The functions $\alpha(s)$ and $x(s)$ are determined with the help of the standard methods of variational calculus. The auxiliary Lagrangian reads

$$F^* = \left[K_0\left(\frac{d\alpha}{ds}+\frac{\sin\alpha}{x}-a^*\right)^2+K_1\frac{\sin\alpha}{x}\frac{d\alpha}{ds}\right]2\pi x +$$
$$+\lambda_1 2\pi x+\lambda_2\pi x^2\sin\alpha+\mu(s)\left(\frac{dx}{ds}-\cos\alpha\right)\ . \tag{3.1}$$

Here λ_1, λ_2, and $\mu(s)$ are Lagrangian multipliers; λ_1 and λ_2 are constants while $\mu(s)$ is a function according to the constraint conditions that the area and the volume are given and x has to satisfy a differential equation. The formal variation of the integral of the auxiliary Lagrangian compared to that of the availability shows that λ_1 is the interfacial tension and λ_2 is the underpressure inside the vesicle. The set of the Euler–Lagrange differential equations reads

$$\begin{gathered} x\frac{d^2\alpha}{ds^2}+\cos\frac{d\alpha}{ds}-\frac{1}{x}\sin\alpha\cos\alpha=\frac{\lambda_2}{4K_0}x^2\cos\alpha+\frac{\mu}{4\pi K_0}\sin\alpha\ , \\ \left(\frac{d\alpha}{ds}-a^*\right)^2-\left(\frac{\sin\alpha}{x}\right)^2+\frac{\lambda_1}{K_0}+\frac{\lambda_2}{K_0}x\sin\alpha=\frac{1}{2\pi K_0}\frac{d\mu}{ds}\ , \\ \frac{dx}{ds}=\cos\alpha \end{gathered} \tag{3.2}$$

where the functions looked for are $\alpha(s)$ and $x(s)$, and, naturally, $\mu(s)$. As the independent variable s does not appear explicitly in the Lagrangian and the upper limit of the integration is arbitrary, a first integral of the Euler–Lagrange equations is obtained in the form of

$$K_0 2\pi x\left[\left(\frac{\sin\alpha}{x}-a^*\right)^2-\left(\frac{d\alpha}{ds}\right)^2\right]+2\pi\lambda_1 x+\pi\lambda_2 x^2\sin\alpha-\mu\cos\alpha=0\ . \tag{3.3}$$

The first integral gives the opportunity to eliminate the auxiliary function $\mu(s)$ from the equations. The equations to be solved are of the form

$$\begin{aligned} \frac{d^2\alpha}{ds} &= \left(\frac{\sin\alpha}{x}-\frac{d\alpha}{ds}\right)^2\frac{\cos\alpha}{x}+ \\ &+ \frac{\sin\alpha}{2\cos\alpha}\left[\left(\frac{\sin\alpha}{x}-a^*\right)^2-\left(\frac{d\alpha}{ds}\right)^2+\frac{\lambda_1}{K_0}+\frac{\lambda_2}{2K_0}\frac{x}{\sin\alpha}\right]\ , \\ \frac{dx}{ds} &= \cos\alpha \end{aligned} \tag{3.4}$$

These equations are highly non-linear and obtaining an analytical solution seems a hopeless task; yet a sphere with radius r

$$\alpha=\frac{s}{r};\qquad x=r\sin\frac{s}{r} \tag{3.5}$$

may be a solution if the condition

$$\frac{\lambda_1 r}{2K_0} + \frac{\lambda_1}{K_0} + a^* \left(a^* - \frac{2}{r} \right) = 0 \tag{3.6}$$

is satisfied. The forms slightly deviating from a sphere may be sought in the implicit form

$$s = r[\alpha + v(\alpha)]; \qquad x = r \sin\alpha [1 + u(\alpha)] \tag{3.7}$$

and the differential equations are linearized for $u(\alpha)$ and $v(\alpha)$. The detailed calculations (see in [4]) show that the condition

$$\frac{\lambda_2 r^3}{4K_0} + ra^* = n(n+1) \qquad \{n = 2, 3, \dots\} \tag{3.8}$$

holds for any smooth surface. The smallest value of n determines the load the sphere collapses at. From higher order approximations Deuling and Helfrich [15] determined that elongated forms are preferred if

$$a^* r > -\frac{39}{23} \tag{3.9}$$

and flattened ones else. The numerical computations are in agreement with the above value.

4. Numerical computations

For various reasons the set of equations (3.4) is not the best for numerical computations. The first is that the parameters contain information not only on the shape but on the size as well; the number of the parameters can be reduced. The second is that the equations have a number of removable singularities, which can have cause troubles to emerge during the run of a computer program.

The first problem is eliminated by introducing the new variables x', s', A, and K making use of the transformation rules

$$x = Dx'; \quad s = ds'; \quad A = Da^*; \quad K' = \frac{\lambda_2 D^3}{2K_0} \tag{4.1}$$

where length D is chosen suitably so that

$$2\lambda_1 + \lambda_2 D = 0\ . \tag{4.2}$$

With the above transformation, equations (3.4) turn into

$$\begin{aligned}
\frac{d^2\alpha}{ds'^2} &= \left(\frac{\sin\alpha}{x'} - \frac{da}{ds'}\right)\frac{\cos\alpha}{x'} + \\
&+ \frac{\sin\alpha}{2\cos\alpha}\left[\left(\frac{\sin\alpha}{x'} - A\right)^2 - \left(\frac{d\alpha}{ds'}\right)^2 - K + K\frac{x'}{\sin\alpha}\right], \qquad (4.3)\\
\frac{dx'}{ds'} &= \cos\alpha
\end{aligned}$$

The transformation has reduced the number of parameters to two.

The other problem is the presence ot the removable singularities at the places where $x' = 0$, or $\cos\alpha = 0$; at the top, at the bottom, and anywhere the tangent of the contour is parallel to the axis. The latter is the more inconvenient. It can be eliminated by introducing the auxiliary variable Ξ with the formula

$$\Xi = \frac{x'}{\cos\alpha}\left[\left(\frac{\sin\alpha}{x'} - A\right)^2 - \left(\frac{d\alpha}{ds'}\right)^2 - K + Kx'\sin\alpha\right]. \qquad (4.4)$$

With this trick, the set of equations to be solved turns into

$$\begin{aligned}
\frac{d^2\alpha}{ds'^2} &= \left(\frac{\sin\alpha}{x'} - \frac{d\alpha}{ds'}\right)\frac{\cos\alpha}{x'} + \frac{K}{2}x'\cos\alpha + \frac{\sin\alpha}{2x'}\Xi,\\
\frac{d\Xi}{ds'} + \Xi\frac{\cos\alpha}{x'} &= (3x'\sin\alpha - 2)K - 2.4\left(\frac{d\alpha}{ds'} + \frac{\sin\alpha}{x'} - A\right), \qquad (4.5)\\
\frac{dx'}{ds'} &= \cos\alpha,
\end{aligned}$$

where the only singularities left are at the top and at the bottom.

4.1. **Fine Points of Computations.** The computations have been done with the Runge–Kutta method with some slight modifications. The starting point is the bottom. The only initial condition needed is the curvature there, c_0. The derivatives at the start are determined from the definition of Ξ and the differential equations — using L'Hospital's rule. The steps of the Runge–Kutta method are programmed so that the derivatives at the beginning are input quantities and output quantities are the values of the functions and of the derivatives.

Any triplet of A, K, and c_0 determines a curve in the x–y plane but not all can be the contour of a smooth surface. For a given value of A, a phase plane is defined – the coordinates are the (non-dimensional) underpressure K and the (non-dimensional) bottom curvature c_0 – in which the points determining the contour of a smooth surface form lines. The above parameters were chosen partly for the ease of computations, partly for the sake of those reproducing the computations. In principle, if the parameters belong to such a line, the computer program runs along the contour and arrives at the axis y orthogonally. But it is never so – the solutions looked for are instable in Liapunov's sense. The parameters may be close to the line

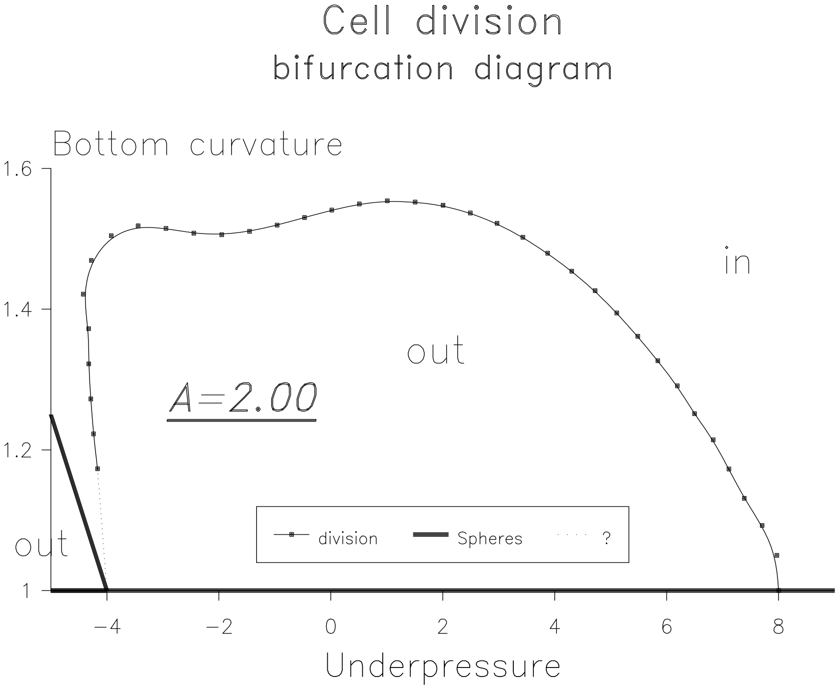

Figure 4. Phase diagram for cell division.

but are not exactly on it. This way the computer line – when running close to the contour of a smooth surface— takes a sharp bend before reaching the axis y. It may bend inward or outward according to what side of the phase line the phase point is on. (The domains in Figures 4 and 5 are labeled with 'in' and 'out', respectively.) Halving intervals, phase lines can be determined with sufficient accuracy. The physically more relevant variable (the ratio of the volume to the maximal one having room in the same envelope) is defined for the phase lines only and the computations give its value.

In Figure 4 the phase diagram of cell division is shown. (The forms are shown in Figure 1 for $A = 2$). Figure 5 is the phase diagram for $A = 0$. It shows both the elongated and flattened forms, moreover, the phase line of pear-like forms and the forms after the buckling of lateral symmetry. The elongated forms and the pear like join curiously – the two phase lines wind on to the same point. Nevertheless, the gastrulated forms in Figure 2 have been calculated with $A = -10$, the proper diagram – having very similar topology – would be inconvenient to print for the extreme sizes. According to the experience of computations, the forms of cell division appear if A is greater than a number slightly smaller than 1.8 and remain similar for very high values of A. The forms of gastrulation vary with the value of A. The higher the absolute value of the negative A is, the earlier the lateral symmetry beaks.

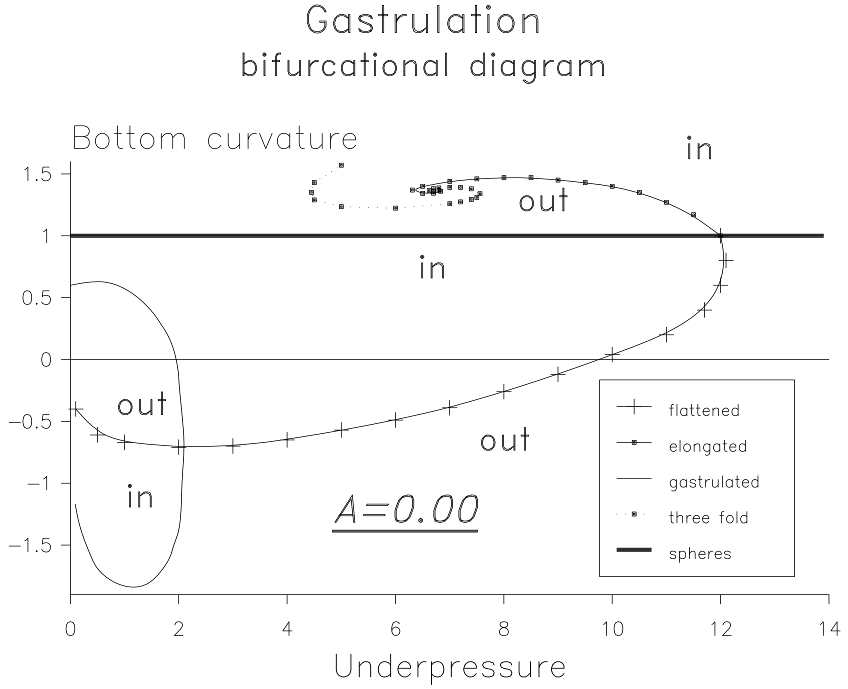

Figure 5. Phase diagram for gastrulation and other forms.

5. **Conclusions**

The results of calculations and computations presented prove that a fluid membrane with bending energy is able to produce the shapes necessary for proliferation. The model works even in a pre-biotic environment – in the ancient broth.

It would be nice if biology could find the fingerprints of this primitive mechanism in modern living beings.

References

1. Helfrich, W.: The size of bilayer vesicles generated by sonication. *Phys. Lett. A*, **50**, (1974), 115–116.
2. Gompper, G. and Zschocke, S.: Ginzburg–Landau theory of oil–water–surfactant mixtures. *Phys. Rev.*, **A 46**, (1992), 4836–4851.
3. Deuling, H. J. and Helfrich, W.: Red blood cell shapes as explained on the basis of curvature elasticity. *Biophys. J.*, **16/8**, (1976), 861–868.
4. Verhás, J.: A liquid crystal model for early cell division. *Liquid Crystals (London)*, **3**, (1988), 1183–1190.
5. Verhás, J.: Liquid crystal membranes with morphogenetic relevance. In H. T. W. Schneider and F. Zigler (eds.), *Lecture Notes in Physics, Trends in Applications*

of Pure Mathematics to Mechanics. Proceedings, Hollabrunn, Austria. 1989., Longman, London, 1991.

6. Seifert, U. and Lipowsky, R.: Addhesion of vesicles. *Phys. Rev.*, **A 42**, (1990), 4768–4771.
7. Oseen, C. W.: The theory of liquid crystals. *Trans. Faraday Soc.*, **29**, (1933), 883–899.
8. Frank, F. C.: On the theory of liquid crystals. *Disc. Faraday Soc.*, **25**, (1958), 19–28.
9. Kralj-Iglic, V., Svetina, S., and Zeks, B.: The existence of non-axisymmetric bilayer vesicle shapes predicted by the bilayer couple model. *Eur. Biophys. J.*, **22**, (1993), 97–103.
10. Lipowsky, R.: Statistical physics of flexible membranes. *Physica A*, **194**, (1993), 114–127.
11. Koch, A. L., Higgins, M. L., and Doyle, R. J.: Surface tension-like forces determine bacterial shapes: Streptococcus faecium. *Journal of General Microbiology*, **123**, (1981), 151–161.
12. Koch, A. L.: How bacteria grow and divide in spite of internal hydrostatic-pressure. *Canadian Journal of Microbiology*, **31**, (1985), 1071–1084.
13. Koch, A. L.: The bacterium's way for safe enlargement and division. *Applied and Environmental Microbiology*, **66**, (2000), 3657–3663.
14. Koch, A. L.: Control of the bacterial cell cycle by cytoplasmic growth. *Critical Reviews in Microbiology*, **28**, (2002), 61–77.
15. Deuling, H. J. and Helfrich, W.: The curvature elasticity of fluid membranes. *Physique*, **37**, (1976), 1335–1345.

Notes for Contributors

to the Journal of Computational and Applied Mechanics

Aims and scope. The aim of the journal is to publish research papers on theoretical and applied mechanics. Special emphasis is given to articles on computational mechanics, continuum mechanics (mechanics of solid bodies, fluid mechanics, heat and mass transfer) and dynamics. Review papers on a research field and materials effective for teaching can also be accepted and are published as review papers or classroom notes. Papers devoted to mathematical problems relevant to mechanics will also be considered.

Frequency of the journal. Two issues a year (approximately 80 pages per issue).

Submission of Manuscripts. Submission of a manuscript implies that the paper has not been published, nor is being considered for publication elsewhere. Papers should be written in standard grammatical English. Two copies of the manuscript should be submitted on pages of A4 size. The text is to be 130 mm wide and 190 mm long and the main text should be typeset in 10pt CMR fonts. Though the length of a paper is not prescribed, authors are encouraged to write concisely. However, short communications or discussions on papers published in the journal must not be longer than 2 pages. Each manuscript should be provided with an English Abstract of about 50–70 words, reporting concisely on the objective and results of the paper. The Abstract is followed by the Mathematical Subject Classification – in case the author (or authors) give the classification codes – then the keywords (no more than five). References should be grouped at the end of the paper in numerical order of appearance. Author's name(s) and initials, paper titles, journal name, volume, issue, year and page numbers should be given for all journals referenced.

The journal prefers the submission of manuscripts in LaTeX. Authors should prefer the AMS-LaTeX article class and are not recommended to define their own LaTeX commands. Visit our home page for further details concerning the issue how to edit your paper.

For the purpose of refereeing, two copies of the manuscripts should initially be submitted in hardcopy to an editor of the journal. The eventual supply of an accepted-for-publication paper in its final camera-ready form (together with the corresponding files on an MS–DOS diskette) will ensure more rapid publication. Format requirements are provided by the home page of the journal from which sample LaTeX files can be downloaded:

`http://www.uni-miskolc.hu/home/web/pumns/mechanics`

These sample files can also be obtained directly (via e-mail) from a member of the Editorial Board, Gy. Szeidl (Gyorgy.SZEIDL@uni–miskolc.hu), upon request.

Twenty offprints of each paper will be provided free of charge and mailed to the correspondent author.

The Journal of Computational and Applied Mechanics is abstracted in Zentralblatt für Mathematik and in the Russian Referativnij Zhurnal.

Responsible for publication: Rector of the Miskolc University
Published by the Miskolc University Press under the leadership of Dr. József PÉTER
Responsible for duplication: works manager Mária KOVÁCS
Number of copies printed: 200
Put to the Press on June 12, 2008
Number of permission: TU 2008-338-ME **HU ISSN 1586–2070**

A Short History of the Publications of the University of Miskolc

The University of Miskolc (Hungary) is an important center of research in Central Europe. Its parent university was founded by the Empress Maria Teresia in Selmecbánya (today Banska Štiavnica, Slovakia) in 1735. After the first World War the legal predecessor of the University of Miskolc moved to Sopron (Hungary) where, in 1929, it started the series of university publications with the title *Publications of the Mining and Metallurgical Division of the Hungarian Academy of Mining and Forestry Engineering* (Volumes I.-VI.). From 1934 to 1947 the Institution had the name Faculty of Mining, Metallurgical and Forestry Engineering of the József Nádor University of Technology and Economic Sciences at Sopron. Accordingly, the publications were given the title *Publications of the Mining and Metallurgical Engineering Division* (Volumes VII.-XVI.). For the last volume before 1950 – due to a further change in the name of the Institution – *Technical University, Faculties of Mining, Metallurgical and Forestry Engineering, Publications of the Mining and Metallurgical Divisions* was the title.

For some years after 1950 the Publications were temporarily suspended.

After the foundation of the Mechanical Engineering Faculty in Miskolc in 1949 and the movement of the Sopron Mining and Metallurgical Faculties to Miskolc, the Publications restarted with the general title *Publications of the Technical University of Heavy Industry* in 1955. Four new series - Series A (Mining), Series B (Metallurgy), Series C (Machinery) and Series D (Natural Sciences) - were founded in 1976. These came out both in foreign languages (English, German and Russian) and in Hungarian.

In 1990, right after the foundation of some new faculties, the university was renamed to University of Miskolc. At the same time the structure of the Publications was reorganized so that it could follow the faculty structure. Accordingly three new series were established: Series E (Legal Sciences), Series F (Economic Sciences) and Series G (Humanities and Social Sciences). The latest series, i.e., the series H (European Integration Studies) was founded in 2001. The eight series are formed by some periodicals and such publications which come out with various frequencies.

Papers on computational and applied mechanics were published in the

Publications of the University of Miskolc, Series D, Natural Sciences.

This series was given the name Natural Sciences, Mathematics in 1995. The name change reflects the fact that most of the papers published in the journal are of mathematical nature though papers on mechanics also come out.

The series

Publications of the University of Miskolc, Series C, Fundamental Engineering Sciences

founded in 1995 also published papers on mechanical issues. The present journal, which is published with the support of the Faculty of Mechanical Engineering as a member of the Series C (Machinery), is the legal successor of the above journal.

Journal of Computational and Applied Mechanics
Volume 6, Number 1 (2006)

Contents

Contributed Papers